# ENHANCED THERMAL IMAGING A NOVEL IMAGING TECHNIQUE FOR MONITORING RE-PERFUSION POST-OPERATIVELY

by

Cobey L. McGinnis

A dissertation submitted to the faculty of
The University of North Carolina at Charlotte
in partial fulfillment of the requirements
for the degree of Doctor of Philosophy in
Optical Science and Engineering

Charlotte

2023

Approved by:

_____
Dr. Susan R. Trammell

_____
Dr. Glenn Boreman

_____
Dr. Mike Fiddy

_____
Dr. Russ Keanini

_____
Dr. Didier Dréau

# ABSTRACT

COBEY L. MCGINNIS. Enhanced Thermal Imaging a Novel Imaging Technique for Monitoring Re-Perfusion Post-Operatively. (Under the direction of DR. SUSAN R. TRAMMELL)

We are developing a real-time infrared imaging technique, Enhanced Thermal Imaging (ETI), that can detect blood vessels embedded in tissue and assess tissue perfusion. ETI is a combination of standard thermal imaging (8 - 10 $\mu$m) and selective heating of blood relative to surrounding water-rich tissue using LED sources at low power. Blood absorbs strongly at 530 nm. Illumination of water-rich tissue and embedded blood vessels at this wavelength selectively increases the temperature of the blood vessels relative to the surrounding tissue causing the vessels to appear brighter in a thermal image. ETI does not require the use of injectable dyes and has a compact footprint allowing for use both during surgery and at the bedside.

Previous studies using ETI were limited due to lengthy post-processing times required to delineate vessels. The first study in this dissertation shows the real time capabilities of ETI in mapping vascular structures. Real time application of computational filters highlighting temporal and spatial changes reveal embedded blood vessels. The temporal filter averages the frames captured before LED illumination and then subtracts that average frame from each subsequent frame. The result is a 2-dimensional map showing how each pixel in the image changes temperature as the result of LED illumination. The spatial filter applies a 2-dimensional gradient function across each frame. This creates a 2-dimensional map showing the difference for each pixel from the neighboring pixels, thus revealing temperature boundaries. ETI was obtained of a model with simulated blood vessels and a porcine heart tissue model. In both sets of experiments the temporal and spatial filters outperformed standard thermal imaging. The temporal filter consistently increased the contrast between the vessel/tubing and the surrounding tissue. This increase in contrast al-

lows for the temporal filter to detect and map the vessels more quickly and accurately than standard thermal imaging. The application of the spatial filter consistently delineated the vessel walls clearly and provided measurements of the vessel width. The spatial filter images have potential to highlight the presence of occlusions in vessels.

In the second study presented in this dissertation, simulations of the illumination and heating of the blood vessels embedded in tissue were conducted to understand the effects of LED power and vessel depth on the ability of ETI to detect vessels. The simulations were performed with an open-source MATLAB integrated solver, MCmatlab. A tissue model with a volume of 1 $cm^3$ consisting of air, epidermis, dermis, and a single blood vessel was simulated using several different LED illumination powers (0.1 - 1 W) and different vessel depths (1 - 3 mm). ETI can be used in two different modalities, direct and indirect illumination. Both modalities were simulated. In direct illumination the area of illumination is the same as the area of imaging. In indirect illumination, the region of interest for imaging is downstream (in direction of blood flow) from the site of illumination. The objective of the simulations was to characterize the limitations of ETI, optimize imaging parameters and understand the effects of vessel depth and width on imaging. The results of the simulations were compared to *ex vivo* tissue experiments of ETI using porcine skin, blood, dissected kidney vessels, and intact porcine hearts.

In the third study presented in this dissertation, ETI was used to monitor the healing of skin flaps in a murine model. ETI, fluorescent imaging and visual inspection were used to assess the viability of skin flaps in 15 mice over a 12 day study period. The results from these three different techniques were then compared. ETI plus the temporal derivative filter revealed persistent healing not seen using the other techniques. This study shows the potential of ETI to assess re-perfusion post-operatively with insights into non-superficial healing.

# DEDICATION

I will be the first to admit that I could not achieve this goal on my own. I would like to dedicate this work to my countless friends who supported me. I know I was absent for many events because of my arduous work schedule, but to those who stayed by my side unquestioningly I can't express the extent of my gratitude. To my family I know it has been rough with how often I had to choose school over them, but their love has allowed me to keep pursuing this goal.

# ACKNOWLEDGEMENTS

First I would like to thank Dr. Susan Trammell for her guidance. Without her I would not be where I am today nor would I have the confidence to succeed in my future career.

I would also like to thank Dr. Glenn Boreman, Dr. Russel Keanini, Dr. Mike Fiddy, and Dr. Didier Dréau. Their expertise and guidance as committee members has been impactful and helped me to conduct and present the following work.

I would like to thank my fellow students Daniel Furr, Anteneh Tsegaye, Maddie Kern, and Gunnar Olson for help in collecting, analyzing, and interpreting the data throughout this process.

Finally I would like to thank my friends and family for their unending support and love.

TABLE OF CONTENTS

# LIST OF TABLES

# LIST OF FIGURES

# LIST OF ABBREVIATIONS

ETI Enhanced Thermal Imaging

IVIS In Vivo Imaging system

OSE An acronym for Optical Science and Engineering.

# CHAPTER 1: INTRODUCTION

## 1.1 Motivation

Enhanced Thermal Imaging (ETI) is a new thermal infrared imaging modality that uses heat as a contrast agent to visualize microvasculature embedded in soft tissue. ETI is a combination of thermal IR imaging (8 - 10 $\mu$m) and selective heating of blood relative to surrounding water-rich tissue.[1–3] This imaging technique is non-destructive and does not require the use of ionizing radiation or IV contrast agents, making it an imaging tool that could be used for surgical planning and guidance. Currently, imaging techniques used for surgical planning include x-ray, computed tomography (CT) and magnetic resonance imaging (MRI). These imaging modalities are generally not available during surgery and both CT and x-ray imaging use ionizing radiation. Indocyanine green angiography (ICGA) can accurately map vascular networks during surgical procedures, but requires the intravenous application of a fluorescent dye. A better method for intraoperative imaging and guidance is needed for procedures such as the delineation of margins around solid mass tumors, assessment of the perfusion of skin flaps during reconstructive microsurgery, evaluation of the perfusion in regions around complex closures during amputation and cardiac bypass surgery.

ETI is an imaging technique that can be used intraoperatively and does not require the use of injectable dyes or ionizing radiation. In previous work, ETI successfully highlighted the blood-rich vascular region that is routinely targeted for surgical excision around mammary tumor masses in a murine model.[2] The enhanced IR images revealed a corona of bright emission along the edges of the tumor masses associated with the vessel-rich peri-tumoral zone. In another previous study, ETI was used to map the flow of blood through vasculature in porcine heart tissue *ex vivo*.[1] The study

demonstrated that ETI can be used to map embedded vascular networks and has potential applications in surgery. In these earlier studies, significant post-acquisition processing was required to visualize blood vessels. In this dissertation, we describe recent efforts to apply spatial and temporal filtering as imaging is acquired and thus enable real-time ($\geq$ 1 fps) acquisition of images. In addition, computational simulations of ETI provide insights into the limits of the technique and may provide a way to estimate the depth and width of embedded vessels. Further, a study exploring ETI as a means to evaluate blood perfusion in skin flaps is presented. For reference, typical sizes and lengths of vessels in the human body are shown in Table 1.1. The secondary/tertiary branches and capillary beds are of particular interest in the studies presented in this dissertation.

Table 1.1: Lengths and diameters of different vessel types in the human body.[4]

| Vessel Type | Diameter (mm) | Length (cm) |
|---|---|---|
| Aorta | 10 | 40 |
| Large arteries | 3 | 20 |
| Main branches | 1 | 10 |
| Secondary branches | 0.6 | 4 |
| Tertiary branches | 0.14 | 1.4 |
| Terminal branches | 0.05 | 0.1 |
| Terminal arteries | 0.03 | 0.15 |
| Arterioles | 0.02 | 0.2 |
| Capillaries | 0.008 | 0.1 |
| Vernules | 0.03 | 0.2 |
| Terminal branches | 0.07 | 0.15 |
| Terminal veins | 0.13 | 0.1 |
| Secondary veins | 1.5 | 4 |
| Main veins | 2.4 | 10 |
| Large veins | 6 | 20 |
| Vena cava | 12.5 | 40 |

## 1.2 Black-Body Radiation

A perfect blackbody is defined as an object that absorbs all radiation incident upon it. In order for this object to stay in thermal equilibrium with the environment, it

must emit electromagnetic radiation at all frequencies in proportion to the rate of absorption. A perfect blackbody re-radiates energy at all wavelengths (a continuous spectrum) and the spectral energy distribution of the emitted radiation depends only on the temperature of the blackbody. Figure 1.1 shows the spectra of several black-body radiators with different temperatures. In 1901 Max Planck postulated that the emission of light from a blackbody is quantized and derived an expression to describe the spectral energy distribution of a blackbody source (see Equation 1.1).

$$B(\upsilon, T) = \frac{2h\upsilon^3}{c^2} \frac{1}{\frac{\hbar\upsilon}{ek_bT} - 1} \tag{1.1}$$

In Equation 1.1, $B$ is the spectral radiance of a blackbody in $\mathrm{W{\cdot}sr^{-1}{\cdot}m^{-2}{\cdot}Hz^{-1}}$, $\upsilon$ is the frequency of emitted radiation, $T$ is the absolute temperature, $k_b$ is the Boltzmann constant, $\hbar$ is Planck's constant, and $c$ is the speed of light. An evaluation of Planck's law shows that as the frequency increases the spectral radiance approaches zero, thus avoiding the ultraviolet catastrophe of the Rayleigh-Jeans formula that had previously been used to describe blackbody radiation.

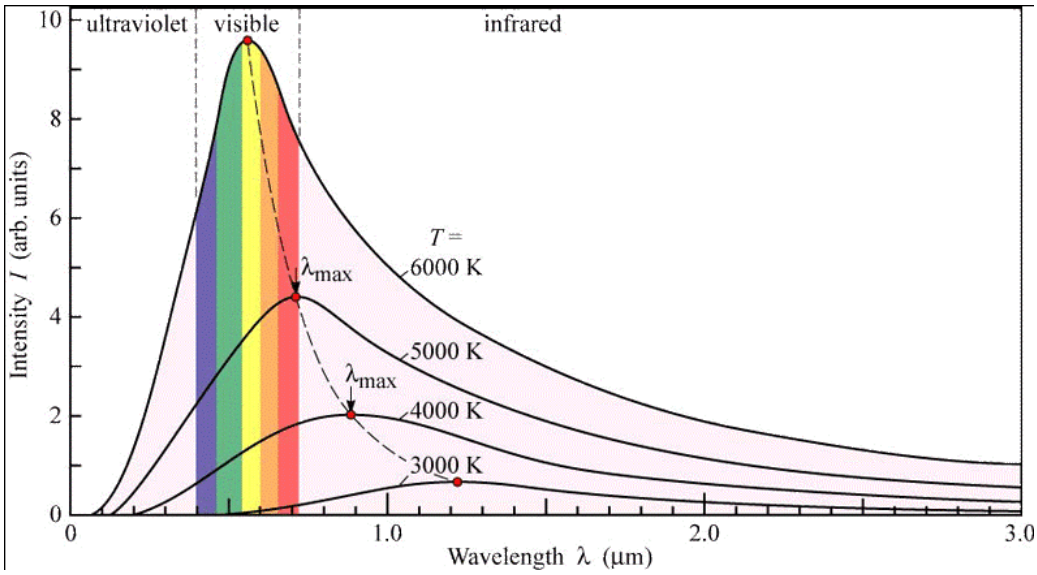


Figure 1.1: Black-body emission spectrum.[5]

The Stefan-Boltzmann law states that the total energy radiated per unit surface

area of a black body per unit time, $J$, is directly proportional to the fourth power of the black body's absolute temperature ($T$),

$$J = \sigma T^4 \tag{1.2}$$

where $\sigma$ is the Stefan-Boltzmann constant. As the temperature of the blackbody increases, emittance increases as can be seen in Figure 1.1. Wien's Displacement law describes the relationship between the wavelength at which the most radiation is emitted ($\lambda_{max}$) and the temperature of the blackbody.

$$\lambda_{max} = \frac{2.898 \text{ x } 10^{-3}}{T} \tag{1.3}$$

where $\lambda_{max}$ is the wavelength in meters at which the blackbody emission peaks and $T$ is the temperature of the object in Kelvin. As the temperature of the blackbody increases, the peak wavelength decreases as can be seen in Figure 1.1.

All objects with a temperature above 0 K emit radiation. The emissitivity, $\epsilon$, is the ratio of the radiant energy emitted by an object to that emitted by a blackbody at the same temperature and can be used to describe how well the radiative emission of an object can be approximated by a blackbody spectrum. This emissitivity value can be included in the Stefan-Boltzmann equation.

$$J = \epsilon \sigma T^4 \tag{1.4}$$

A material with an emissivity value of 1 is a perfect blackbody radiator, while lower emissitivities indicate that an object's emitted spectrum deviates from a perfect blackbody. For example, polished metals typically have low emissivity values. The majority of organic materials have emissitivities very close to 1.0. The emissitivity of human tissue is approximately 0.95, indicating that it can be well approximated as

a blackbody radiator.[6] The human body has a temperature of approximately 310 K. Utilizing Equation 1.3, we can calculate that the peak wavelength of emission for the human body is approximately 9.34 $\mu$m. This is in the infrared part of the electromagnetic spectrum and this blackbody emission from a human body can be detected using a thermal camera.

## 1.3 Light-Tissue Interaction

Light can interact with matter in several ways including reflection, refraction, absorption, and scattering. When light impinges on a boundary between two materials, light will reflect at the material boundary where a change in refractive index occurs, and refract as the light speeds up or slows down upon entering the new material. Absorption occurs within a material and is dependent upon the energy of the light and the potential difference of the electron cloud energy levels in the atoms that make up the material. Scattering occurs as light propagates through a material. The direction and magnitude of scattering is dependent upon the size and shape of the scattering particles and the wavelength of the light. In this dissertation, the interaction between tissue and incident light, as well as the thermal emission from tissue will be considered and all of these processes play a role.

Reflection and refraction at the boundary between two materials are dependent on their refractive index values and the angle of incidence of the light. The law of reflection states that the angle of incidence is equal to the angle of reflection as illustrated in Figure 1.2. The path of the light that is transmitted into the new material can be determined from Snell's law

$$n_1 sin(\theta_1) = n_2 sin(\theta_2) \tag{1.5}$$

where $\theta_1$ is the angle of incidence, $\theta_2$ is the angle of refraction and $n_1$ and $n_2$ are the indices of the two materials.

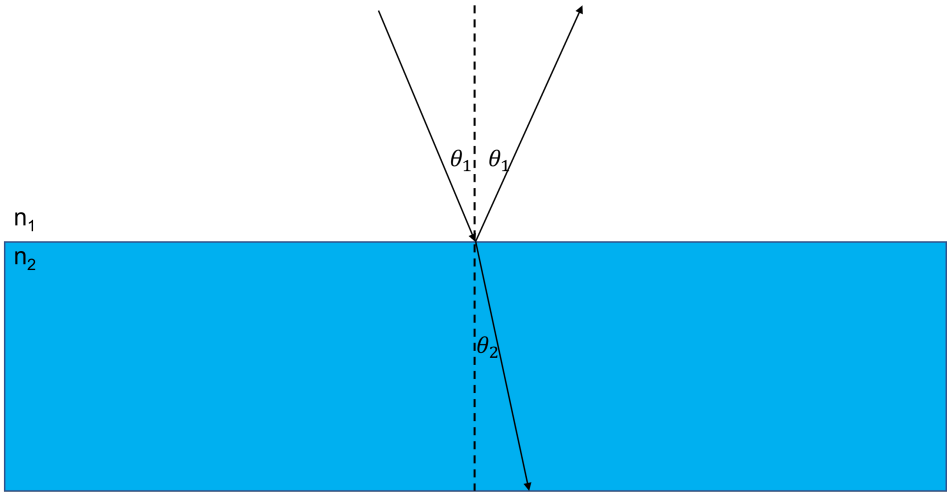


Figure 1.2: The path light takes when it is incident on a material with refractive index $n_2$. In this case $n_2 > n_1$.

Figure 1.2 show that path of light incident on a material with refractive index $n_2 > n_1$, at angle $\theta_1$ from the normal. The portion of the light that travels into the material will refract as the light slows down when it propagates into a region with a higher refractive index. The new speed of propagation is $v = c/n$ in which $v$ is the new speed of the light, $c$ is the speed of light in a vacuum, and $n$ is the refractive index of the material. This decrease in the speed results in a path such that $\theta_2 < \theta_1$. In the case that $n_1 > n_2$ the opposite is true resulting in $\theta_2 > \theta_1$.

The absorption of light by a material is governed by the energy level structures of the molecules that make up the material and the wavelength of light incident on the material. To better understand the absorption of light by a material, the particle model of light is useful. As the wavelength of light decreases, the amount of energy carried by a photon increases. Equation 1.6 shows this relationship between the wavelength of light and photon energy,

$$E = \frac{hc}{\lambda} \tag{1.6}$$

where $h$ is Planck's constant, $c$ is the speed of light in a vacuum, and $\lambda$ is the

wavelength of the light.

It is easiest to understand absorption starting with the simplest atom, the hydrogen atom. We can model the allowed energy levels in a hydrogen atom using the Bohr model (see Figure 1.3). The allowed energies of electrons are given by,

$$E(n) = \frac{-1}{n^2} \cdot 13.6eV \tag{1.7}$$

where $n$ is the principle quantum number of the energy level. The energy separation between two levels is then

$$\Delta E(n) = (\frac{1}{n_{low}^2} - \frac{1}{n_{high}^2}) \cdot 13.6eV \tag{1.8}$$

The hydrogen atom can only absorb light that carries an energy equal to $\Delta E(n)$ When absorption occurs, an electron in a lower energy level moves into a higher energy level. This electron in the higher energy level will drop to a lower energy state after some time $t$ called the relaxation time. The energy lost in this transition is dissipated either by the release of another photon(s) or by increasing the thermal energy of the material.

For more complex atoms the electrons and nuclei can be considered as a system of simple harmonic oscillators governed by Hooke's law. In this model, electrons are imagined to be connected to the nucleus by a single spring, and the electron oscillates at a natural frequency $\omega_0$. When light with frequency $\omega = E/h$ impinges on the system, the frequencies $\omega$ and $\omega_0$ constructively and destructively interfere. If $\omega = \omega_0$ then the impinging light is in resonance with the atom and the frequencies will constructively interfere increasing the oscillatory amplitude of the atom. This oscillatory amplitude can be thought of as the energy state of the atom. Since there is a spring connecting the electron to the nucleus, then there is a restoring force that will eventually force the electron back to a lower energy state.

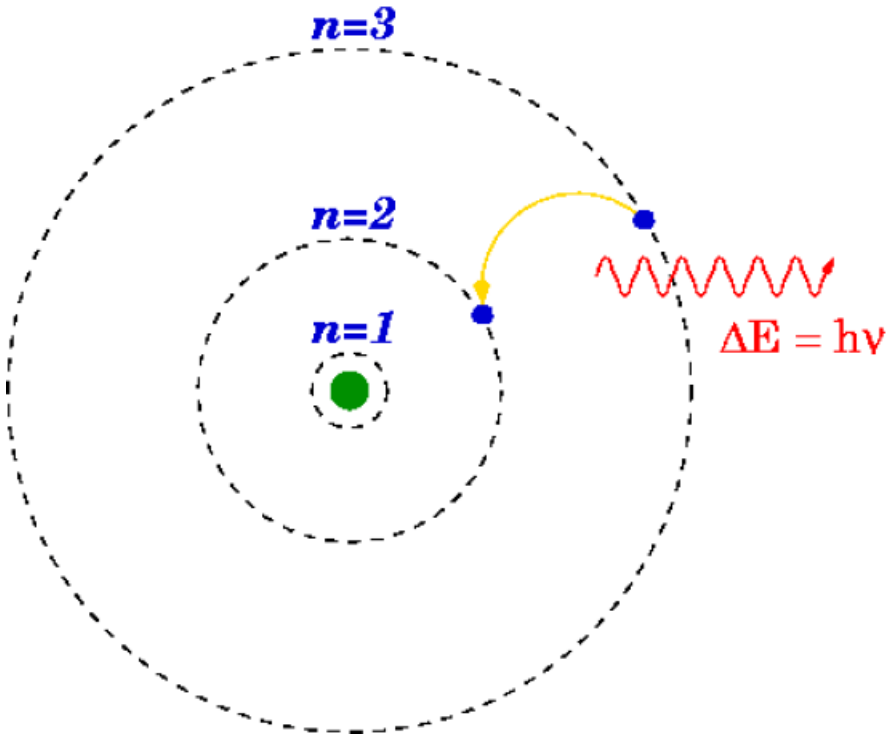


Figure 1.3: Bohr model of the atom[7]

For more complex structures (e.g. molecules), this model of oscillators can be extended by imagining a system of coupled oscillators.[8] An electron/atom displaced in a system does experience a restoring force, however that restoring force is not proportional to the displacement of the electron/atom. Instead an anharmonic oscillatory system or Morse potential can be used to describe the system as shown in Figure 1.4.[8] If a specific amount of energy in the form of light with frequency $v$ impinges on such a system and an electron can be excited to a specific energy level. In Figure 1.4 the system is excited to the energy level $d$. This energy level $d$ allows the molecule to vibrate a distance $d_{j,max} - d_{j,min}$. The molecule can not stay at these higher vibrational energy states and has to return to an equilibrium state after some time. The energy that the molecule absorbed to reach these higher states is then released as longer wavelength radiation (typically in the infrared). As the input energy increases, the excitation level increases and the vibrational distance increases, until a point at which the energy is equal to the dissociation energy and the molecule breaks apart.

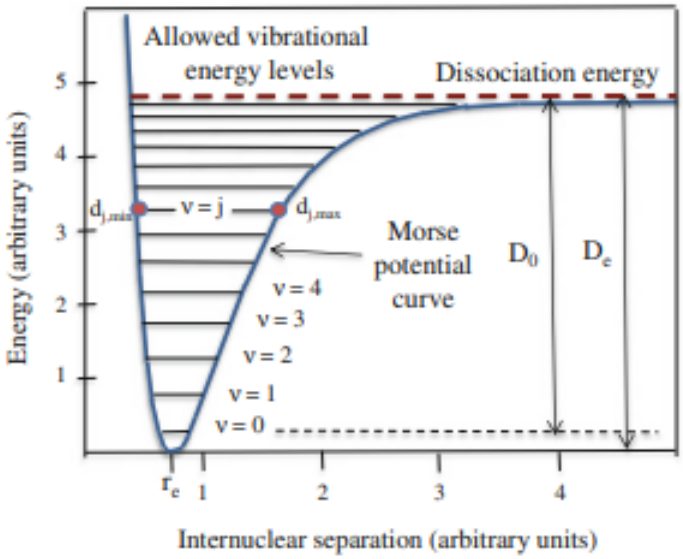


Figure 1.4: Morse potential energy curve for inter-nuclear separation of molecules.[8]

The absorption properties of a material are embedded in the complex refractive index

$$\tilde{n} = n + ik \tag{1.9}$$

where $n$ is the real component of refractive index, and $ik$ is the imaginary component. The imaginary component, or extinction coefficient, of refractive index describes the absorption of light for a specific material and is dependent on the wavelength of light and is given by equation

$$\alpha = \frac{4\pi k}{\lambda} \tag{1.10}$$

where $\alpha$ is the absorption coefficient, $\lambda$ is the wavelength of light and $k$ is the extinction coefficient.[9]

Figure 1.5 shows that when the extinction coefficient is at a maximum, the real component of the refractive index is approaching its local minimum. It is clear that at the wavelength corresponding to the maximum extinction coefficient, the value for $k$ is larger than the value of $n$ and so the complex refractive index is dominated by

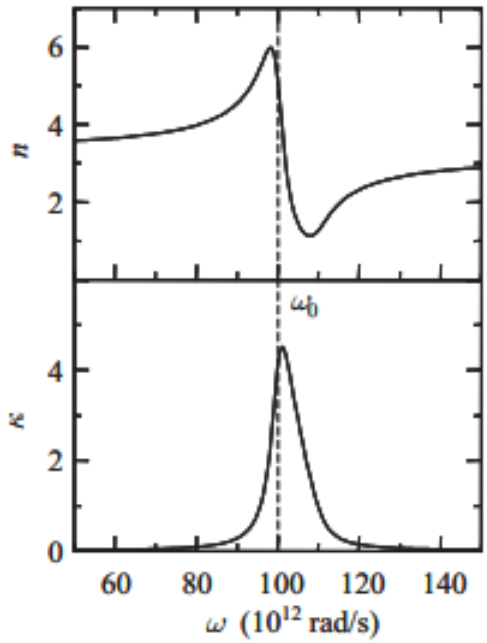


Figure 1.5: A comparison of the real refractive index and the extinction coefficient as a function of wavelength.[9]

the imaginary term. Referring back to equation 1.10, as the complex component $k$ of the refractive index increases the absorption coefficient will increase as well. This will lead to resonance within the molecule and increase the vibrational energy state of the molecule, see figure 1.4.

The absorption cross section, $\sigma_a$, is a metric used to define the absorbing power of a material. This absorption cross section is a ratio of the incident power $P_0$, the absorbed power $P_{abs}$, and the surface area of the material $A$

$$\sigma_a = \frac{P_{abs}}{P_0/A} \tag{1.11}$$

This absorption cross section is also related to the absorption coefficient $\alpha$ by

$$\alpha = \rho\sigma_a \tag{1.12}$$

in which $\rho$ is the density of absorbers in the material. It should be noted that this absorption coefficient has units of inverse length because it is a probability that a photon will be absorbed within a length scale.[8]

The absorption coefficient in Equations 1.10 and 1.12 is accurate within a thin layer of the material. If the material is thick then one must consider multiple stacks of thin layers, and with some mathematics the Beer-Lambert law can be defined. The Beer-Lambert law shows that the attenuation of a collimated light beam with initial intensity $I_0$ as it propagates a distance $x$ in a material is given by

$$I(x) = (1 - R)I_0 exp(-\alpha x) \tag{1.13}$$

where $R$ is the Fresnel Coefficient of reflection, and $I(x)$ is the intensity after some distance $x$. Equation 1.13 shows that the attenuation of a collimated beam of light decays exponentially as it propagates through a material.

Scattering occurs as light propagates through the material and causes light propagating in the forward direction to change directions. Attenuation occurs from scattering because the number of photons that will continue traveling in the forward direction will decrease. The direction and magnitude of scattering is dependent upon the size of the particles scattering the light and the wavelength of the light. The two most common forms of scattering are Rayleigh scattering and Mie scattering. Rayleigh scattering is dominant when the size of the scatters is on the same size-scale as the wavelength of incident light. Mie scattering is dominant when the scatters are larger than the wavelength of light. Scattering occurs in two forms, elastic and inelastic. Elastic scattering causes no change in the frequency of the propagating light, while inelastic scattering changes the frequency of the propagating radiation.

Rayleigh scattering is present in biological tissue, but scattering at optical and infrared wavelengths is dominated by Mie scattering. Figure 1.6 shows size scales for

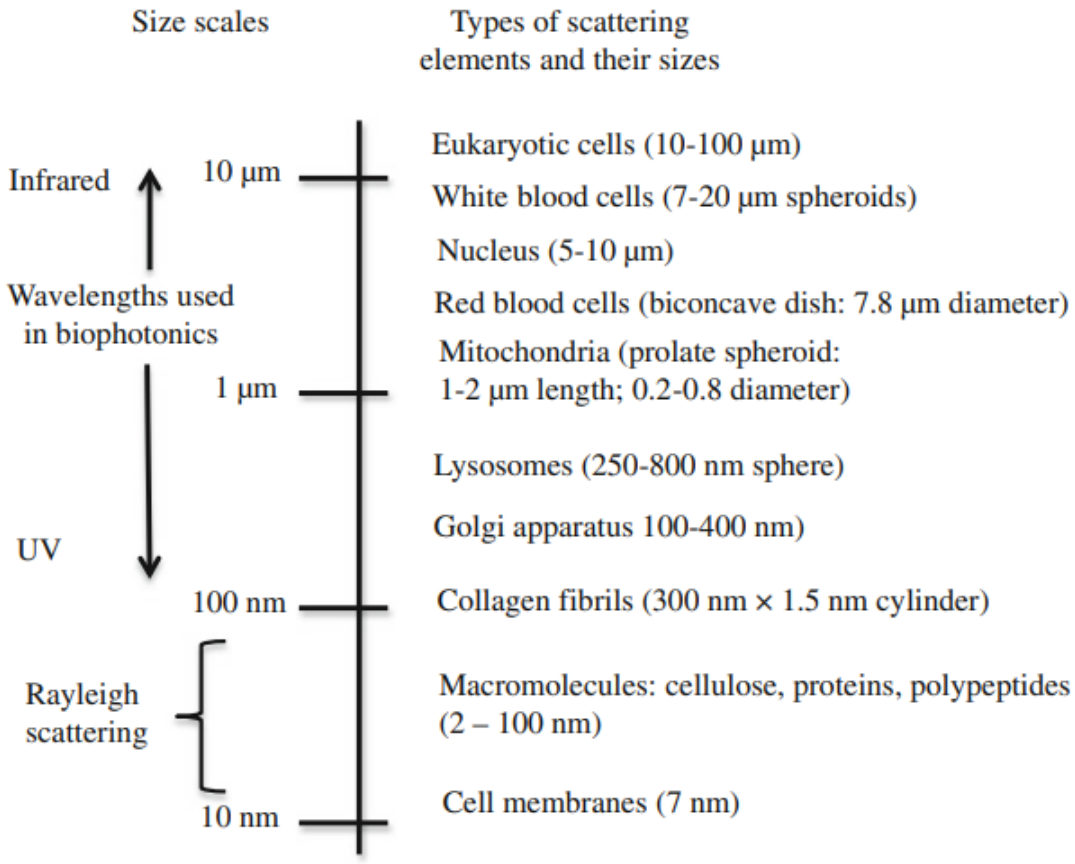


Figure 1.6: Several elements that constitute human tissue and their relative size.[8]

several of the elements comprising human tissue and demonstrates that Mie scattering is the dominant scattering process in this medium.

Similar to absorption, Mie scattering can be parameterized by the scattering cross section, $\sigma_s$, which is a ratio of the scattered power ($P_s$) to the incident power ($P_0$) and the surface area of the material ($A$).[8]

$$\sigma_s = \frac{P_s}{P_0/A} \tag{1.14}$$

Like with absorption, the non-scattered intensity is highly dependent on the distance the light propagates in the material and therefore requires the use of the Beer-Lambert

law resulting in

$$I_s(x) = I_0 exp(-\mu_s x) \tag{1.15}$$

where $I_0$ is the initial intensity, $\mu_s$ is the scattering coefficient of the material and $I_s$ is the intensity that propagates through the scattering medium. The scattering coefficient $\mu_s$ is similar to the absorption coefficient in that it measures the probability per unit length that a photon is scattered in a material. Using the density of optical scatterers $\rho$ the scattering coefficient can be described by

$$\mu_s = \rho\sigma_s \tag{1.16}$$

The path a photon takes in tissue can be described by the scattering mean free path $L_s$ which is the inverse of the scattering coefficient, and represents the average distance a photon will travel before another scattering event occurs. The path of a photon through tissue will resemble Figure 1.7. The path a photon travels in a tissue is not straight and instead the photon can exit the tissue at places translationally far from the point of impingement. The scattering phase function $g$ determines the directionality of scattering. This decides whether forward or backward scattering dominates the direction the scattered light propagates. For human tissue $g$ is typically close to 1 and therefore forward scattering is dominant.

To model the light propagation in a tissue, the reflection and refraction of light at tissue boundaries must be considered, as well as absorption and scattering of light in the tissue. Up to this point the discussion has been focused on homogeneous media which have a constant refractive index, particle size, and particle density. Human tissue is not a homogeneous material, but rather is heterogeneous with spatial variations in refractive index and other properties. This type of medium is referred to as a turbid medium.[8] The propagation of light through a turbid media will be modeled in this dissertation using a Monte Carlo computer simulation. This model

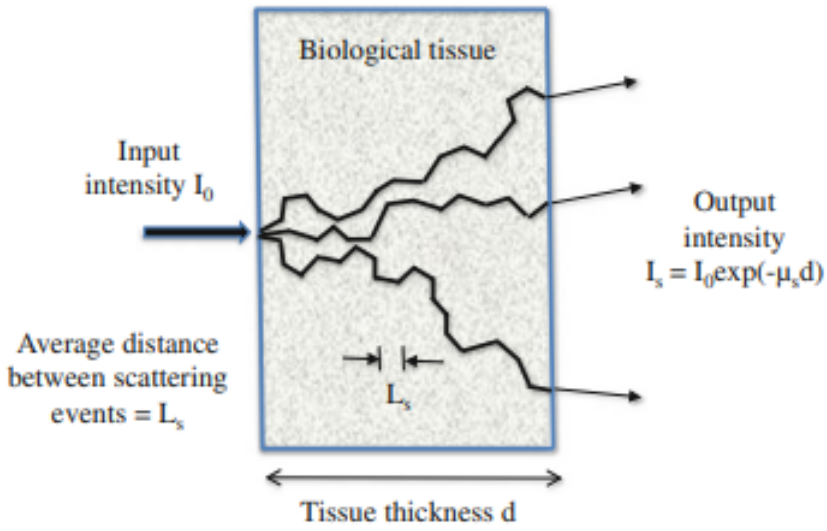


Figure 1.7: The optical path of a photon travelling in a tissue medium due to scattering events.[8]

includes all of the relevant processes and can include different types of tissue with different optical properties in the model.[10,11]

## 1.4 Bio-Heat Equation

In this dissertation, the thermal emission of tissue will also be modeled. Evaluating and understanding the evolution of temperature in living tissue has advanced considerably since the introduction of the most widely used model coined in 1948 by Harry H. Pennes.[12] To fully understand the processes involved in regulating, heating, and cooling of living tissues energy transfer by conduction, convection, perfusion by blood, and metabolic heat production need to be modeled.[13] Not only are these thermodynamic processes involved, but multiple layers of different tissue types each with a respective thermal conductivity, and specific heat are present.

In 1948 Harry H. Pennes proposed a linear equation to model heat transport in biological tissue, called the Pennes bioheat transfer equation

$$\dot{T} = k\nabla^2 T - T/\tau + q_v/c_v \tag{1.17}$$

where $q_v$ is the function of the heat source, $T$ is the temperature rise above the ambient level, $\dot{T}$ is the rate of said temperature rise, $k$ is the thermal diffusivity, $\tau$ is the time constant for perfusion and $c_v$ is the volume specific heat for the tissue. The thermal conductivity coefficient $K$ is proportional to the thermal diffusivity $k$ by a factor of the volume specific heat for tissue $c_v$. This equation was later confirmed by Eberhart et al. in 1980 to be an adequate solution to model the macroscopic temperature distribution in biological tissues.[12,14] This model is a continuum model that examines the thermal impact of all blood vessels with a single global parameter.[13] Although Pennes' original model was an attempt to predict heat transfer in a human arm, it has become the most widely used continuum model to date.[12–14] Pennes modeled blood as an isotropic heat source proportional to the blood flow rate.[12,13] In a biological system, the human body for example, the perfusion rate is dependent upon the thermal regulatory system. This means that any area of the human body will regulate its temperature at the same rate that blood is perfused through the tissue.[13–15] Therefore, $\tau$ can be written as,

$$\tau = \rho_b c_v / w c_{vb} \tag{1.18}$$

in which $\rho_b$ is the density of blood, and $c_{vb}$ is the volume specific heat for blood, and $w$ is the perfusion rate of blood.[14,16] A solution for equation 1.17 comes from considering the heat source as a point source of small volume $dv$ a distance $r$ away. With an adaptation of Greens function, the solution can be written as[14]

$$T = (C/r)E[2 - erfc(t^* - R)] + E^{-1}erfc(t^* + R) \tag{1.19}$$

with variables:

$$C = q_v dv / 8\pi K \tag{1.20}$$

$$E = exp(-r/L) \tag{1.21}$$

$$L = (k\tau)^{1/2} \tag{1.22}$$

$$t^* = (1/\tau)^{1/2} \tag{1.23}$$

$$R = r/(4kt)^{1/2} \tag{1.24}$$

After a long time, the steady state solution becomes

$$T = 2CE/r = (2C/r)exp(-r/L) \tag{1.25}$$

where $L$ is the perfusion length. Since equation 1.19 is the solution for a single point source, a superposition of this solution multiple times will result in a solution for an extended source resulting in

$$\dot{T} = q_v\tau/c_v \tag{1.26}$$

$$T = T_0 exp(-t/\tau) \tag{1.27}$$

in which $T_0$ is the temperature rise at t = 0.[14] This solution shows that the elevated temperature of a perfused medium will decrease exponentially over time. Substituting equation 1.27 into equation 1.17 shows that the temperature of the perfused medium will reach a steady state over a long period of time. This is shown in figure 1.8 in which the temperature of a perfused medium is plotted for equation 1.19 for, (a) different distances $r$ from the heat source, and (b) for different perfusion rates.

## 1.5 Enhanced Thermal Imaging Techniques

Thermal imaging captures pictures and videos at longer wavelengths than optical imaging, thereby collecting information not generally seen by the human eye. Standard imaging generally occurs within the visible region of the electromagnetic spectrum (400 nm to 700 nm) and wavelengths of light longer than approximately

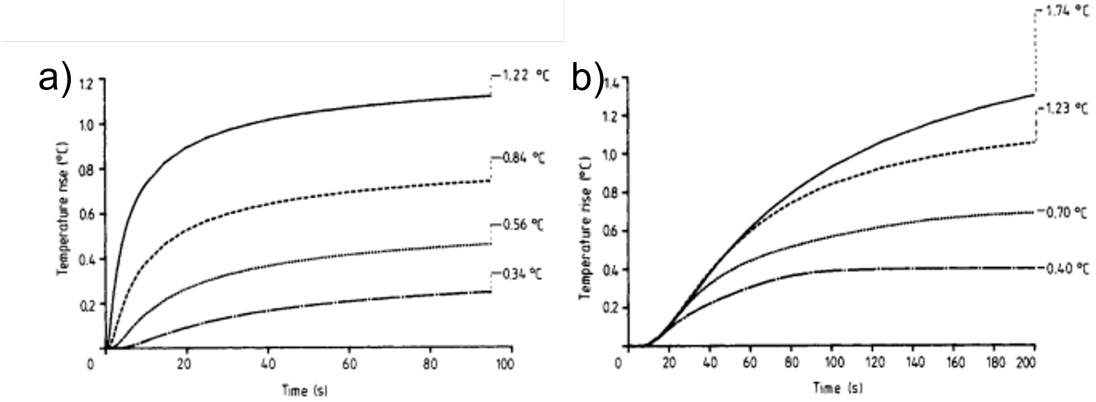


Figure 1.8: a) temperature plotted against time, according to equation 1.19 from a point source generating 10 mW of heat. Perfusion constant is 1000s, and each curve from top to bottom is r = 1mm, r = 1.4 mm, r = 2mm, and r = 3mm respectively. b) Temperature plotted against time for equation 1.19 but at a distance r of 5 mm from a 100 mW source. The perfusion constants are from top to bottom, $\tau$ = 1000s, $\tau$ = 300s, $\tau$ = 100s, and $\tau$ = 50s respectively.[14]

700 nm are called infrared radiation. Infrared radiation is generally broken up into four categories near infrared (700 nm to 1,100 nm), shortwave infrared (1,100 nm to 3,000 nm), mid-wave infrared (3,000 nm to 5,000 nm), and long-wave infrared (7,500 nm to 13,500 nm).[17] Thermal imaging systems typically measure the intensity of radiation in the long-wave infrared regime. The human body has a temperature of approximately 37 °C and applying equations 1.1 and 1.2 the emitted peak wavelength is approximately 9,343 nm. This wavelength is in the middle of the long-wave infrared regime. Therefore if you wish to compare the relative temperatures of two objects a thermal camera is an ideal tool. A typical thermal image is shown in Figure 1.9. Figure 1.9 shows the color mapping typically used for thermal images, hotter/brighter objects appear red while colder/dimmer objects appear blue.

Enhanced thermal imaging is the combination of standard thermal imaging with selective heating of blood. The selective heating in this case is a contrast inducing technique to improve the contrast ratio between an object of interest and the background.[1–3,18] Contrast inducing techniques can either be physical, optical, or computational. In the following work two contrast inducing techniques were used

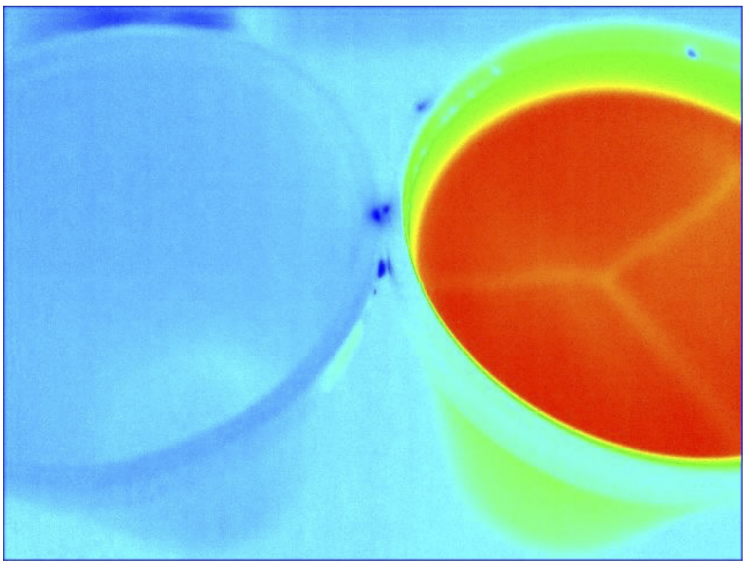

Figure 1.9: Standard thermal image of two cups side by side, one filled with cold water and the other filled with warm water. The brighter of the two is the coffee cup while the darker is the cup of water.

simultaneously, selective heating and real-time filters. Selective heating is an optical contrast agent that increases the temperature of a specific object relative to the surrounding medium based on the object's absorption properties. Real-time filters are a computational contrast inducing technique that rely on either subtracting the steady state heat solution of the system, or removal of the background radiation through differencing frames or complex derivatives. The use of contrast inducing techniques can delineate the margins of features that would normally be unresolved because of the low temperature contrast to the background.

We have discussed how different materials absorb different wavelengths of light based on their molecular makeup. Biological tissue has been shown to be a heterogeneous medium with many different biological components. Each of these components has its own distinct absorption properties and may absorb readily at certain wavelengths while other tissues do not absorb at the same wavelength. This can be limiting or advantageous in biomedical imaging. Different constituents of the biological medium can be targeted based on their particular optical properties, and a thermal

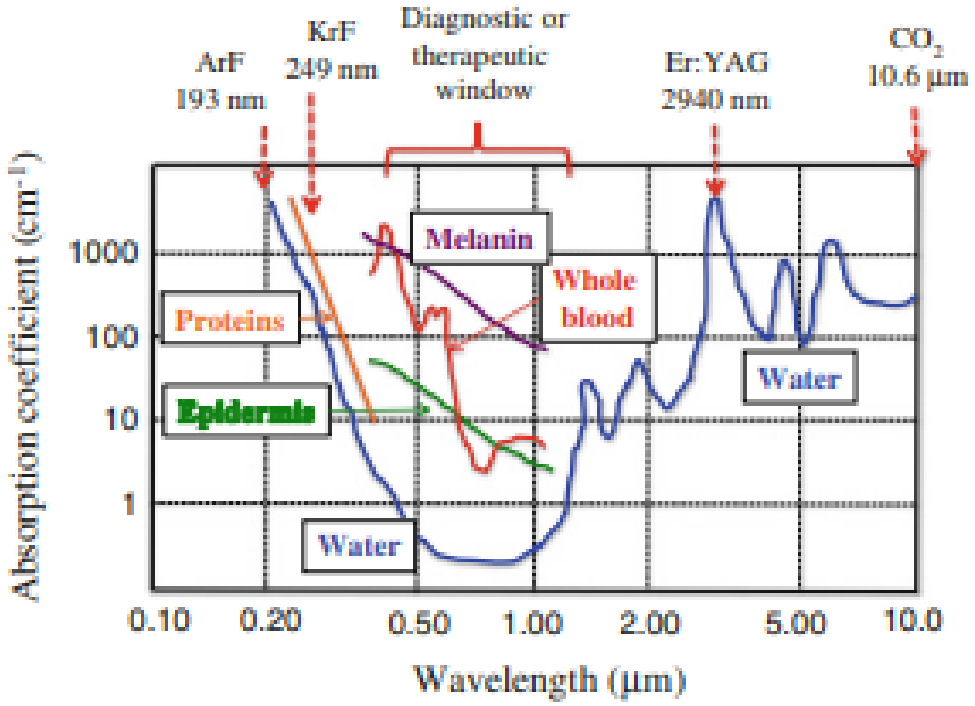


Figure 1.10: Absorption coefficients of different biological tissues as a function of wavelength. Also shown are the emission wavelengths of several optical lasers.[8]

contrast can be created relative to the surroundings.

Selective heating is a process in which an object is heated relative to the surrounding medium based on its unique optical properties. In this study we selectively heat blood-rich tissue that is embedded in water rich tissue. Due to its high concentration of hemoglobin, human blood readily absorbs light at 530 nm. Therefore, illuminating human tissue that has embedded blood vessels with this wavelength of light will selectively heat the blood vessels relative to the surrounding tissue. Figure 1.8 shows a comparison of the absorption spectrum for whole blood compared to water. Figure 1.8 shows that for whole blood there are two large absorption peaks. The first, and larger of the two, is just below 500 nm and, and the second, and weaker of the two, is above 500 nm. The absorption coefficient for water increases as the wavelength of light gets shorter than 500 nm, and longer than 1000 nm. While the absorption coefficient

for whole blood is always much larger than for water, the absorption coefficient for water is below 1 $cm^{-1}$ for the wavelength slightly larger than 500 nm. Using a LED with a peak wavelength of 530 nm can create a large temperature contrast between the illuminated blood and surrounding tissue while not significantly increasing the temperature of the surrounding tissue.

Enhanced thermal imaging can be used in two different modalities, direct illumination and indirect illumination. In the direct illumination mode, the region of illumination is the region being imaged. Indirect illumination images a region that is down-stream (in reference to blood flow) from the illumination site. Direct illumination is the modality used in the previous studies that measured tumor growth in a murine model.[2] This modality is ideal for solid mass tumor delineation, and for dermatologist that may have to look over many moles on a patient and determine which may be cancerous. Indirect illumination is ideal for surgical guidance and micro-vascular surgery. The flow of warm blood is imaged in this modality and the ability to see if the blood is flowing without the use of injected contrast agents is a powerful tool for surgeons. This dissertation further explores both direct and indirect illumination.

## 1.6 Summary of Previous Work

### 1.6.1 Using LED Sources to Selectively Heat Blood for Enhanced Mid-IR Imaging of Vascular Structures

A comparison between the heating rates of non-coagulated blood when illuminated by a high powered LEDs with wavelengths of 530 nm and 405 nm was performed in earlier work.[1] It was determined that the rate of temperature change of whole blood is higher when illuminated by the 405 nm LED. However, the maximum temperature the whole blood reached is greater than the bio-heat shock temperature and could be dangerous for clinical use. Using the 530 nm LED instead allowed for a more controllable temperature change over a longer period of time. This means that in

clinical use the potential damage to surrounding tissue and whole blood is greatly reduced.

### 1.6.2 Non-invasive Enhanced Mid-IR Imaging of Breast Cancer Development

Previously a murine model was used to image and monitor the growth of breast cancer tumors. The tumor volume was measured via physical caliper measurements, standard thermal imaging, enhanced thermal imaging, and fluorescent imaging.[2] This study showed that ETI could accurately measure the tumor volume in comparison to fluorescent imaging and physical caliper measurements. Enhanced thermal imaging allowed for the visualization of the peri-tumor region that exists around solid mass tumors and is targeted for excision.

## 1.7 Goals of this Dissertation

### 1.7.1 Real-time Image Acquisition

The previous studies showed that ETI is a viable method for delineating blood/blood vessel and tumor margins.[2,3] However, ETI required lengthy post-processing to identify blood-rich regions and could not be used in real-time. The objective of this study was to show that a combination of selective heating and enhanced thermal imaging could be performed in real-time, at an acceptable video frame rate, and that the transition to real-time measurements did not decrease the viability of the method as an accurate means to detect blood vessels. The results of the real-time imaging implementation and imaging results will be discussed in Chapter 2.

### 1.7.2 Computer Simulations of ETI

The previous studies showed that a combination of enhanced thermal imaging with selective heating is a viable method for delineating blood/blood vessel and tumor margins while being acquired in real time. However, in order to further our understanding of the thermodynamic processes that dictate the radiation and diffusion of thermal energy within tissue, a computational model was utilized. The use of the open source

MCMatlab model allows an easy way to monitor the temperature change of multiple tissue types simultaneously.[11] Use of this modeling software has allowed for an optimization of the previously described ETI system in respect to illumination power and illumination time. The use of this model determined which illumination powers and times would be adequate to heat the embedded blood vessel to a desirable temperature while ensuring the epidermal tissue layer did not reach temperatures that could cause damage. These models were used to create a quantitative model to measure the depth and width of embedded vessels. The results of the modeling are presented in Chapter 3.

### 1.7.3 Using ETI to Access Perfusion in Skin Grafts

After establishing the viability of ETI as a real-time imaging technique and using models to quantify the depth and width of embedded vessels, the final objective of this work is to show the capabilities of ETI as a means to monitor wound healing. Adequate blood perfusion is essential for healing and ETI offers a way to detect and monitor perfusion during the healing process. For these studies healing of skin autografts in a murine model were monitored for 12 days post-surgery using ETI in direct illumination mode. ETI was compared to imaging using a fluorescent dye that is currently used clinically that allows detection of blood vessels.

# CHAPTER 2: ENHANCED THERMAL IMAGING TO DETECT MICROVASCULATURE DURING SURGERY: REAL-TIME ACQUISITION

## 2.1 Introduction

Enhanced Thermal Imaging (ETI) is a new thermal infrared imaging modality that uses heat as a contrast agent to visualize microvasculature embedded in soft tissue. ETI is a combination of thermal IR imaging (8 - 10 $\mu$m) and selective heating of blood relative to surrounding water-rich tissue.[1–3] Blood absorbs light strongly at 530 nm, while absorption by soft tissue is lower at this wavelength.[19] Illuminating tissue containing blood vessels with a 530 nm LED at low power heats the blood ($\leq$ 0.5 °C) relative to the surrounding water-rich tissue. The resulting difference in temperature increases the contrast between the vessels and the surrounding tissue making the vessels more apparent in the thermal images. ETI, unlike standard thermal imaging, is a modality capable of specifically targeting blood vessels for imaging. This imaging technique is non-destructive and does not require the use of IV contrast agents making it an imaging tool that could be used for surgical guidance during procedures such as the delineation of margins around solid mass tumors, assessment of the perfusion of skin flaps during reconstructive microsurgery, evaluation of the perfusion in regions around complex closures during amputation and determination of boundaries for excision of burned tissue.

Inadequate tissue perfusion can cause complications secondary to tissue ischemia following a variety of surgical procedures. Surgical site necrosis can result in prolonged healing and/or require secondary corrective procedures. Palpation of pulses, assessing bleeding at cut edges and observation of tissue color have been the primary means of evaluating tissue perfusion intraoperatively. However, clinical examination

alone is often insufficient for accurately predicting surgical site necrosis.[20–23] Duggal et al. showed that the introduction of an additional intraoperative assessment tool, indocyanine green angiography imaging, reduced the incidence of skin necrosis by almost 10%.[22] Indocyanine green angiography (IGA) has since been successfully used as an adjunct to physical examination in a variety of surgical procedures including the detection of skin flap and superficial tissue viability in plastic, vascular, and general surgery.[20,21,24–30] However, ICG angiography is an invasive procedure that requires the intravenous application of a fluorescent dye. Contraindications such as iodide allergy or renal failure limit/prohibit the use of the imaging tool for some patients. Further, ICG angiography is a non-continuous imaging modality (limited by available dye volume and time of fluorescence). This non-continuous nature of ICG angiography requires careful pre-operative planning, limits the flexibility of this technique during procedures, and makes postoperative bedside monitoring expensive and difficult.[22] An imaging modality that does not require the use of dyes that could be used both intraoperatively and to monitor perfusion during the healing process could improve patient outcomes.[24] While indocyanine greeen angiography imaging (ICGI) offers intra-operative methods for assessing perfusion and graft/wound viability other less invasive techniques using thermal imaging and near-infrared spectroscopy are also becoming available.[24,31–36] Han et al. shows that indocyanine green angiography imaging outperformed standard thermal imaging in assessments of vascular morphology, and post-procedure tissue viability.[31] Therefore an improved thermal imaging based assessment is needed for it to become an intraoperative or bedside capable replacement for indocyanine green angiography. ETI may offer such an improvement to thermal based intraoperative guidance, and post-procedure tissue viability assessment.

In previous work, we successfully highlighted the blood-rich vascular region that is routinely targeted for surgical excision around mammary tumor masses in a murine

model.[2] Fluorescent, standard thermal and enhanced thermal imaging modalities, as well as physical caliper measurements, were used to monitor breast cancer tumor volumes over a 30-day study period. The tumor volumes estimated from all imaging modalities showed exponential growth over the study period. A strong correlation was found between tumor volumes estimated using fluorescent imaging, standard IR imaging and caliper measurements with enhanced thermal imaging, indicating that enhanced thermal imaging monitors tumor growth. Further, the enhanced IR images reveal a corona of bright emission along the edges of the tumor masses associated with the vessel-rich peri-tumoral zone. In another previous study, ETI was used to map the flow of blood through vasculature in porcine heart tissue *ex vivo*.[1] The LEDs were used to heat the blood and the flow of the heated blood was mapped downstream from the illumination site. A time derivative analysis highlighted the path of the selectively heated blood through the surrounding tissue and a spatial derivative analysis was also applied to the images to reveal the edges of blood vessels. The study demonstrated that ETI can be used to map embedded blood vessels and has potential applications in surgery.

In our previous studies, clear delineation of vessel morphology required significant post-acquisition processing using temporal and spatial filtering algorithms. While the method was promising as a surgical guidance tool, in our previous work ETI was not a real-time imaging technique. The real-time acquisition of imaging is a crucial step in the development of this technique for real-time surgical guidance. In this work, we describe recent efforts to apply the spatial and temporal filtering as imaging is acquired and thus enable real-time ($\geq$ 1 fps) acquisition of images.

## 2.2 Methods

### 2.2.1 Experimental Setup and Tissue Models

In all experiments a FLIR A6c series mid-IR camera (sensitive 7.5 - 14 $\mu$m) with an array size of 320 x 240 pixels and maximum frame rate of 60 fps was used for

imaging. The camera has a thermal resolution of $\sim$ 30 mK and emissitivity of the object was assumed to be 0.95. The camera was turned on approximately 10 minutes before imaging sessions began. Two sets of experiments were conducted.

In the first set of experiments, thinly sliced porcine tissue ($\sim$ 0.8 mm thick) was layered to surround and cover a small section of empty surgical tubing (0.5 cm diameter, length $\sim$ 30 cm) that was used to simulate a blood vessel. These experiments did not employ LEDs to selectively heat blood. The temperature contrast between the porcine tissue and the simulated vessel (the tubing) was induced by the flow of warm water through the tubing. This setup is shown in Figure 2.1a. In these experiments the working distance between the camera and tissue surface was 27 cm yielding a spatial resolution of 0.375 mm/pixel. Experiments were conducted with the tissue at room temperature (18°C). Warm water (T $\sim$ 30°C ) was then introduced into the tubing. A 2-minute video using a frame rate of 7 fps was recorded using the FLIR camera. Temporal and spatial filters were applied to the video as it was acquired (in real time). The procedure was repeated three times (N =3) with each trial separated by $>$ 5 minutes to ensure the tissue and tubing returned to equilibrium temperatures between imaging sets.

In the second set of experiments, intact porcine hearts and porcine blood (Animal Technologies, Inc.) were used. The research lab is certified as a Bio-safety level 1 laboratory, ensuring proper use and disposal of animal tissues. Two 530 nm LEDs were used to selectively heat blood and induce a temperature contrast between the blood and surrounding tissue (see Figure 2.1b). The working distance between the camera and tissue was 20 cm yielding a spatial resolution of 0.298 mm/pixel. Three existing vessels were identified and selected for ETI. The blood vessels were flushed with a saline solution to clear any obstructions before ETI experiments began. The porcine heart and blood were allowed to reach room temperature ($T = 20°\text{C} \pm 0.8°\text{C}$). Blood was injected into a vessel using a hypodermic needle. The vessel was illuminated 0.5

cm downstream from the injection site with a 530 nm LED (Thorlabs), using an LED spot with 0.5 cm diameter yielding a power density of 12.8 mW/cm$^2$. A video (60 fps) was recorded using the FLIR mid-IR camera, as the porcine blood was injected into and flowed through the vessel. During imaging temporal and spatial filters were applied to the video as it was acquired. After imaging, the heart tissue was dissected and the depth and width of each blood vessel was measured using a ruler.

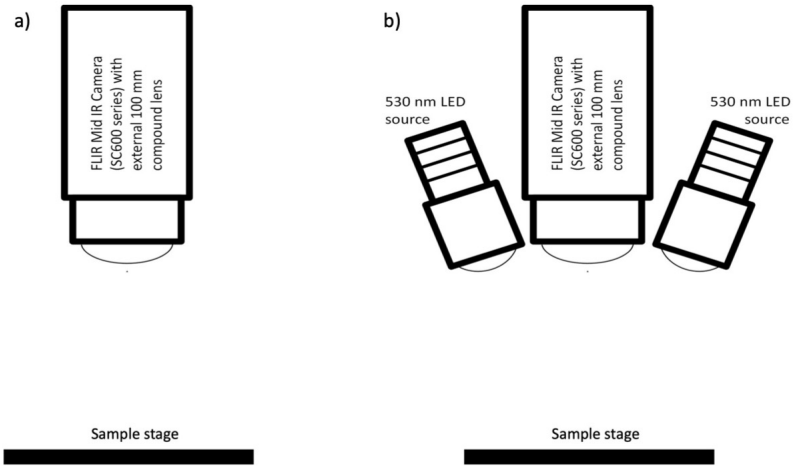


Figure 2.1: Schematic of the imaging setup for the layered porcine tissue model (a) and for the porcine heart tissue (b). The thermal camera imaged the sample from above as shown in both cases. LEDs were not used for heating in the layered porcine tissue experiments. Instead, warm water flowing through the tubing provided a temperature contrast between the simulated vessel and the surrounding tissue. For the porcine heart studies, two 530 nm LEDs were used to illuminate the tissue and the thermal camera was used to measure the temperature contrast between injected porcine blood and the surrounding tissue.

### 2.2.2 Image Filters Applied In Real-time

In both sets of experiments, a temperature contrast between the tubing/vasculature and the surrounding tissue was created. We applied both a temporal and spatial derivative analysis to highlight this temperature contrast. This analysis was performed in real time - that is the analysis was done as the video was acquired. No post-acquisition processing was required. In our previous studies, significant post-processing was necessary to apply the temporal and spatial derivative filters. MAT-

LAB was used to overlay a filter algorithm in the output video from the FLIR camera. The active application of the analysis filters resulted in a reduction of the frame rate from approximately 60 fps in the unprocessed video to approximately 1 fps for the temporal derivative filtered videos, and 30 fps for the spatial derivative filtered videos.

The temporal derivative filter averaged the first 10 frames (approximately 0.17s) of the video to create a baseline image. This baseline image was obtained as the blood was introduced into the vessel and before LED illumination. This baseline image was then subtracted from each subsequent frame of the video so that each output frame shows the temperature difference between that frame and the baseline image. This resulted in a 2D map highlighting pixels in which rapid temperature change occurred.

The spatial derivative filter used the Prewitt method defined in MATLAB. The Prewitt gradient operator employs the weighted sum of the 3 x 3 pixels in the neighborhood of the pixel of interest.[37] This filter emphasizes differences that occur at temperature boundaries. The pixel-by-pixel difference was determined and represented in a 2D map. Each pixel in the map represents the weighted temperature difference between it and its neighbors within the 3 by 3-pixel area. This produced a 2D map highlighting pixels that exhibited a temperature difference with neighboring pixels. This filtering process was applied to each frame of the video as it was acquired.

## 2.3 Results and Analysis

### 2.3.1 Enhanced Thermal Imaging of a Layered Porcine Tissue Model

Figure 2.2 shows frames from the video of the layered porcine tissue model with embedded surgical tubing (tubing was 1.66 mm below the tissue surface). The first column displays the standard thermal image (no spatial or temporal filters applied), the second column is the image after the application of the temporal derivative filter, and the last column is the image after applying the spatial derivative filter. The scale bar shown at left is the temperature scale for the first column of images (no filter applied). The first row shows images obtained before warm water was introduced

into the tubing ($t = 0$ s). The tissue and tubing are at the same temperature (room temperature) so the tubing is not evident in these images. The second row shows images captured as the warm water was introduced into the embedded tubing. The arrows in the figure indicate the position of the ends of the tubing not covered by tissue. The visible ends of the tubing are warmer than adjacent regions in all three images, as expected. The last row shows images captured 60 seconds after the warm water was introduced into the tubing. The tissue directly above the tubing was warmer compared to the surrounding tissue (by $\sim 1°$C) and is visible in all three images. However, the filtered images more clearly delineate the tubing. The temporal derivative filter successfully removes the background and clearly outlines the pixels that are changing temperature with time. The spatial derivative clearly defines the edges of the embedded tubing beneath the surface of the porcine tissue.

The tubing width was measured in the temporal derivative, spatial derivative and standard thermal images at $t = 60$s and then compared to the physical width. For the unfiltered and temporal derivative images, a line plot of the pixels across the tubing was created and this revealed a Gaussian-like profile of the temperature across the vessel, see Figure 2.3. The full width at half the maximum (FWHM) of a Gaussian fit to the profile was used to estimate the vessel width. The temperature profile in the spatial derivative images was not Gaussian see Figure 2.3. Instead, two peaks corresponding to the large temperature gradients at the edge of the vessels were seen. The pixel separation between these two maxima provided an estimate of the tubing width. Each of these measurements was repeated at five positions spaced equally along the tubing length and an average width was determined. In the standard thermal image (no filter applied) the width of the embedded tubing was 1.3 cm $\pm$ 0.1 cm, in the temporal filter image the width was 0.4 cm $\pm$ 0.3 cm and in the spatial derivative image the width was 0.53 $\pm$ 0.01 cm. The physical width of the tubing was 0.5 cm. Both the standard thermal and temporal filter images underestimate the width of

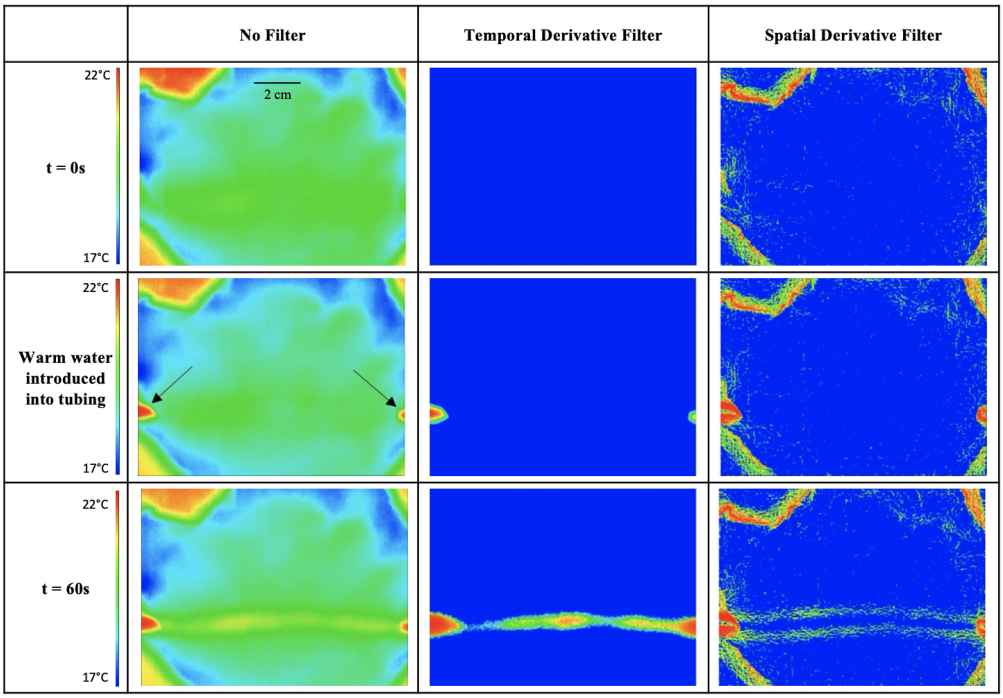


Figure 2.2: Frames from the layered porcine tissue model captured by the FLIR camera with no filter, temporal derivative filter applied, and spatial derivative applied. The first row shows the images before warm water was introduced into the tubing, the images shown in the second row were captured just as warm water was introduced into the tubing and the images in the third row were taken 60 s after the warm water was added. The scale bar shows the temperature in the images with no filters applied. The arrows indicate the position of the ends of the surgical tubing not covered by tissue. The temporal derivative filter shows a temperature difference of approximately $1°C$ compared with the surrounding tissue. The spatial derivative filter shows a temperature difference for each pixel compared to surrounding pixels.

the tubing and have larger errors. This is likely due to the fact that the edges of the tubing were cooler than the center and, as a result, the edges are not clearly defined in these images. The width measured in the spatial derivative filter is much closer to the actual tubing width and the error is smaller. This filtering algorithm clearly delineates the temperature boundary between warmer tubing and surrounding tissue making the spatial derivative images best suited for measuring the width.

### 2.3.2 Enhanced Thermal Imaging of Blood Vessels in Porcine Heart Tissue

Figure 2.5 shows frames from the videos taken of the porcine heart tissue for three different embedded vessels (referred to as Vessels 1, 2, and 3). The first column shows

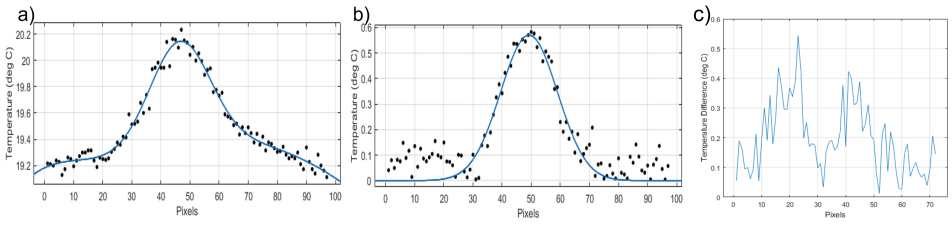


Figure 2.3: Graph of temperature as a function of position across the tubing as measured at t=60 s. a) Profile from the standard thermal image (no filters applied), b) profile from the temporal filter image, and c) profile for the spatial filter image.

the standard thermal image (no temporal or spatial derivative filter applied) and the second column is the image after the temporal derivative filter has been applied. The standard thermal image shown is from the same frame of the video as the filtered image to enable a direct comparison of these images. The third column is a second standard thermal image and the fourth column is the image after the spatial filter has been applied. Again, the standard thermal image shown is from the same frame of the video as the filtered image to enable a direct comparison of the images. In each standard thermal image (labeled as no filter in Figure 2.5), the LED spot position is noted by the red circle and the arrows indicate the direction of blood flow.

The temporal filter eliminates thermal emission from the surrounding tissue and allows for rapid delineation of vessel morphology and measurement of vessel length. Figure 2.4 shows the temperature as a function of position across a vessel. The profile is approximately Gaussian, but wings on either side of the central peak as seen in the standard thermal image are reduced with the application of the temporal filter. The spatial filter clearly outlines the edges of vessels and can provide measurements of vessel width. Both the temporal and spatial filters reveal more detailed information about the vessel morphology than is seen in the equivalent standard thermal image. For example, the temporal filter for Vessel 2 reveals a branching point that is not apparent in the standard thermal image. The existence of this additional vessel pathway was confirmed when the tissue was dissected at the end of the study.

Each vessel was dissected at the end of the study and depth and width were mea-

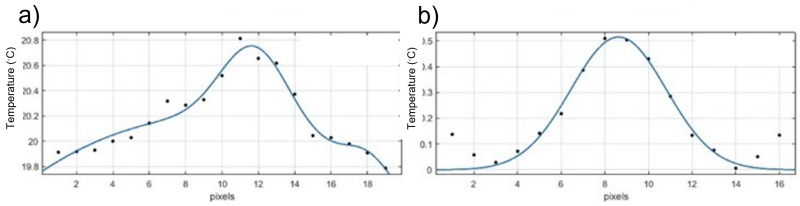


Figure 2.4: Graph of temperature as a function of position across Vessel 3. a) Profile from the standard thermal image (no filters applied), and b) profile for the temporal filter image.

sured at 6 points along the length of each vessel. The depths of the vessels were approximately constant along the length of the vessel with Vessel 1 having an average depth of 0.9 mm and Vessels 2 and 3 having an average depth of 0.6 mm. The widths of the vessels were also approximately constant along the entire length of each vessel.

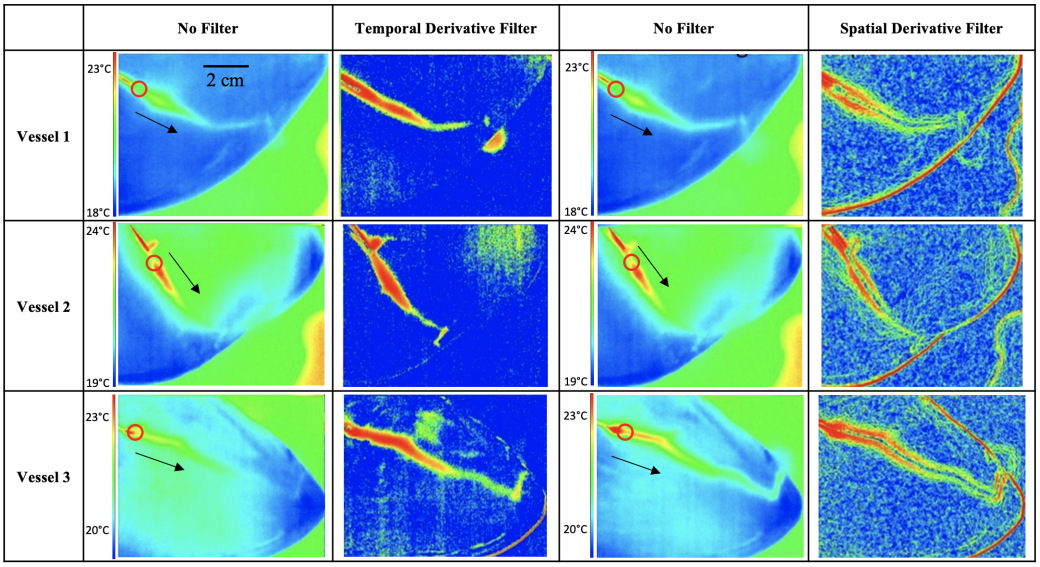


Figure 2.5: Frames from the video for blood flowing through vessels in porcine heart tissue with and without filters applied to the images.

#### 2.3.2.1 Time at Which Vessels Were First Detected

The time at which the vessels could first be identified in the standard thermal image was compared to the time at which the vessel was seen in the temporal filter image. Since the porcine heart and chosen vessels were visually inspected beforehand the

location of the vessel in the thermal image was known. When a temperature artifact appeared in this location with contrast greater than 0.1 °C relative to the surrounding tissue, and grew in length along the direction of blood flow, it was determined to be the vessel. The frame that this artifact began to grow in length was considered the frame of first appearance. In all cases, the vessels were evident in the temporal derivative image before they were detected in the standard thermal image. For vessels 1, 2, and 3 the temporal filter revealed the morphology of the vessel 1.445 s, 0.47 s, and 16.45 s more quickly than the standard image, respectively. As seen in Figure 2.5, the temporal filter clearly increases the contrast between the vessels and the surrounding tissue. The enhanced contrast provided by ETI revealed the morphology of the vessels more quickly than standard thermal imaging.

#### 2.3.2.2 Vessel Length Measurements

Table 2.1 compares the lengths of the vessels as measured in the standard and temporal derivative images with physical measurements of vessel length made after tissue dissection at the end of the study. The same frame of the video was used for making the length determinations in the standard and filtered images so that they could be directly compared. For each image the length was measured by placing a series of lines along the imaged vessel. The number of pixels along the series of lines was summed and then converted to centimeters based on the resolution of the camera. The measurements made with the temporal filter are closer to the physical length measurements, while those determined in the standard thermal image are shorter. The temporal derivative filter provided higher contrast images than the standard thermal images and more quickly and clearly revealed the path of the vessels downstream from the illumination site.

Table 2.1: Comparison of the vessel lengths, measured in cm, with and without the temporal filter applied along with physical measurements.

| Vessel | Standard Image | Temporal Filter Image | Physical Measurement |
|---|---|---|---|
| 1 | 3.80 ± 0.01 | 4.19 ± 0.01 | 4.00 ± 0.01 |
| 2 | 1.90 ± 0.01 | 3.90 ± 0.01 | 5.30 ± 0.01 |
| 3 | 3.20 ± 0.01 | 6.30 ± 0.01 | 6.20 ± 0.01 |

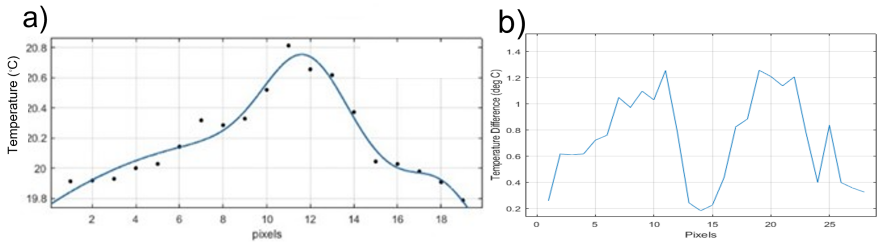


Figure 2.6: Graph of temperature as a function of position across Vessel 3. a) Profile from the standard thermal image (no filters applied), and b) profile for the spatial filter image.

#### 2.3.2.3 Vessel Width Measurements

Vessel widths were measured in the standard and spatial filter images at five positions along the vessel length spaced by equal intervals and these five measurements were then averaged. The same frame of the video was used for making the length determinations in the standard and filtered images so that they could be directly compared. Widths were calculated using the same method that was used to find the tubing width in the layered porcine tissue model describe in 2.3.1. A Gaussian fit was used to estimate the widths of vessels in the standard thermal images. An example of a vessel profile with the corresponding Gaussian fit is shown in Figure 2.6. The vessel profile in the spatial derivative images was not Gaussian. Instead, two peaks corresponding to the large temperature boundary at the vessel edges are seen (see Figure 2.6). Half the pixel separation between these two maxima provided an estimate of vessel width.

Table 2.2 shows the widths of the vessels measured in the standard and spatial derivative images, along with physical measurements made after tissue dissection.

The spatial filter highlights areas that show a steep spatial temperature gradient and clearly delineate the vessel edges (see Figure 2.5). The spatial derivative images provided more accurate widths than the standard thermal images when compared to the physical measurements. The widths measured in the standard thermal images are consistently larger than the physical measurements. The edges of the profile are not as clearly defined in the standard thermal image as in the filtered image (see Figure 2.2 resulting in an overestimate of vessel width.

Table 2.2: Comparison of the vessel widths measured in the standard thermal images and in the images with the spatial derivative filter applied. The physical measurements were made after tissue dissection at the end of the study.

| Vessel | Standard Image | Spatial Filter Image | Physical Measurement |
|---|---|---|---|
| 1 | 2.02 ± 0.61 | 1.05 ± 0.05 | 1.45 ± 0.18 |
| 2 | 2.87 ± 0.15 | 0.87 ± 0.05 | 1.25 ± 0.08 |
| 3 | 3.38 ± 0.17 | 1.26 ± 0.13 | 1.14 ± 0.23 |

## 2.4 Discussion

ETI combined with the application of a temporal derivative filter allows for rapid delineation of vessel morphology and accurate measurement of vessel length. The increase in contrast allows for the temporal filter to detect and map the vessels more quickly and accurately than standard thermal imaging. The application of the spatial derivative filter clearly delineates the vessel walls and can provide measurements of vessel width. In addition, the spatial filter images could be used to highlight the presence of occlusions in vessels. Previous studies performed using ETI required acquisition of standard thermal videos that then were exported to MATLAB for extensive post-acquisition processing and the application of the derivative filters. The spatial and temporal filters were applied in real time, as the videos were acquired, in this work.

This study demonstrates that enhanced thermal imaging is a promising real-time imaging modality that in the future could be used in medical applications that benefit

from accessing blood flow and delineating vascular morphology. Procedures including the creation of skin flaps/grafts during reconstructive microsurgery and complex closures during amputation would benefit from the use of ETI to map vessel structure and monitor perfusion. A combination of the spatial and temporal derivative filters could potentially delineate depth information of embedded structures in future applications. A demonstration of the real time capabilities of ETI were shown in this study. The application of those capabilities in an animal model are underway, and plans for a human clinical trial are being made to address the use of ETI in the clinical environment.

# CHAPTER 3: ENHANCED THERMAL IMAGING TO DETECT MICROVASCULATURE DURING SURGERY: QUANTIFYING DEPTH AND WIDTH

## 3.1 Introduction

Enhanced thermal imaging (ETI) is a combination of thermal IR imaging (8−10 $\mu$m) and selective heating of blood relative to surrounding water-rich tissue using LED sources at low power.[1–3] Blood absorbs light strongly near 530 nm, while absorption by the surrounding tissue is lower.[19] Illuminating soft tissue with embedded blood vessels with this wavelength of light induces a temperature contrast between the vessels and the surrounding tissue. This technique allows thermal imaging to target a specific tissue, blood vessels, for imaging. In previous studies, extensive post-acquisition processing of the images was necessary to highlight the presence of vascular structures. Recently, improvements to the acquisition software have enabled real-time imaging with this technique highlighting ETI's potential use as an intraoperative imaging tool.[18]

In a previous study, ETI was used to map vasculature associated with solid mass tumors. The tumor and surrounding tissue (which included embedded blood vessels) were directly illuminated with the LED and the vasculature in the illuminated region was imaged. This approach was used to outline the vessel-rich region around breast cancer tumors in an 4T1 murine orthotopic model. These regions are routinely targeted for surgical excision around solid mass tumors.[2] These studies demonstrated the possible application of ETI for margin delineation in cancer surgery. When ETI is used in this direct illumination mode, the depth to which blood vessels can be detected is limited by the penetration depth of the LED light and the resulting thermal

contrast that can be created between vessels and surrounding tissue.

ETI has also been used to map blood vessels in porcine heart tissue.[38] In these studies a vessel was illuminated and a then region of interest was imaged downstream of the illumination point. This process allowed vascular networks downstream from the point of illumination to be mapped in real time. These regions are routinely examined intraoperatively. For example, during plastic and reconstructive surgery reconnection of vascular structures is assessed to determine if perfusion is sufficient for tissue viability. This previous work demonstrated that ETI allows for real-time mapping of vascular networks. When ETI is used in indirect illumination mode the quality of mapping vascular regions is limited by the penetration depth of the LED light and the rate of blood flow.

Imaging techniques widely used for surgical planning include x-ray, computed tomography (CT) and magnetic resonance imaging (MRI). These imaging modalities are generally not available during surgery and both CT and x-ray imaging use ionizing radiation. These imaging modalities often require the use of contrast agents/dyes that are not tolerated by all patients. Indocyanine green angiography (ICGA) has been adopted for intraoperative use in plastic/reconstructive surgery. ICGA uses a dye that binds to blood and then fluoresces when illuminated by specific wavelengths of light. This technique can accurately map vascular networks during surgical procedures. However, ICGA requires the intravenous application of the fluorescent dye. Contraindications such as iodide allergy or renal failure limit/prohibit the use of the imaging tool for some patients. Further, ICG angiography is a non-continuous imaging modality (limited by available dye volume and time of fluorescence). This non-continuous nature of ICG angiography requires careful pre-operative planning and limits the flexibility of this technique during procedures. ETI is an imaging technique that does not require the use of injectable dyes, thus eliminating issues related to contraindication and continuous use inherent to ICGA, does not use ionizing radi-

ation like x-ray and CT and can be used intraoperatively unlike CT and MRI. The compact footprint of the imaging system could allow for use both during surgery and at the bedside.

In this study MCmatlab is used to simulate ETI by modeling the deposition of energy by a green (532 nm) LED into tissue and the resulting heating of blood vessels embedded in that tissue. MCmatlab integrates a Monte Carlo model for light transport in multi-layered tissue[10] with a three-dimensional finite element time-domain heat deposition and diffusion solver in a MATLAB-based user interface.[11] The goal of this study was to understand the limitations of detecting blood vessels when using ETI in both direct and indirect illumination mode and to determine optimum illumination parameters. In addition, the simulations provide insights on the effect of depth and width of embedded vessels on images captured with ETI. *Ex vivo* tissue experiments using porcine heart and skin tissue and vessels, were conducted and the results of these experiments were compared to the simulations.

## 3.2 Methods

For all simulations, a 1 $cm^3$ rectangular cuboid tissue model consisting of an air layer ($\approx$ 0.01 cm), an epidermis layer ($\approx$ 0.006 cm), a dermis layer ($\approx$ 0.984 cm), and a cylindrical blood vessel (radius = 0.05 cm or 0.1 cm) was used for all simulations (see Figure 3.1). This cuboid consisted of 250 x 250 x 250 voxels. The optical tissue properties at a specific wavelength (absorption coefficient $\mu_a$, scattering coefficient $\mu_s$, and the Henyey-Greenstein scattering anisotropy factor $g$) for the different tissue types were assigned to the voxels so that light propagation through the tissue could be modeled. The thermal properties (specific heat $c_v$ and the thermal conductivity $k$) of tissues were assigned on the same voxel grid. This allowed for the solution of thermal diffusion and heat transport within the tissue model and allowed for the solution of Arrhenius-based thermal chemical changes. The optical and thermal properties of the tissue layers used for all models were taken from Marti et al.[11]

Porcine skin, vessels dissected from porcine kidneys and porcine blood (Animal Technologies, Inc.) were used in the *ex vivo* tissue experiments. A FLIR A6c series mid-IR camera (sensitive 7.5 to 14 $\mu$m) with an array size of 640 x 480 pixels and maximum frame rate of 60 fps was used for imaging. The working distance between the camera and tissue was 14.5 cm yielding a spatial resolution of 0.185 mm/pixel. Two 530 nm LEDs were used to selectively heat blood and induce a temperature contrast between the blood and surrounding tissue (see Figure 3.2).

### 3.2.1 Direct Illumination Simulations

To model direct illumination ETI, an input LED beam was simulated by launching photon packets and calculating their paths in the simulated volume. All tissue types started at the same initial temperature in these models so that heating by the LED could be monitored. The depth of the embedded vessel was varied from 0.5 mm to 3.5 mm in 0.5 mm increments. MCmatlab includes a variety of beam types and the focus of these beam types can also be altered. For these simulations the tissue was illuminated with an LED emitter (532 nm) with a spatially flat, circular beam spot to simulate the LED used experimentally (1 cm in diameter; see Figure 3.2) The LED illumination power was varied from 0.1 W to 1 W in increments of 0.1 W. The tissue was illuminated for 1 s then thermal diffusion was modeled for 5 s after illumination ended. The temperature of the epidermis layer (directly above the embedded vessel), the dermis layer (between the blood vessel and epidermis), the top edge of the vessel, and the center of the blood vessel were all measured as a function of time.

### 3.2.2 Direct Illumination *Ex Vivo* Experiments

Thin slices of porcine skin tissue (varying thicknesses; see Table 3.1) were layered on top of vessels ($\approx$ 1 cm in length) dissected from porcine kidneys. A thick slice of porcine tissue ($\approx$ 2 cm in thickness) was placed underneath the vessels. The size, thickness, and length of each tissue slice and vessel were measured with a ruler and

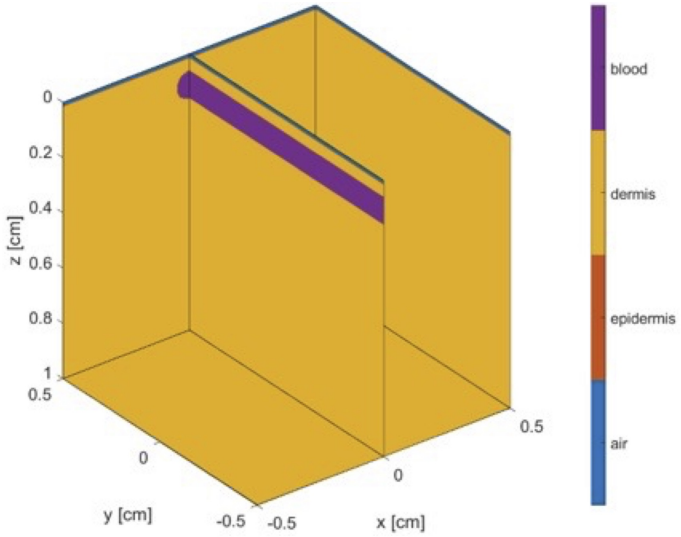


Figure 3.1: Geometry of the 1 $cm^3$ rectangular cuboid tissue model that consisted of epidermis, dermis and an embedded blood vessel.

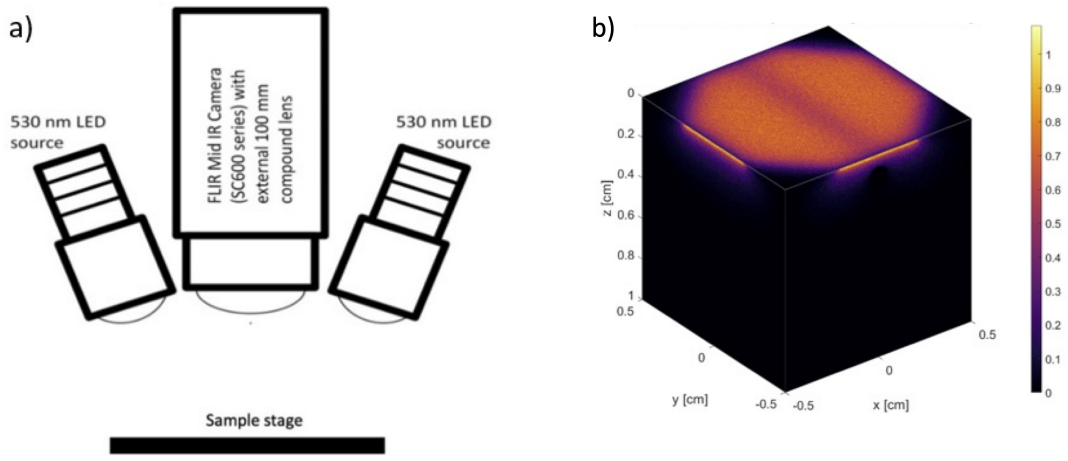


Figure 3.2: a) Schematic of the imaging setup used for the *ex vivo* tissue experiments. The thermal camera imaged the sample from above. Two 530 nm LEDs were used to illuminate the tissue and induce a temperature contrast. b) The normalized irradiance of the 532 nm source with a beam spot 1 cm in diameter simulated in MCMatlab. This type of beam was used in the tissue experiments.

Table 3.1: Table showing tissue depth and vessel diameters used for the *ex vivo* direct illumination experiments.

| Tissue Depth (mm) | Vessel Diameter (mm) |
|---|---|
| **0.584** | 2.056,0.834 |
| **0.600** | 0.784,0.644 |
| **0.622** | 0.784,0.644 |
| **0.666** | 0.702 |
| **0.696** | 0.784,0.644 |
| **0.770** | 0.784,0.644 |
| **0.826** | 0.784,0.644 |
| **0.888** | 0.762,1.258 |
| **0.918** | 0.784,0.644 |
| **1.006** | 0.784,0.644 |
| **1.034** | 0.762,1.258 |
| **1.038** | 0.784,0.644 |
| **1.048** | 0.762, 1.258 |
| **1.068** | 2.056,0.834 |
| **1.096** | 0.582, 0.248, 1.062, 1.296 |
| **1.158** | 0.702 |
| **1.370** | 1.296 |
| **1.420** | 0.702 |
| **1.440** | 1.222,1.318 |
| **1.548** | 0.784,0.644 |
| **1.548** | 0.784,0.644 |
| **1.588** | 1.222,1.318 |
| **1.768** | 0.702 |
| **1.824** | 0.702 |
| **2.042** | 1.222,1.318 |
| **2.466** | 1.296 |
| **2.578** | 0.702 |
| **3.188** | 0.702 |
| **3.854** | 0.702 |

digital calipers. The dissected vessels were filled with blood and the ends of the vessels were clamped. The porcine skin and dissected vessels were allowed to reach room temperature ($\approx 17°C$), and were then illuminated for one minute with two 530 nm LEDs (Thor Labs), using an LED spot with 1 cm diameter yielding a power density of 13.6 mw/cm$^2$. This is similar to the lowest simulated power, 0.1 W/cm$^2$. The dissected vessel and porcine tissue were then allowed to thermally relax for one minute after illumination. A 2 minute and 10 second video (25 fps) was recorded using the FLIR mid-IR camera before, during, and after illumination (see Figure 3.2). The temperature gradients produced along the surface of the tissue were measured before, during and after illumination allowing for the measurement of maximum temperature and temperature distribution along the tissue surface. These experimental results were then compared to the simulations. Note that there is a difference in illumination times used in the simulations compared to the illumination times used for the *ex vivo* tissue experiments. The model does not include cooling mechanisms such as convective cooling at the tissue surface or cooling due to blood perfusion. In the *ex vivo* experiments, the tissue temperature plateaus during extended illumination as heating by the LED is balanced by cooling. Longer illumination times in the simulations resulted in unrealistic heating not seen in tissue experiments due to the lack of cooling. Shortening the simulation time allows modeling of the heating of the tissue before these cooling effects become important.

### 3.2.3 Indirect Illumination Simulations

Upstream illumination was modeled by embedding a heated vessel in the tissue model (see Figure 3.3). LED illumination was not included. The direct illumination models were used to determine appropriate temperatures for the embedded vessels. The initial temperature of the embedded blood vessels was varied from 36 °C to 39 °C. The tissue was allowed to thermally relax for 20 seconds. The temperatures of five places across the surface of the epidermis were measured as a function of time

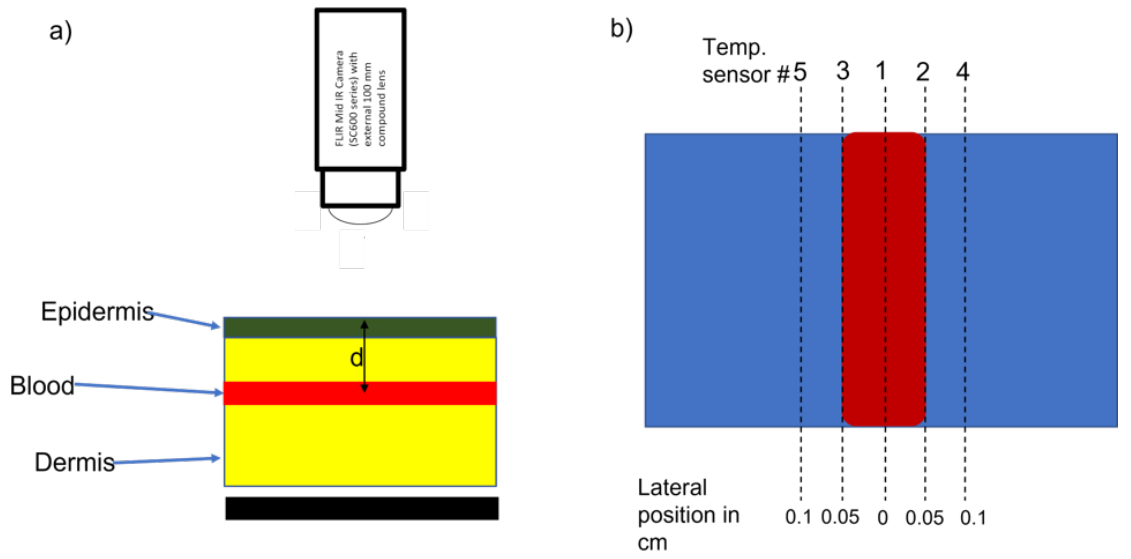


Figure 3.3: a) Illustration showing the 1 cm thick tissue model that consists of an epidermis layer, and a layer of dermis with an embedded blood vessel, b) the surface of the same tissue model with markers showing the lateral placement of the temperature sensors.

(see Figure 3.3).

### 3.2.4 Indirect Illumination *Ex Vivo* Experiments

Three *in situ* blood vessels were identified in porcine heart tissue. The blood vessels were flushed with a saline solution to clear any obstructions before ETI experiments began. The porcine heart and blood were allowed to reach room temperature (T = 20°C). Blood was injected into each vessel using a hypodermic needle. The vessel was illuminated 0.5 cm downstream from the injection site by two 530 nm LED (Thorlabs), using an LED spot with 1 cm diameter yielding a power density of 13.6 mW/cm$^2$. A video (25 fps) was recorded using the FLIR mid-IR camera, as the porcine blood was injected and flowed through the vessel. After imaging, the heart tissue was dissected and the depth and width of each blood vessel was measured using a ruler and digital calipers. Measurements of depth and width were taken at five locations along the vessels and these values were averaged. Table 3.2 shows the depths and widths of the vessels used in this study.

Table 3.2: Depth and width measurements determined using a ruler or digital calipers after dissection.

| Vessel # | Depth (mm) | Width (mm) |
|---|---|---|
| 1 | 0.90 ± 0.14 | 1.64 ± 0.40 |
| 2 | 1.16 ± 0.08 | 0.92 ± 0.12 |
| 3 | 0.58 ± 0.04 | 0.68 ± 0.19 |

## 3.3 Results

### 3.3.1 Direct Illumination Simulation

The maximum recorded temperatures for the epidermis, dermis, top edge of a 1 mm diameter blood vessel and center of the vessel versus incident LED power for seven different vessel depths are shown in Figure 3.4 (a-g). As the LED power increases, the temperature of all tissues increases for all depths, as expected. The change in the maximum temperature for each tissue type is approximately linear as a function of power for each depth. In Figure 3.4 a, the temperatures of the epidermis and dermis layers are slightly higher compared to the other graphs. This is the result of the shallow depth of the blood vessel. The blood absorbs light and this results in local heating of the surrounding tissue. As the depth of the vessel increases the maximum temperature of the epidermis and dermis show little change from depth to depth (see Figure 3.4 b-g). The temperature of the top edge of the blood vessel is higher than the temperature of the center of the vessel for all powers and all depths (see Figure 3.4 (a-g)). The top edge of the blood layer strongly absorbs the 532 nm radiation, thus reducing the amount of energy available to be deposited at the vessel center resulting in less heating. Figure 3.4 (a-g) also shows that the maximum temperature of the top edge of the blood vessel and the temperature at the center of the vessel decrease as vessel depth increases. At a depth of 2 mm the blood is heated by $\leq 0.5$ °C even for the largest incident powers and at a depth of 3.5 mm there is little to no change in the temperature of the top or center of the vessel regardless of illumination

power. Previous studies have shown that a temperature difference of 0.5 °C along the surface of the epidermis is needed for accurate delineation of embedded vessels.[1–3,38] This suggests that in direct illumination mode, vessels deeper than approximately 2 mm will be difficult to detect.

Figure 3.5 (a-g) shows the maximum recorded temperature of all tissues when a 2 mm diameter blood vessel is embedded in the model. The same trends are present for the 2 mm diameter blood vessel as were seen for the 1 mm blood vessel (see Figure 3.4 (a-g)). Upon close inspection of Figures 3.4 and 3.5 it is noticeable that the maximum temperatures of the epidermis, dermis, and blood are much higher for the 2 mm diameter blood vessel than for the 1 mm vessel when the larger vessel is at shallow depths. This is due to the thicker layer of blood present at shallow depths for the larger vessel. This results in strong absorption and heating of the blood and surrounding tissue. Similar to the 1 mm blood vessel shown in Figure 3.4, the maximum temperature of the epidermis shows little dependence on the depth of the vessel for depths greater than 0.5 mm. Figures 3.4 and 3.5 show that the maximum temperature of the epidermis and dermis tissue does not depend on vessel depth if the depth is greater than 0.5 mm.

Figure 3.6 shows the evolution of the maximum temperature as a function of time for each tissue type for both the 1 mm and 2 mm vessel diameters. In the simulation shown, the tissue was illuminated with an LED power of 0.7 W. The 1 mm vessel was located at a depth of 0.5 mm and the 2 mm vessel was at a depth of 0.15 mm. The tissue was illuminated with the LED for the first second of the simulation and then thermal diffusion was monitored for 5 seconds after illumination ended. The temperature behaviors shown in Figure 3.6 are similar to those seen in simulations with different powers and different vessel depths, and are representative of the areas directly above the center of the embedded vessel. For both vessel diameters, the epidermis, dermis and top edge of the blood vessel heat quickly during the illumination

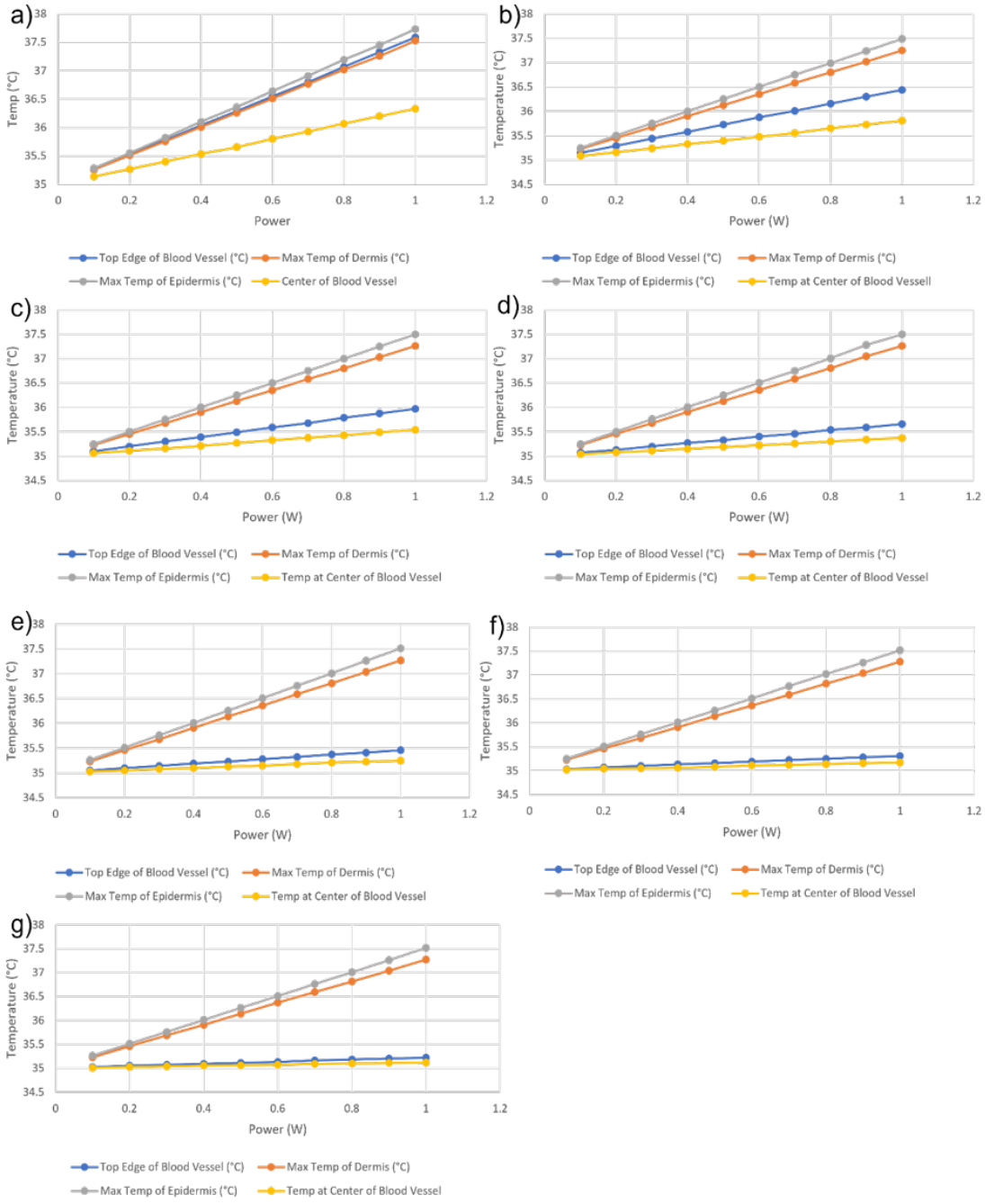


Figure 3.4: The maximum temperature of the epidermis, dermis, top edge of the blood vessel, and center of the blood vessel for a 1 mm diameter vessel at seven different depths: a) 0.5 mm, b) 1 mm, c) 1.5 mm, d) 2 mm, e) 2.5 mm, f) 3 mm, and g) 3.5 mm.

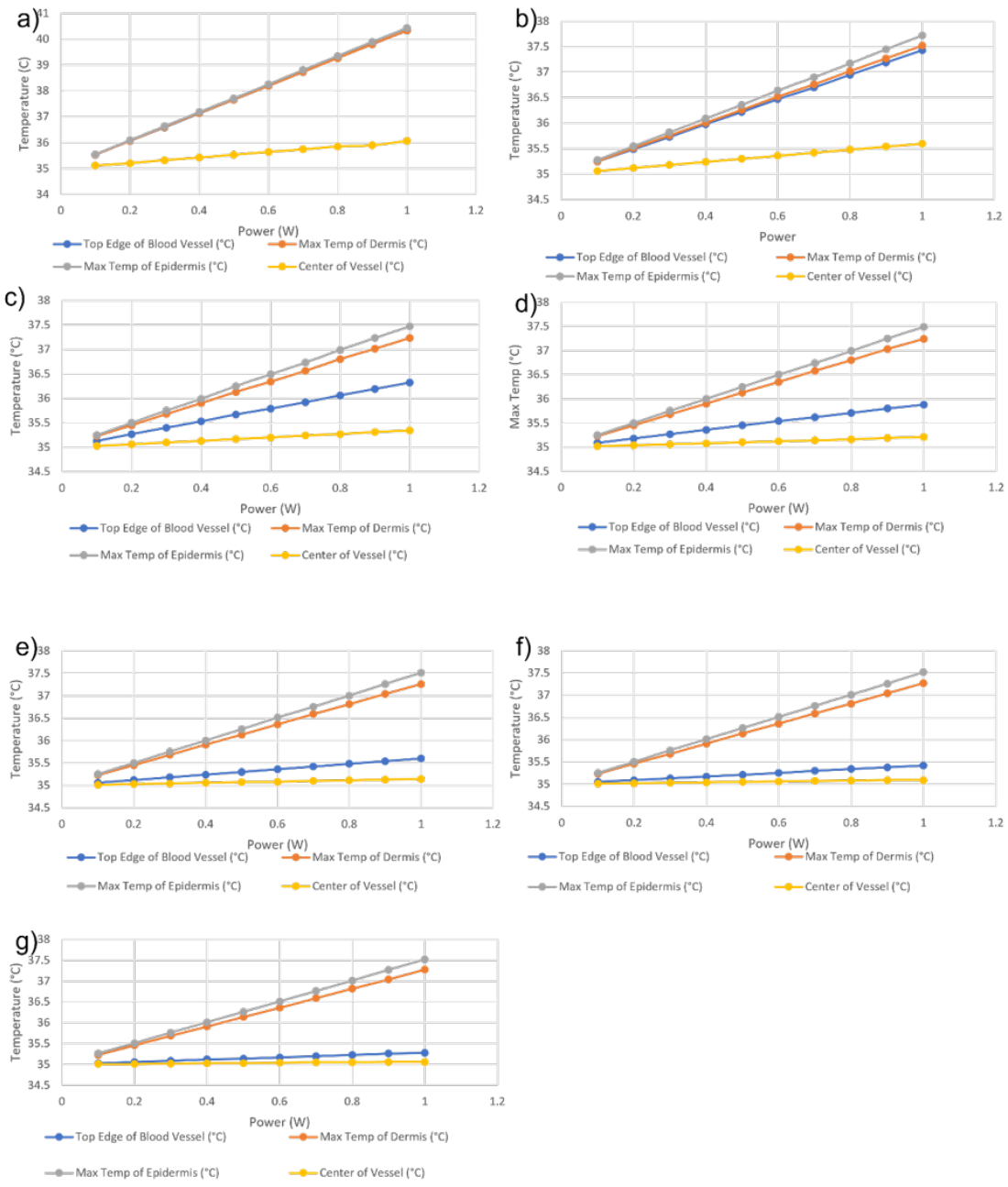


Figure 3.5: The maximum temperature of the epidermis, dermis, top edge of the blood vessel, and center of the blood vessel for a 2 mm diameter vessel at seven different depths: a) 0.15 mm, b) 0.5 mm, c) 1 mm, d) 1.5 mm, e) 2 mm, f) 2.5 mm, and g) 3 mm.

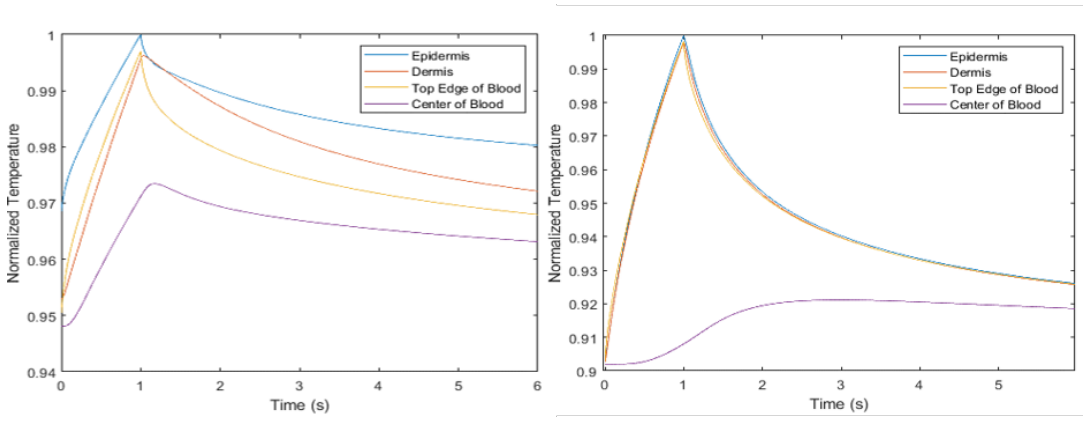


Figure 3.6: Temperature of each tissue type as a function of time. The tissue is illuminated with the LED at a power of 0.7 W for the first second of the simulation and thermal diffusion is monitored for 5 seconds after illumination ends. Panel a) is for a 1 mm diameter blood vessel embedded at a depth of 0.5 mm and panel b) is for a 2 mm diameter blood vessel at a depth of 0.15 mm.

phase and begin to cool after illumination ends. The center of the blood vessel heats more slowly in both cases. For the 1 mm vessel, the vessel center reaches a peak temperature approximately 0.2 s after the other tissue types. This effect is even more pronounced for the 2 mm vessel. For this larger vessel, the temperature of the center reaches its maximum temperature 1.7 s after the other tissue types. This slower heating rate is likely due to the fact that less LED light penetrates into the vessel center indicating that heating via diffusion plays a significant role in heating the vessel center. For the 1 mm vessel there seems to be some heating from illumination indicated by the shape of the curve (it is similar to the other tissues). For the 2 mm vessel, thermal diffusion appears to be the primary source of heating.

Figure 3.7 shows the temperature profile across the surface of the tissue at 1 s intervals for a simulation that did not have a vessel embedded in the tissue. The circular LED spot is visible in all images. These images are similar to what would be captured with a mid-IR camera. Figure 3.8 shows the same temperature profiles when a vessel is embedded at a depth of 0.5 mm (results for both a 1 mm and 2 mm vessel are shown). The t = 1 sec frame shows the temperature distribution at the end

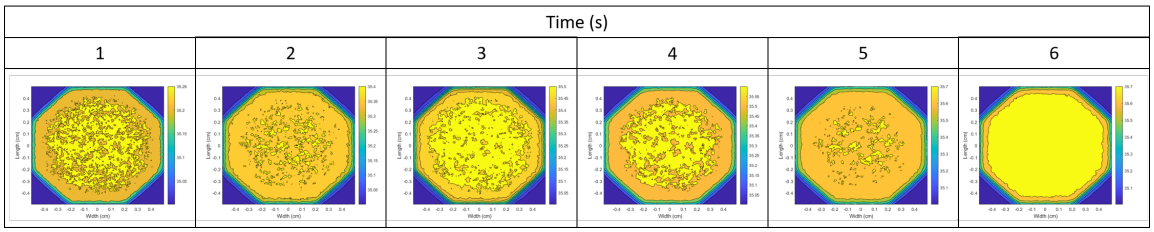


Figure 3.7: Temperature profile of tissue surface at 1 second intervals. This is simular to images that would be acquired by a thermal camera. The tissue was illuminated for 1 second with a 0.7 W, 532 nm LED and then the tissue was allowed to thermally relax for 5 seconds. In this case there was no embedded vessel.

of the illumination phase. The LED spot is evident in this image. For both vessel diameters shown in Figure 3.8, the embedded blood vessel is apparent at the end of the illumination phase as the bright yellow cylindrical structure. In comparison, no such structure is evident in the simulations without the vessel (see Figure 3.7). The temperature difference between the vessel and the surrounding tissue is $\approx 0.5$ °C for the 1 mm vessel and $\approx 2$ °C for the 2 mm vessel at the end of illumination. The temperature is highest just above the embedded blood vessel throughout the simulations and the vessel is apparent in all images. The tissue directly above the embedded vessel heats more quickly and to a higher temperature than adjacent tissue. As time progresses, the shape of the temperature profile above the vessel increases in width as heat diffuses from the embedded vessel laterally across the surface tissue.

Figure 3.9 shows the 2D temperature profile at the surface of the tissue for 1 mm and 2 mm diameter vessels embedded at depths of 0.5 mm, 1.0 mm, 1.5 mm, and 2.0 mm. The temperature profiles are from simulations using an LED power of 0.5 W. Each frame was chosen such that the temperature difference between the center of the area above the embedded vessel and the adjacent tissue was at a maximum. The time at which this maximum difference occurs is given in each panel and this time will be referred to as the signal arrival time. The time at which this maximum temperature difference occurs is a function of depth, but does not depend on the size of the vessel. The shallow vessels are detected more quickly than deeply embedded

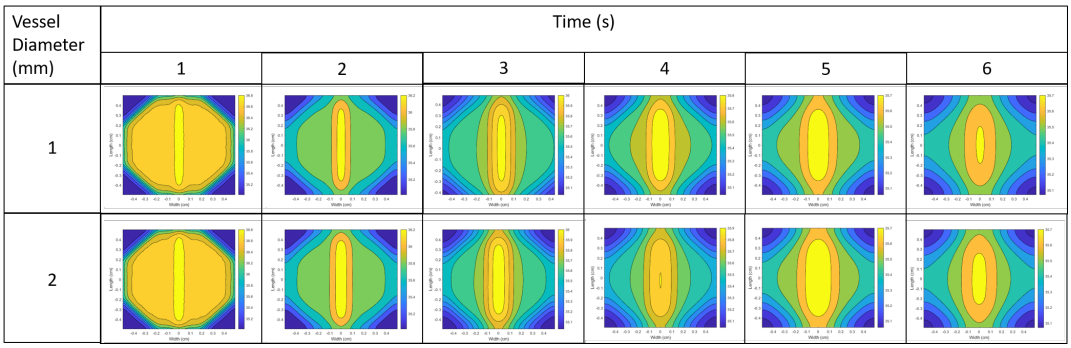


Figure 3.8: Temperature profile of the tissue surface at 1 second intervals. This is similar to images that would be acquired by a thermal camera. The tissue was illuminated for 1 second with a 0.7 W, 532 nm LED and then the tissue was allowed to thermally relax for 5 seconds. The top panel shows the resulting temperature profile for a 1 mm vessel embedded in the tissue and the bottom panel displays the temperature of the tissue surface above a 2 mm vessel. In both cases, the vessel was embedded $\approx$ 1 mm below the tissue surface.

vessels. Figure 3.10 (a) shows the signal arrival time for both diameter vessels at four different depths and three different incident LED powers (0.1 W, 0.5 W, and 0.7 W). The signal arrival time is linear with vessel depth and is independent of both the illumination power and vessel width. Figure 3.10 (b) shows the signal arrival time averaged over all sizes and powers at each depth. The linear fit provides a simple way to estimate the depth of a vessel based on the signal arrival time.

Figure 3.11 shows the measured full width at half maximum (FWHM) of the vessel profiles seen at the tissue surface as a function of time for both 1 mm and 2 mm vessels at two different depths. For panel (a) the vessels were embedded at 0.5 mm below the surface and in panel (b) the vessels were 1.5 mm below the surface. At each point on the graphs, the FWHM at 3 different powers has been averaged and the error bars are the standard deviation about the mean. The small error bars demonstrate that the FWHM and evolution of the FWHM with time does not depend on illumination power. Notice that in the two figures the times at which the FWHM values are measured is different. This is because it takes longer for the signal from the deeper vessel to arrive at the surface. In 3.11 (a), the 2 mm vessel has a wider profile than

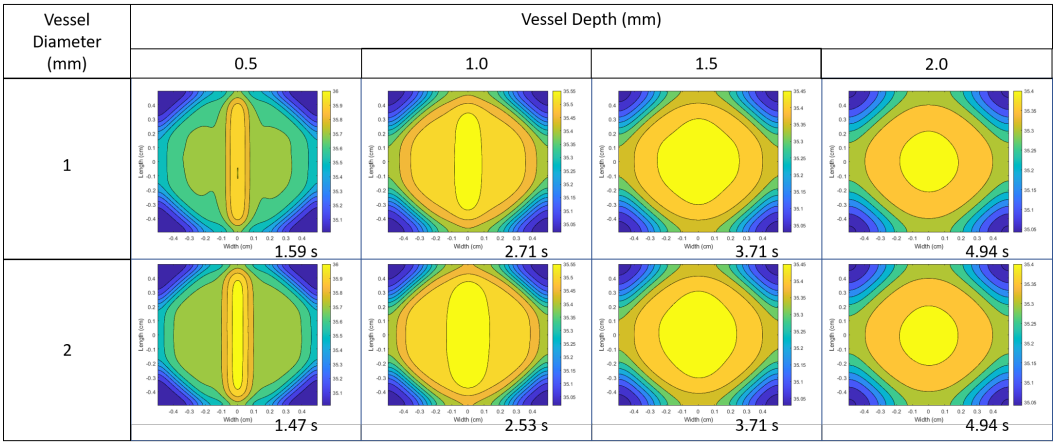


Figure 3.9: Temperature profiles of tissue surface when simulated with direct illumination by a 0.5 W, 532 nm LED. The first row shows results for the 1 mm diameter vessel while the second row is for the 2 mm diameter vessel. Each column shows simulated images for vessel depths from 0.5 mm to 2.0 mm. The time at which the temperature profile was taken is shown in the bottom right corner of each cell. The frames were selected based on when the maximum temperature difference between the center of the vessel and the surrounding tissue occurred.

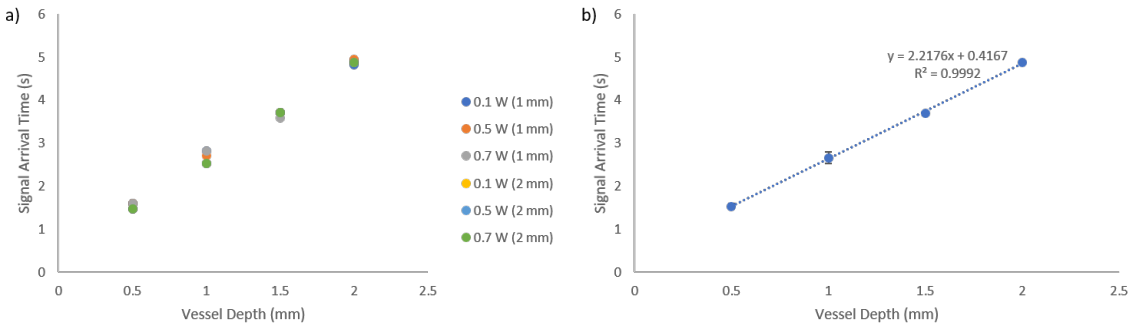


Figure 3.10: a) The signal arrival times for 1 mm and 2 mm diameter vessels for illumination with LED powers of 0.1 W, 0.5 W, and 0.7 W as a function of vessel depth. b) The average arrival time at each depth and the linear fit to these points.

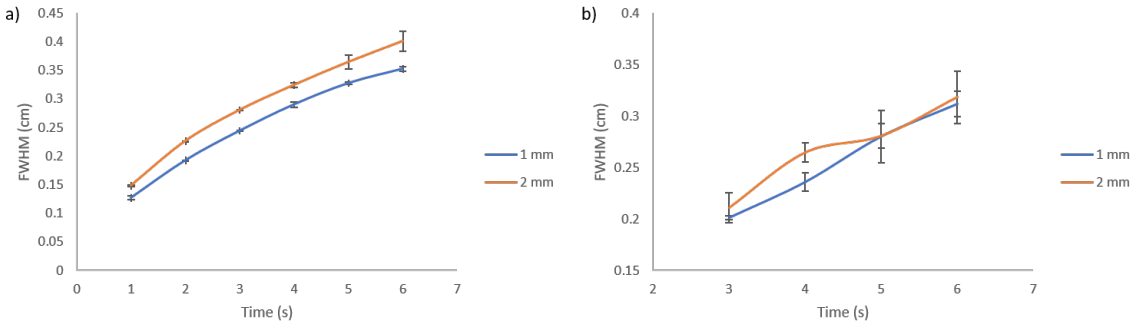


Figure 3.11: The full width at half maximum (FWHM) of the vessel profile at the tissue surface averaged for three different LED illumination powers: 0.1 W, 0.5 W, and 0.7 W. In panel a) both vessels are embedded 0.5 mm below the tissue surface and in panel b) the vessels are 1.5 mm below the surface.

the 1 mm vessel at all times. For both vessel sizes, the FWHM increases over time as the heat diffuses through the model. Figure 3.11 (b) shows the FWHM for vessels embedded at a depth of 1.5 mm. At early times, the FWHM for the 2 mm vessel is larger than for the 1 mm vessel, but as time progresses the sizes of these features approach the same value. This is the result of the evolution of the shape of the profile over time for more deeply embedded vessels. This profile becomes more circular and less cylindrical (see Figure 3.9) and it becomes more difficult to distinguish between different vessel sizes.

ETI used in direct illumination distinguishes the difference in the heating and cooling rates between the surface level tissue directly above the vessel compared to tissue adjacent to the embedded vessel. The depth and width of an embedded vessel can be estimated based on the signal arrival time and FWHM of the profile seen at the surface. First, the signal arrival time (independent of vessel width and illumination power) provides an indicator of vessel depth. Once depth is known, the width of the vessel profile at the surface can provide an estimate of vessel size.

An additional interesting effect is apparent in the simulated images. Figure 3.12 shows a temperature profile along the surface of the tissue for a 1 mm diameter vessel embedded at a depth of 0.5 mm and illuminated with an incident power of 0.1 W.

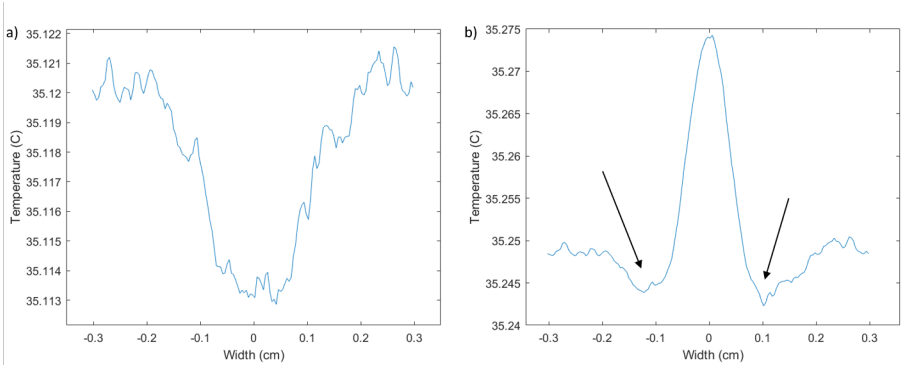


Figure 3.12: Temperature profile across the surface of the tissue for a 1 mm diameter vessel embedded at a depth of 0.5 mm and illuminated with an incident power of 0.1 W. Panel (a) is the profile a) t = 0.29 s (before the vessel is evident at the surface), and panel (b) is at t = 0.59 s (when the vessel is first seen at the surface.)

The profile shown is panel (a) is from t = 0.29 s after the start of illumination. The signal from the vessel has not yet reached the tissue surface. Panel (b) is at 0.59 s after the start of illumination and marks the time at which the vessel is first seen at the tissue surface. The tissue directly above the vessel is at a lower temperature than the surrounding tissue within the illumination spot at t = 0.29 s. This same effect is also seen after the vessel is apparent at the surface (indicated by the arrows in Figure 3.12 (b)). This behavior only occurs in the tissue layers directly above the embedded vessel. This small drop in temperature at the start of LED illumination can be attributed to the embedded vessel readily absorbing the thermal energy distributed in the tissue directly above it. This is due to the difference in thermal properties between the blood and porcine tissue. Blood has a higher thermal conductivity than tissue which allows it to readily absorb the thermal energy present at the surface. This intrinsic property of blood is what allows the vascular system of the body to regulate local temperature changes. This phenomenon was previously noted by Kolios et al.[15]

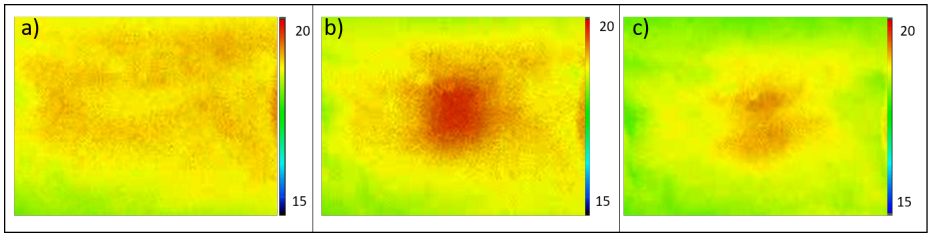


Figure 3.13: Thermal images of the surface of porcine tissue with an embedded vessel (diameter = 0.784 mm, depth 1.006 mm) a) before illumination (t = 7 s), b) during illumination (t = 45 s), and c) after illumination (t = 90 s).

### 3.3.2 Direct Illumination *Ex Vivo* Experiments

We compared the results of the *ex vivo* tissue experiments to those seen in the direct illumination simulations. The tissue depths used in the *ex vivo* experiments were similar to those modeled in the simulations. Figure 3.13 shows three images taken from a video during direct illumination of a vessel embedded in porcine tissue during the experiments. The first frame shows the initial temperature state of the tissue before illumination started (t = 7 s). The second frame shows the temperature distribution approximately halfway through the illumination period (t = 45 s). The final frame shows the temperature distribution after illumination has ended (t = 90 s). Figure 3.13 b shows a region of higher temperature (red), which is the spot of illumination and is similar to the distributions shown in figures 3.8 and 3.9. However, the spot seen in Figure 3.13 is not as well defined due to noise, inhomogeneous tissue and the thermal resolution of the camera. Figure 3.13 c shows the diffusion of the thermal energy laterally across the surface of the tissue after the illumination phase has ended. The red area present in Figure 3.13 b is no longer present in Figure 3.13 c demonstrating that the temperature change at the surface is no longer dominated by LED illumination. This is the same behavior seen in the simulations.

Figure 3.14 shows the temperature profiles for two vessel depths (1.006 mm and 1.548 mm) with the same vessel diameter (0.784 mm). The shapes of the temperature curves shown in Figure 3.14 are dominated by the heating caused by the LED illumi-

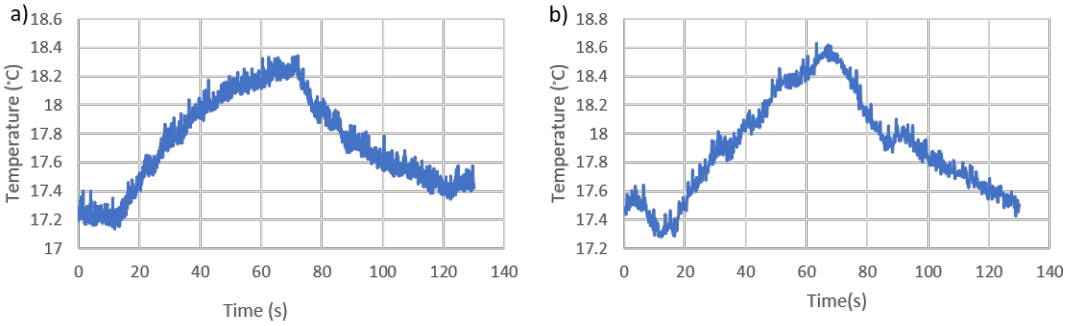


Figure 3.14: The mean temperature versus time graphs for vessel depths of a) 1.006 mm and b) 1.548 mm. The vessel diameter in both cases was 0.784 mm. LED illumination began at 10 seconds, and then the tissue was illuminated for 60 seconds. The tissue and vessel were then allowed to thermally relax for another 60 seconds. A small decrease in temperature is seen at the start of illumination (t= 10 s) and this is followed by an increase in temperature until 70 seconds (the end of LED illumination). The temperature then decreases until the end of the recording.

nation, resulting in the cresting wave shape. This same type of response was noted in the simulations. LED illumination began at 10 s, so the temperature measured before this time represents the equilibrium state of the tissue. There is a small dip in temperature at the start of illumination and then this is followed by an increase in temperature during LED illumination. At 70 s LED illumination ended and the temperature of the tissue begins to decline. The maximum mean temperatures (as measured by a mean ROI in FLIR ResearchIR software) reached in Figures 3.14 a and b are 18.34 °C and 18.63 °C, respectively. The surface heating resulting from LED illumination can be determined by averaging the temperature during the first 10 seconds (when there was no illumination) and then subtracting this value from the maximum temperature. For the 1 mm deep vessel (Figure 3.14 a) the change in surface temperature was 1.09 °C and for the 1.5 mm (Figure 3.14 b) vessel the increase in temperature was 1.02 °C. The change in the surface temperature does not depend on the depth of the vessel. This behavior was also noted in the simulations. The small drop in temperature at the start of LED illumination was also noted in the simulations.

Figure 3.15 a shows the maximum temperature change at the tissue surface as a function of depth for all experiments (this includes all vessel sizes). The maximum temperature change was determined by subtracting the temperature of the surface before illumination began from the maximum temperature of the surface recorded by the mid-IR camera during illumination. A Spearman correlation test was used to determine if a correlation between vessel depth and maximum surface temperature change exists. The Spearman coefficient ($\rho$) was determined to be -0.350, which falls below the critical $\alpha$ value of 0.246. This indicates with greater than 95% confidence there is a weak negative correlation. This is in agreement with the simulation results shown in Figures 3.4 and 3.5 and is consistent with the idea that LED illumination is the dominant factor driving the change in surface temperature for the tissue. Figure 3.15 b shows a comparison of the maximum temperature change for multiple vessel depths with two vessel thicknesses (0.644 mm and 0.784 mm). This plot also indicates that there is no distinct difference in the maximum temperature change at the tissue surface with vessel thickness. This is similar to the trends seen in the simulation data. Figures 3.4 and 3.5 showed the maximum temperature at the surface of the tissue changed minimally or not at all as the depth of the embedded vessel increased. The trends seen in the *ex vivo* tissue experiments indicate that for ETI in direct illumination mode the maximum temperature at the surface of the tissue is independent of vessel depth and size and this is in agreement with the MCmatlab simulations.

Figure 3.9 revealed that in the simulations the signal arrival time occurs later for deeper vessels and showed that as the vessel depth increases the area of maximum temperature increases radially in size, until it is approximately circular. Measurement of a signal arrival time was also attempted for the *ex-vivo* tissue samples. Figure 3.16 shows the temperature difference between the maximum temperature of the surface of the tissue directly above an embedded vessel compared to the temperature of surrounding tissue located 0.25 cm to the right of the vessel within the illumination

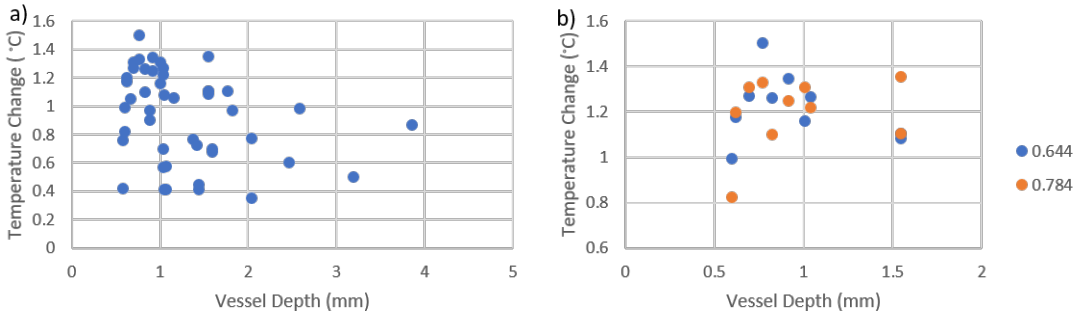


Figure 3.15: Maximum temperature change for a) all tissue thicknesses and their corresponding vessel thicknesses, and b) tissue thicknesses with the same vessel thicknesses (0.644 mm and 0.784 mm).

spot for both 0.748 mm and 0.644 mm diameter vessels. Figure 3.16 shows that for the *ex vivo* tissue studies there is no clear point of maximum temperature contrast. This is most likely due to the longer illumination times used in the tissue experiments. The maximum temperature contrast reaches a plateau that is maintained for a large amount of time ($\approx$ 40 s). Figure 3.16a shows a clear separation in the maximum temperature contrast for each vessel depth between 40 s and 60 s. However this same separation is not seen for the smaller diameter vessel (0.644 mm; see Figure 3.16b). To estimate the signal arrival time of the curves shown in Figure 3.16 a Gaussian curve was fit to each maximum temperature contrast curve, and the time of the Gaussian's maximum (the signal arrival time) was determined. Figure 3.17 shows the signal arrival times for both a 0.784 mm and 0.644 mm diameter vessel as a function of depth. This graph of arrival time versus depth for the simulations revealed a clear linear trend (see Figure 3.10). No clear trend in the signal arrival time versus vessel depth is evident in the *ex vivo* tissue studies. This is most likely due to the lower thermal and spatial resolution of the *ex vivo* experiments compared to the simulations.

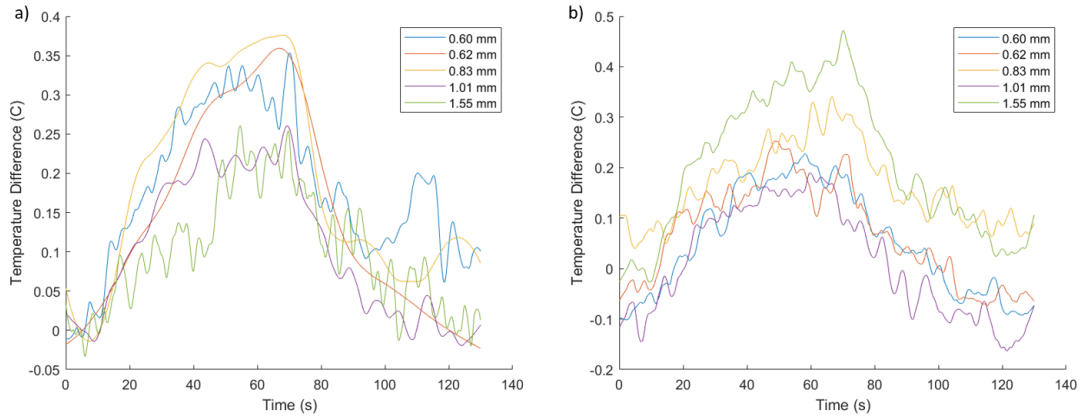


Figure 3.16: Temperature contrast between the maximum temperature of a point located on surface of tissue directly above the embedded vessel compared to the surrounding tissue located 0.25 cm to the right of the vessel within illumination spot measured during the *ex-vivo* tissue study. a) For a 0.748 mm diameter vessel embedded at depths 0.60 mm, 0.62 mm, 0.83 mm, 1.01 mm, and 1.55 mm from, and b) for a vessel of 0.644 mm thickness located at depths of 0.60 mm, 0.62 mm, 0.83 mm, 1.01 mm, and 1.55 mm.

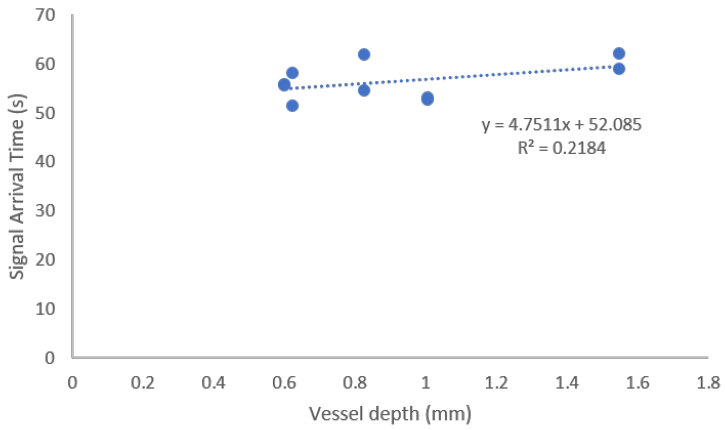


Figure 3.17: The signal arrival time versus depth from the *ex vivo* studies for 0.784 mm and 0.644 mm diameter vessels.

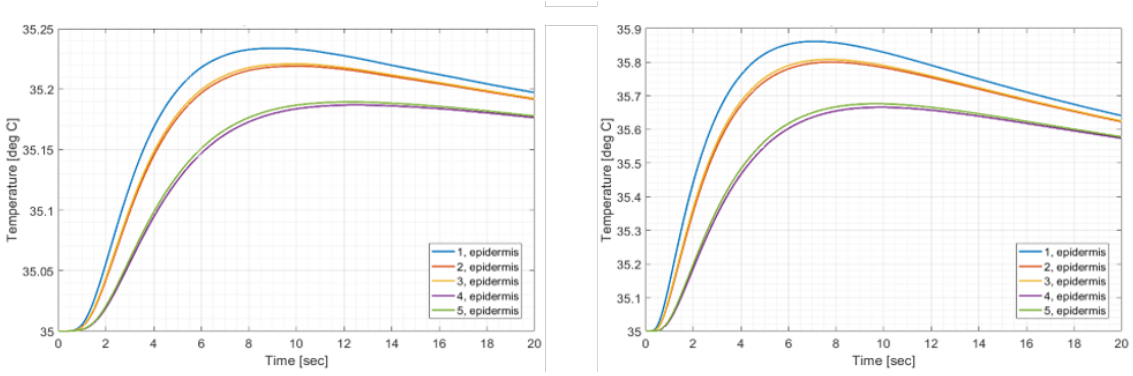


Figure 3.18: Temperature across the surface of the epidermis at points 1-5 shown in Figure 3.3. a) Temperature profiles for a 1 mm diameter vessel embedded 0.5 mm below the surface at an initial temperature of 39 °C, and b) temperature profiles for a 2 mm diameter vessel embedded 0.5 mm below the surface at an initial temperature of 39 °C.

### 3.3.3 Indirect Illumination Simulation

In indirect illumination mode, the region of interest is downstream from the region of illumination. ETI can be used to map vascular networks in indirect illumination mode. The temperature as a function of time was measured laterally across the surface of the tissue model at the five points shown in Figure 3.3 b and the results are shown in Figure 3.18. A sharp increase in temperature can be seen in the first several seconds of the simulation. The behavior of the temperature profiles shown in Figure 3.18 are similar for both vessel diameters modeled (1 mm and 2 mm). However, the larger diameter vessel causes the epidermis to reach a higher temperature. The behaviors shown in Figure 3.18 are the same regardless of the initial temperature of the embedded vessel, however the maximum temperature of the epidermis increases as the initial temperature of the embedded vessel increases. Also, as expected, the highest temperature is recorded at location 1 (just above the embedded vessel) and locations 2 and 3 have slightly lower temperatures. Locations 4 and 5 have even lower temperatures because they are even farther from the vessel center.

The depth of the embedded vessel affects the maximum temperature and the rate of change of the temperature at the surface of the epidermis. Figure 3.19 shows the

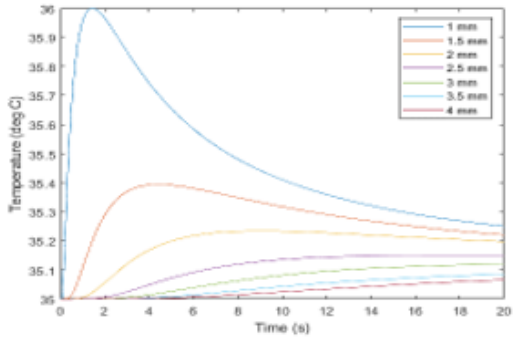


Figure 3.19: Temperature as a function of time for temperature sensor 1 shown in Figure 3.3 at different depths for a 1 mm diameter blood vessel. The vessel was at an initial temperature of 39 °C.

temperature change as a function of time for temperature sensor 1 (directly above the embedded vessel, see Figure 3.3) for a 1 mm vessel. As the depth of the vessel increases the maximum temperature of the epidermis decreases, and the increase seen at the beginning of the simulation is not as steep for more deeply embedded vessels. This same behavior was also seen for the 2 mm vessel. To investigate this trend more carefully, the derivative ($dT/dt$) of Figure 3.19 is shown in Figure 3.20. The time at which the maximum rate of temperature change at the surface is reached increases as the depth of the vessel increases (see Figure 3.20). The time at which the maximum occurs for each depth is well separated from the other depths. The same behavior was seen for a 2 mm vessel. This time of maximum temperature change will be called the signal arrival time. Figure 3.21 shows the depth of each vessel against the signal arrival time for both diameter vessels and all initial temperatures. This data has been approximated with both a linear and quadratic fit. The two fits provide a model to calculate the depth of an embedded vessel based on when the epidermis undergoes its maximum temperature change.

### 3.3.4 Indirect Illumination *Ex Vivo* Experiments

Figure 3.22a shows the unfiltered image of a porcine heart during indirect illumination ETI for one of the vessels imaged. Five lines are marked along the length of

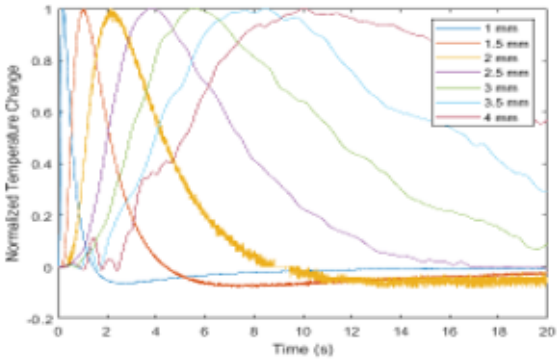


Figure 3.20: Rate of temperature change over time of sensor 1 shown in figure 3.19 at different depths for a 1 mm diameter blood vessel. All plots are normalized to their respective maximums. The vessel was at an initial temperature of 39 °C.

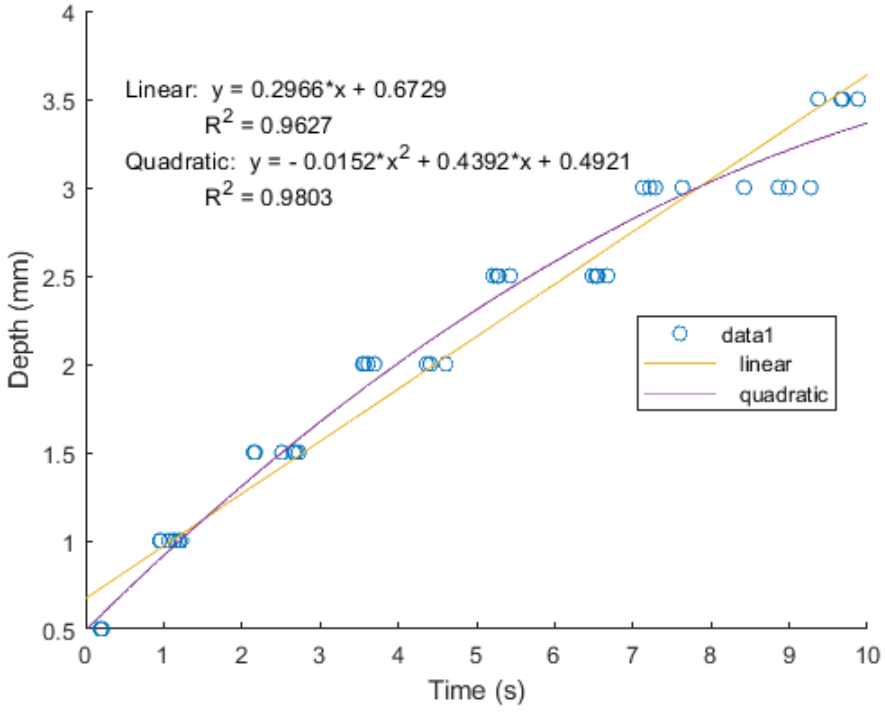


Figure 3.21: Linear and quadratic fits for the depth of an embedded vessel as a function of the arrival time of max temperature change at the surface of the tissue cuboid.

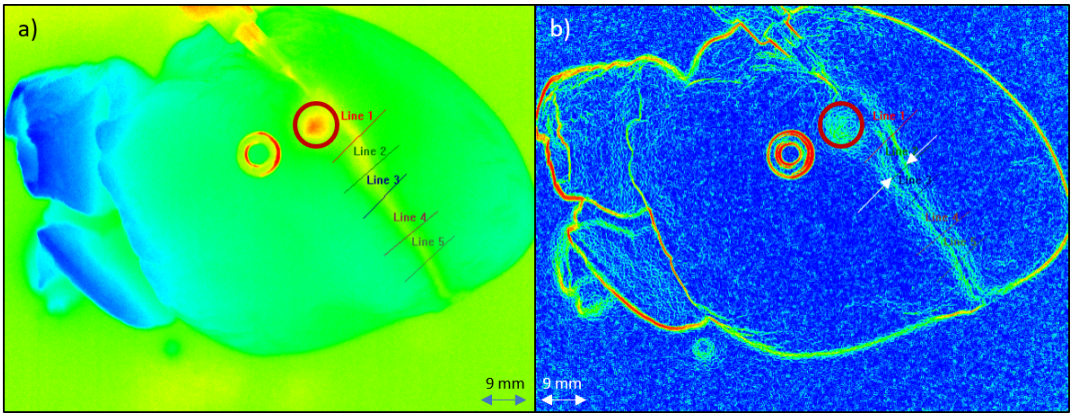


Figure 3.22: A frame from the video of porcine blood flowing through a vessel in a porcine heart using ETI in indirect illumination mode (Vessel 2 is shown here). a) The unfiltered image. Lines 1-5 mark the points at which the vessel was dissected and measured after imaging, and b) shows the same frame but with the spatial filter applied to map out temperature gradients. The spot of illumination is circled in red.

the vessel seen in the image. Physical width and depth measurements of the vessel were made at these locations. The separation between each line is approximately 1 cm. Similar measurements were taken for the other two vessels imaged. Figure 3.22b shows the same image with the spatial filter applied. The added filter clearly outlines the vessel edges.

Figure 3.23a shows the change in the maximum temperature as a function of time at position Line 1 for all three vessels imaged. Line 1 was the position at which the physical size and depth of the vessel was measured during dissection and is the position closest to the LED illumination spot (see Figure 3.22a for an example showing the position of Line 1). In all cases, the temperature change was measured relative to the tissue temperature before LED illumination began at the upstream position. The depths of the three vessels are shown in Table 3.2. These plots should be similar to Figure 3.19 for the simulations. In the simulations there were distinct differences in the heating as a function of depth. These same trends are not evident in the *ex vivo* data. This is likely the result of the fact that blood was flowing in the experiments, but stationary in the modeling. Pennes heating equation for biological tissue shows

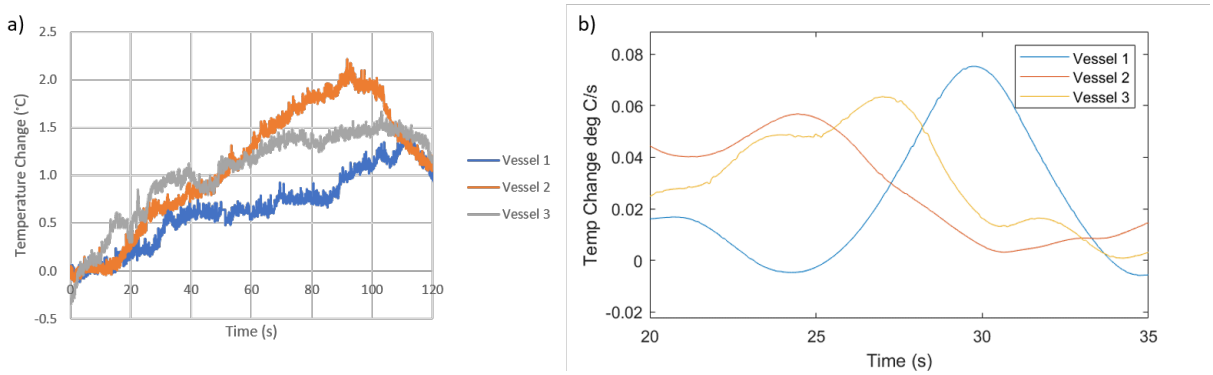


Figure 3.23: a) Temperature versus time plots of three embedded vessels within porcine heart tissue. The depths of these vessels are shown in Table 3.2. b) Derivatives of the temperature versus time plots taken between 20 and 35 s.

a linear dependence on blood perfusion rate.[12] Further, porcine blood was injected into the vessels using a hypodermic needle and it was difficult to maintain a steady flow rate during experiments. A better approach for comparison to the simulations may have been to image trapped (i.e. stationary) warmed blood in the vessels. This proved to be difficult to execute in practice.

Figure 3.23b shows the derivative of the temperature as a function of time between 20 and 35 seconds (where differences in the heating rates were evident) for the three vessels. This should show behavior similar to that seen in Figure 3.20b for the simulations. However, the same dependence on vessel depth is not clearly seen for the *ex vivo* experiments. Again, this is likely the result of flowing blood and inconsistencies in the flow rate. A perfused simulation and a tissue model with a controlled flow rate are needed to further explore the use of signal arrival time to estimate vessel depth in practice.

Figure 3.24 shows temperature versus time for all five positions (Lines 1-5) for vessel 2. Notice that the curves look almost identical. Heating as a function of time is independent of the distance from the point of illumination over the small distances used in this study. This behavior was seen for all 3 vessels. This suggest that there is some flexibility in choosing the point of illumination and the area of interest when

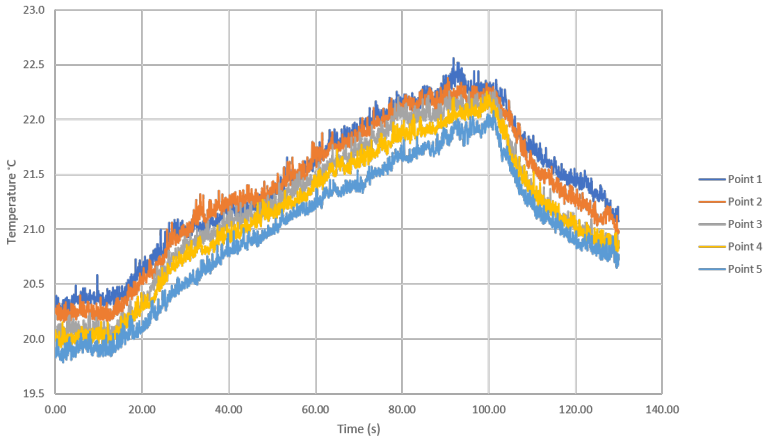


Figure 3.24: Temperature versus time plots for all five points shown in Figure 3.22a.

using ETI in indirect illumination mode. Figure 3.23 also shows the same cresting wave like shape of temperature change that was seen in Figures 3.6 and 3.14. However, this shape is not seen for all vessels. This again is likely due to inconsistent blood flow rates.

Figure 3.22b shows the spatially filtered image. The added filter clearly outlines the morphology of the vessel and the approximate positions of the vessel walls compared to the unfiltered image. Figure 3.25 shows line plots for Lines 1-5 from Figure 3.22. These are graphs showing temperature as a function of position acorss the vessel at these five positions. In all 5 plots, two large local maxima separated by a large dip are evident. The two arrows indicate these maxima in Figure 3.25a. The temperature minimum between the maxima corresponds to the approximate center of the vessel. The width of the vessel was measured based on the separation of the two peaks. Table 3.3 shows the widths based on caliper/ruler measurements during dissection and the widths determine from the spatially filtered images based on the distance between the peaks. Vessel 1 had the largest width and was the most accurately measured of the three, while vessel 3 had the smallest width out of the three vessels and was the least accurately measured.

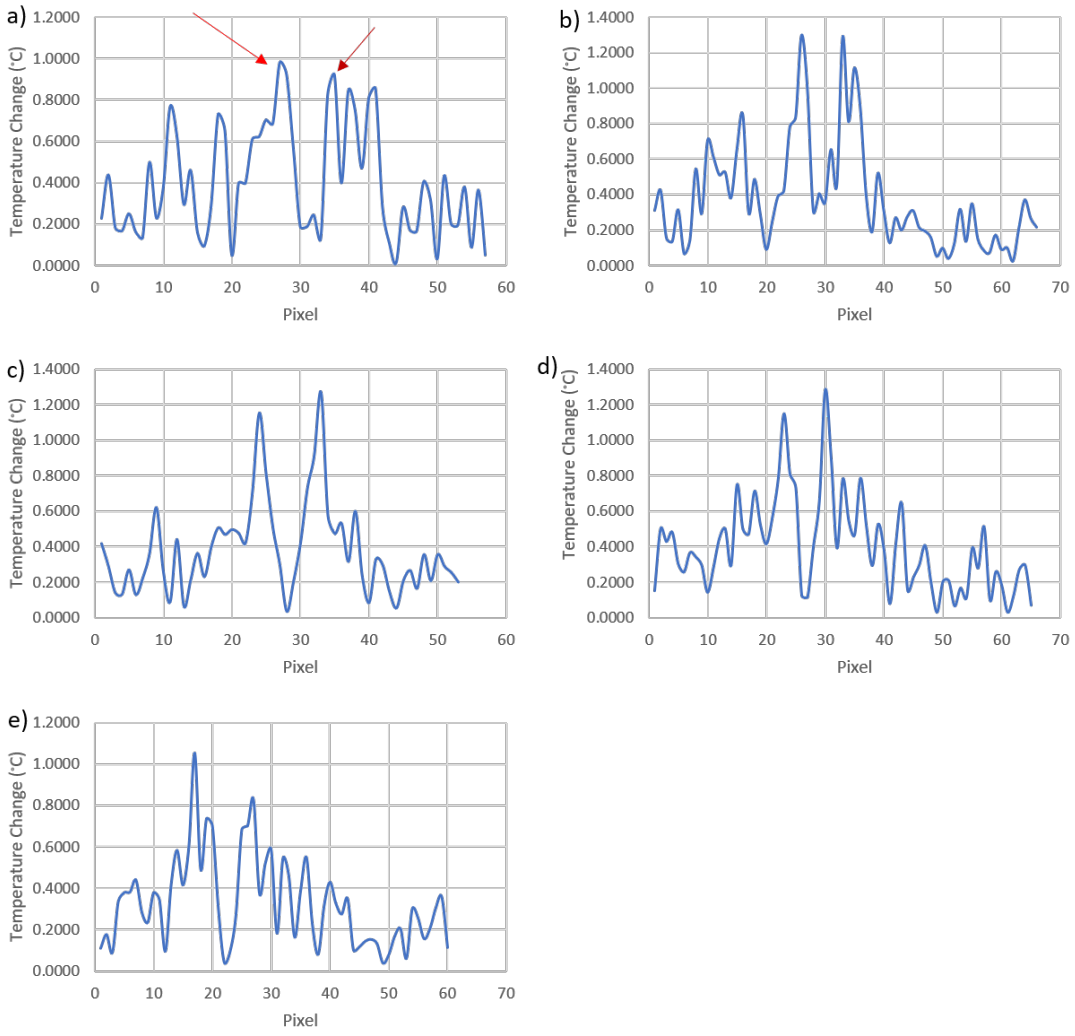


Figure 3.25: Temperature line plots of the 5 lines 1-5 shown in Figure 3.22 where (a)-(e) represent lines 1-5, respectively.

Table 3.3: Widths of vessels 1, 2, and 3 measured using ruler/digital calipers during dissection and with temperature gradient filter.

| Measured Widths (mm) | Vessel 1 | | Vessel 2 | | Vessel 3 | |
|---|---|---|---|---|---|---|
| | Physical | Filtered Image | Physical | Filtered Image | Physical | Filtered Image |
| **1** | 2.24 | 1.83 | 1.03 | 1.2 | 0.87 | 1.2 |
| **2** | 1.90 | 2.29 | 0.96 | 1.35 | 0.74 | 0.94 |
| **3** | 1.48 | 1.51 | 0.95 | 1.57 | 0.70 | 0.93 |
| **4** | 1.54 | 1.24 | 0.75 | 1.18 | 0.41 | 1.13 |
| **5** | 1.05 | 1.02 | n/a | 0.99 | n/a | 1.28 |
| **Average** | 1.64 ± 0.45 | 1.58 ± 0.50 | 0.92 ± 0.12 | 1.26 ± 0.21 | 0.68 ± 0.19 | 1.10 ± 0.16 |

## 3.4 Discussion

Enhanced thermal imaging (ETI) is novel combination of standard thermal imaging and selective heating of embedded blood vessels. This combination shows potential in overcoming previous short comings of biomedical applications of standard thermal imaging highlighted previously by Han et al (i.e contrast between tissue types because temperature differences are small, and limited spacial resolution because of limited pixel densities in micro-bolometer arrays.) Both computational simulations and physical tissue experiments designed to determine limitations of the ETI process and to begin to develop methods for accurate estimation of embedded vessel depth and width have been presented here.

Enhanced thermal Imaging can be used in two different modalities - direct and indirect illumination. Direct illumination images within the spot of illumination. Computational simulations of direct illumination showed a limitation to the depth an embedded vessel can be accurately detected of approximately 2.0 mm regardless of vessel size. An independence between the depth of an embedded vessel and the maximum temperature at the tissue surface was also shown computationally. *Ex-vivo* tissue experiments showed a weak negative correlation between maximum temperature change at the surface of the tissue and the vessel depth. Computational simulations showed the potential to use the contrast between temperature artifacts and surrounding tissue temperature to delineate vessel depth via signal arrival time. A dependence between the signal arrival time was shown computationally, but further exploration during *ex vivo* did not show this same dependence. However, the imaging system used during the tissue experiments has a lower spatial and thermal resolution compared to the simulations. Future work will use a relay lens to achieve a higher spatial resolution to overcome this limitation. Limitations within the computational model restricted energy flow at the boundaries of the tissue cube, cooling via convection, and the flow of blood. Future work will involve the addition of these parameters

(i.e heat loss at boundaries, convective cooling of air at the surface, and blood flow modeling) to create a more robust model to predict the effects of ETI.

Indirect illumination ETI was also modeled. In this mode, the imaging area is located downstream from the point of illumination. Computational simulations showed a dependence between the depth of an embedded vessel and the time of maximum temperature change at the surface. Tissue experiments using porcine hearts showed this dependence but the trend was not as clear due to inconsistencies of blood perfusion rate between trials. Future work will overcome this issue using an animal or human model. Tissue experiments also showed an independence on the separation between the imaging area and the point of illumination. This demonstrates some flexibility for clinicians to select these regions during surgery.

The introduction of intraoperative imaging techniques has shown beneficial impacts for patient outcomes and a reduction in costs for patients.[22] ETI has the potential to be used both intraoperatively and post-surgically, while overcoming the necessity of intravenous contrast agents. The limitations and potential of ETI has been shown both computationally and experimentally with tissue models. The need for a perfused model either human or animal has also been detailed. Future work using these models will highlight the potential beneficial impact ETI can have as an intraoperative or post-surgery imaging tool.

# CHAPTER 4: POST-OPERATIVE MONITORING OF TISSUE PERFUSION IN SKIN FLAPS IN A MURINE MODEL USING ENHANCED THERMAL IMAGING

## 4.1 Introduction

Inadequate tissue perfusion is a fundamental cause of early complications following a range of procedures including the creation of skin flaps/grafts during reconstructive microsurgery and complex closures during amputation. Historically, clinical judgment has been used as the primary means of evaluating tissue perfusion intra-operatively via palpation of pulses, assessment of bleeding at cut edges, and observation of tissue color. However, these methods are not always reliable. In many cases, a more conclusive evaluation of tissue perfusion is desired intra-operatively to avoid complications secondary to tissue ischemia.[20–23] Duggal et al. showed that the introduction of an intra-operative optical guidance tool, such as indocyanine green angiography (ICGA), reduced the incidence of surgical site necrosis.[22] ICGA involves the intravenous injection of indocyanine green (ICG), a fluorescent dye that binds to blood. ICG fluoresces when illuminated with near infrared light ($\lambda = 745$ nm) and an image is captured at the emission peak of the dye ($\lambda = 840$ nm). ICGA can provide accurate real-time mapping of micro-vasculature during plastic and reconstructive surgery.[20–24,27,39] Unfortunately, the introduction of ICG dye can lead to complications in patients with shellfish allergy or poor renal function. The use of a fluorescent contrast agent also adds limitations during surgery necessitating extended pre-operative planning. In addition, clinically relevant ICGA requires both optimal ICG dose administration and angiography time that can be challenging to achieve in some clinical surgical environments. While the introduction of this type of imaging assessment has shown positive

effects on the prevention of surgical site necrosis, a cheaper more versatile tool that could provide both intraoperative guidance and post-surgical monitoring of healing is needed.

Thermal imaging has been used for surgical guidance, but is consistently outperformed by ICGA.[30,31,33,36] The use of mid-infrared imaging for surgical guidance is limited by the thermal resolution of the camera because temperature differences between tissue types is small. The thermal resolution of mid-IR imaging requires significant improvement to become a viable replacement for ICGA. Enhanced Thermal Imaging (ETI) provides this improvement to mid-infrared imaging, while overcoming the shortcomings of ICGA. ETI uses illumination with low powered LEDs ($\lambda$ = 530 nm) to selectively heat blood rich regions.[1–3,18,38] Blood absorbs strongly at this wavelength allowing the selective increase in its temperature relative to the surrounding tissue. A mid-infrared camera (sensitive from 7 - 10 $\mu$m) is then able to capture the small increase in temperature in the targeted region. Previous studies showcased the ability of ETI to map vascular networks but with a necessity for lengthy post-processing.[1–3] Recent improvements have shown the real-time capability of ETI to map these same regions.[38] Computational filters, previously applied during post-processing, now are applied during the ETI process allowing for faster and more accurate delineation of vascular structures. ETI enables mid-IR imaging to target a specific tissue type (blood and blood vessels) in real time.

Two active computational filters - temporal and the spatial - can be used with ETI. Both active filters create 2-dimensional maps. The temporal filter averages all of the frames acquired by the mid-infrared camera before the illumination by LEDs begins. This creates an average steady state frame for the region of interest. This average steady state frame is then subtracted from each subsequent frame revealing only the pixels that have a temperature change over time. This allows for fast and accurate mapping of vascular structures. The spatial filter works by applying

a 2-dimensional weighted gradient, using the Prewitt derivative, across each frame acquired by the mid-infrared camera.[37] This shows the weighted temperature difference between neighboring pixels. The resulting image is then a 2-dimensional map showing the difference for each pixel from the neighboring 9 pixels.

Angiogenesis and vasculogenesis describe the growth and decay of blood vessels during the healing and re-perfusion of wounds for post-surgical sites such as skin grafts/flaps. The growth and decay of vessels during the healing of skin grafts in a murine model have been studied in detail by Lindenblatt et al. and O' Ceallaigh et al.[40,41] Both studies monitored the reperfusion of grafts using fluorescent labeling techniques similar to ICGA. During the healing process, the number of vessels and, thereby the amount of blood present in the wound area, increased rapidly post-surgery before decreasing again during continued healing. This matches the trends shown by Lindenblatt et al. and O' Ceallaigh et al, who show that there is an increase in the ratio of filled vessels and total vessels in the first 48-60 hours, and 5-6 days post surgery and a decrease in this ratio on day 14. Although in both of these studies they looked at reattached skin grafts, while we monitored skin flaps. ETI has the potential to monitor the reperfusion of tissue graft/flap sights because of this fluctuation in the amount of blood in the region. This change in the amount of blood present in the tissue should be observed as a temperature change during selective heating and imaging. Here we present a preliminary study to explore the potential use of ETI to monitor the re-perfusion and healing of skin flaps using a murine model.

## 4.2 Methods

### 4.2.1 Murine Model

Fifteen SKH1-Elite male mice age 5 to 6 weeks (23 - 28 g) were purchased from Charles River Laboratories and acclimatized to the vivarium at UNC Charlotte prior to use. All experiments were approved by the Institutional Animal Care and Use Committee at UNC Charlotte and supervised by the staff veterinarian. On day 0 of

the study, surgery was performed to create skin flaps roughly 7 mm x 7 mm incised on the left and right sides of the back, at approximately shoulder level. For the right flap, 3 incisions were made to outline the 7 mm x 7 mm area and sutures were placed at the corners (referred to as the incised-only flap in this study). For the left flap, incisions were made along 3 edges of the flap and then the flap was lifted, the flaps were undermined (all blood vessels and tissues were severed) and then the flap was placed back down and sutured at the corners (referred to as the undermined flap in this study). The skin flaps were visually inspected every day of the 12-day study. Skin flaps were imaged using ETI and/or IVIS imaging throughout the 12-day study (see Table 4.1 for details). The animals were separated into two groups, A and B, and these groups were imaged on alternating days to limit the number of times that individual animals were anesthetized. Animals were anesthetized for surgery and during each imaging session so that they remained stationary. After imaging on day 5 post surgery the sutures were removed from all animals. At day 12 post surgery, the animals were euthanized and the skin flaps were excised.

### 4.2.2 Fluorescent Imaging

Fluorescent imaging was performed using an IVIS Spectrum *in vivo* imaging system (PerkinElmer Inc). Sedated mice were illuminated and imaged from above (epi-illumination, see Figure 4.1). The fluorescent response was recorded using a 2048 X 2048 pixel, cooled (-90°C) CCD detector (dark current $< 100$ electron/s/cm$^2$ and RN $< 5$ electrons for 8-pixel binning). A 25 cm x 25 cm FOV was used for all imaging sessions, resulting in a spatial resolution of 20 $\mu$m/pixel. IVIS imaging was performed using a series of narrow-band filters to isolate the fluorescent signal from blood and the fluorescent dye ICG, while allowing removal of the fluorescence background. This spectral fluorescence background removal was performed using Living Image software™. In seven mice, ICG was administered intravenously at a dosage of 25 mg/mL through the tail vein at the start of three different imaging

Table 4.1: Table showing the imaging performed on each day of the study. Day 0 was the day of surgery. The imaging modalities include white light imaging (WL), enhanced thermal imaging (ETI), IVIS fluorescent imaging targeting blood fluorescence (IVIS-B), IVIS fluorescent imaging targeting ICG dye administered intravenously (IVIS-IV), and IVIS fluorescent imaging targeting ICG dye administered sub-cutaneously (IVIS-SubQ).

| | | Day of Study | | | | | | | | | | | | |
|---|---|---|---|---|---|---|---|---|---|---|---|---|---|---|
| | Method | 0 | 1 | 2 | 3 | 4 | 5 | 6 | 7 | 8 | 9 | 10 | 11 | 12 |
| Group A | White Light | X | X | | X | | X | | X | | X | | X | X |
| | ETI | X | X | | X | | X | | X | | X | | X | X |
| | IVIS-B | X | X | | X | | X | | X | | | | | X |
| | IVIS-IV | X | X | | X | | X | | X | | | | | X |
| | IVIS-SubQ | | | | | | | | | | | | | |
| Group B | White Light | X | X | | X | | X | | X | | X | | X | X |
| | ETI | X | X | | X | | X | | X | | X | | X | X |
| | IVIS-B | X | X | | X | | X | | X | | | | | X |
| | IVIS-IV | | | | | | | | | | | | | |
| | IVIS-SubQ | X | X | | X | | X | | X | | | | | X |

sessions. ICG was administered to the other 8 mice subcutaneously at the site of the flap on the day of surgery. No further ICG was administered to these mice during the study. ICG imaging was obtained using an excitation wavelength of $\lambda = 745$ nm and emission wavelength $\lambda = 840$ nm. Blood fluorescent imaging was obtained for each animal using an excitation wavelength of $\lambda = 500$ nm and emission wavelength of $\lambda = 620$ nm. In addition to the fluorescent emission images, low-light level white light images of the mice were obtained. The fluorescent images were overlaid with the white light images to correlate the position of the skin flap (seen by visual inspection) and the fluorescent emission. Table 4.1 lists the type of imaging performed on each group, on each day of the study. Subjects were imaged one at a time, immediately after ETI was completed.

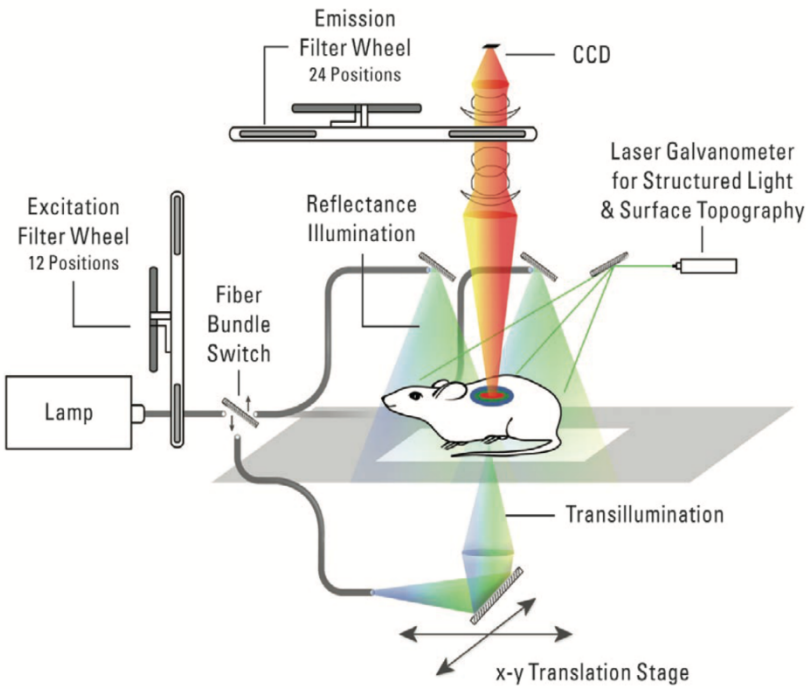


Figure 4.1: Fluorescence image capture process of the IVIS Spectrum *in vivo* imaging system.[42]

### 4.2.3 Enhanced Thermal Imaging

Figure 4.2 shows a schematic of the experimental setup. A FLIR SC600 series mid-IR camera (sensitive from 7.5 to 14 $\mu$ m) with an array size of 640 x 480 pixels and maximum frame rate of 200 fps was used to image all mice. A compound germanium lens with an effective focal length of 100 mm was used in tandem with the camera yielding a spatial resolution of 0.10 mm/pixel and a working distance of 5 cm. Two LED sources with a peak wavelength of 530 nm (Thorlabs M530L2) were used to illuminate the mice during imaging. Both sources were collimated using aspheric optics, and the LED source was controlled using a high-power LED driver (Thorlabs DC2100). The illumination had a 1 cm diameter spot size yielding an average power density of 13.6 mW/cm$^2$.

Imaging was obtained the day before surgery, the day of surgery (day 0), and on subsequent days until the end of the study (day 12). Table 4.1 lists the type of imaging

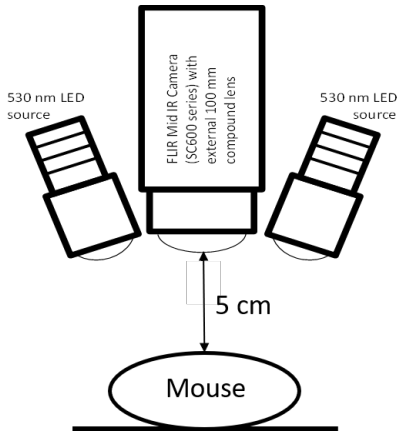


Figure 4.2: Enhanced thermal imaging (ETI) setup. The thermal camera was used to image the mouse from above. The two 530 nm LEDs were used to illuminate the mice inducing a contrast in the blood rich regions of the flaps while the thermal camera measured these temperature gradients.

performed on each animal, on each day of the study. For each imaging session, a 2-minute video was recorded. The videos had an average frame rate of 6 fps. During each imaging session, the skin flap and surrounding tissue was illuminated with the LED sources for 80 s. The thermal camera recorded the temperature of the skin flap and surrounding tissue for 10 s before LED illumination, during illumination, and for 30 s after illumination. After imaging temporal and spatial derivative filters were applied to the videos.

### 4.2.4 Image Filters Applied in Post-processing to ETI Videos

For each ETI imaging session a temperature contrast between the blood vascular network and surrounding tissue was created. Both a temporal and spatial derivative analysis was performed in MATLAB to highlight this temperature contrast. This analysis was performed after the imaging session (but could be done in real time as performed in earlier work).[38] The temporal derivative filter averaged the frames acquired before the beginning of illumination to create a baseline image. The baseline image was then subtracted from each subsequent frame of the video so that the output frame shows the temperature difference between the two. This resulted in

a 2D map highlighting pixels in which rapid temperature change occurred. The spatial derivative filter used the Prewitt method defined in MATLAB. The Prewitt gradient operator uses a weighted sum of the 3 x 3 pixel neighborhood surrounding the pixel of interest.[37] This filter emphasizes differences that occur at temperature boundaries. Each pixel then represents the weighted temperature difference between it and the surrounding pixels, producing a 2D map highlighting pixels that exhibit a temperature difference with neighboring pixels. These spatial filtering processes was applied to each frame of the video.

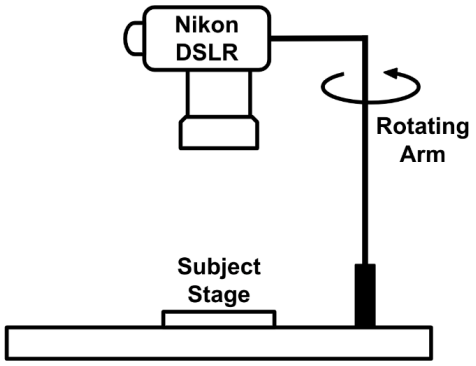


Figure 4.3: White light imaging setup.

### 4.2.5 White Light Imaging

Standard white light images were taken of the flaps to keep track of visible wound healing over the course of the study. A Nikon DSLR camera was mounted on a swinging arm attached to the ETI setup to allow it to be moved out of the field of view of the infrared camera once the pictures were acquired (see Figure 4.3). The lens was oriented parallel to the stage 12 cm directly above the mice, yielding a spatial resolution matching that of the ETI setup. On all 12 days, one picture of each flap was taken, totaling two images per mouse per day. Any wound irritation or injury was captured in these photographs.

## 4.3 Results

### 4.3.1 Enhanced Thermal Imaging

For all mice, the LED illumination heated the blood/vascular networks in and around the skin flap by an average of 0.62 ± 0.18 °C. This increase in temperature from LED illumination was sufficient to highlight vessel-rich areas, but was well below the tissue/blood temperature damage threshold.

#### 4.3.1.1 Thermal, ETI, and White Light Imaging

Figure 4.4 shows the white light, unfiltered ETI, spatially filtered ETI, and temporally filtered ETI images of the incised-only flap for Mouse 1. These are similar to images acquired for all mice. The thermal images were taken from frames in the video 20 s after the LED illumination period ended. The white light images taken on the day of surgery, day 0, show the initial incisions and the location of the sutures (small blue knots). The other images show progressive healing and a decrease in inflammation from day 0 to 12. On day 12 of the study, little or no scaring/damage is evident in the white light images. The unfiltered ETI images show that regions near the edges of the flap were at a lower temperature than the surrounding tissue during the first few days after surgery. On day 0, the incisions are clearly visible in these images. The cooler regions decrease in size as the flap heals until day 7, when the unfiltered ETI image shows no difference in temperature associated with the flap and surrounding tissue. The spatial filter shows the same information as the unfiltered ETI image by highlighting the regions of different temperature. The spatial filter shows that on the day of surgery the incised edges have a different temperature than the rest of the flap area, which decreases in size until day 7 when the edges are no longer apparent. Days 9-12 show no delineation of the flap in the spatially filtered images. The white light, unfiltered ETI, and spatially filtered images seen in Figure 4.4 suggest that the incisions are healed by day 7.

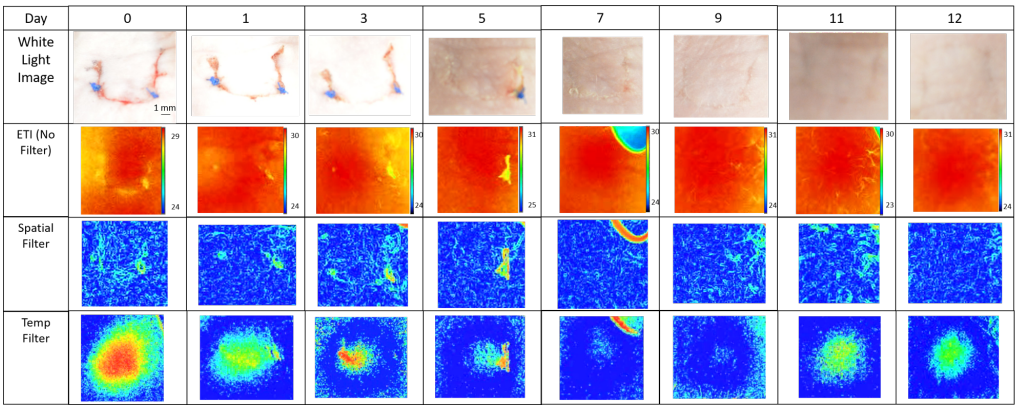


Figure 4.4: White light, ETI (no filter), spatially filtered ETI, and temporally filtered ETI images taken after 20 s of illumination for the incised only flaps of Mouse 1.

The temporally filtered images are shown in Figure 4.4. These images highlight the location of maximum heating. The location of this area of maximum heating shifts over the course of the 12-day study. On day 0, the lower edge and the middle of the flap exhibit the largest temperature change. On day 1 this difference migrates to the bottom edge of the flap and then to the lower left and right corners on days 3 and 5. There is no clear region of maximum temperature change on days 7 and 9. The temporally filtered images on days 11 and 12 show an almost uniform region of temperature change roughly the size of the illumination spot. The flap is not visible in these images.

Figure 4.5 shows the white light, unfiltered ETI, spatially filtered ETI, and temporally filtered ETI images of the undermined flap from Mouse 1. These are similar to the images seen for the other mice. The thermal images were taken from frames in the video 20 s after the LED illumination period ended (as was the case for Figure 4.4). The white light images in Figure 4.5 show progressive healing of the flap between days 0 and 12, with complete healing by day 9. This flap heals more slowly than the incised-only flap shown in Figure 4.4. Some residual scaring is evident for this flap on day 12. The unfiltered ETI images depict regions of different temperatures associated primarily with the edges of the flap. By day 7, the temperature across the

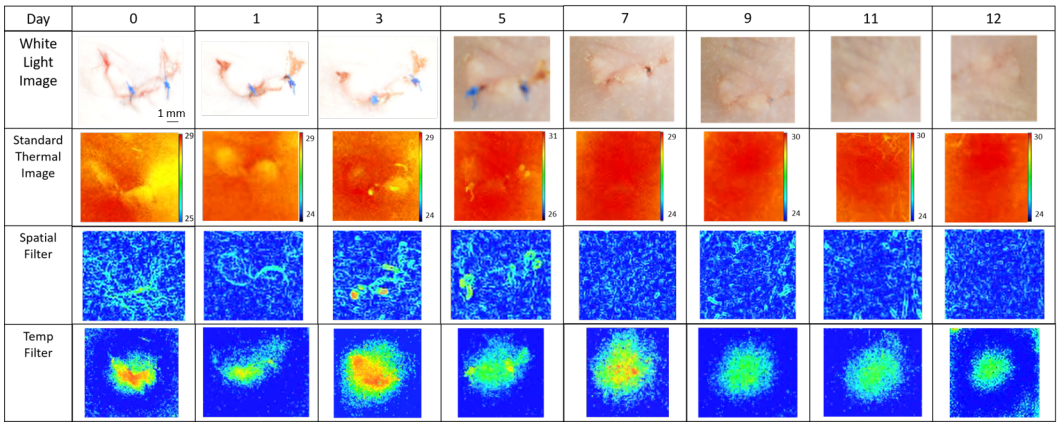


Figure 4.5: White light, ETI (no filter), spatially filtered ETI, and temporally filtered ETI images taken after 20 s of illumination of the incised and undermined grafts of Mouse 1.

entire region is uniform. The spatially filtered images also show similar results. The overall behavior is consistent with that seen for the incised-only flap.

The temporally filtered images again show a shift in position of the region of maximum temperature change over the first three days similar to Figure 4.4. On days 1-3 the position of maximum temperature starts in the lower left corner, transitions to the entire lower edge of the flap, and then begins to migrate to the middle of the flap by day 3. Days 5 and 7 show a persistent area of heating that is associated with the flap. For the flap that was incised-only (Figure 4.4), there is little heating evident on these days. The region of temperature change for the undermined flap then becomes more homogeneous on days 9-12 (Figure 4.5) and looks like the LED spot seen on the incised-only flap.

Figure 4.6 shows the white light images and Figures 4.7 and 4.8 shows ETI (no filter), spatially filtered, and temporally filtered images taken before illumination, at the start of illumination, and at the end of illumination of the incised only and undermined flaps of Mouse 3 on Day 1. Before illumination the spatially filtered images outline the damaged regions since these areas are at a different temperature than the rest of the tissue. After 20 s of illumination two of these regions disappear (indicated by the red arrows in the t = 0 s and 10 s images). A region of damaged

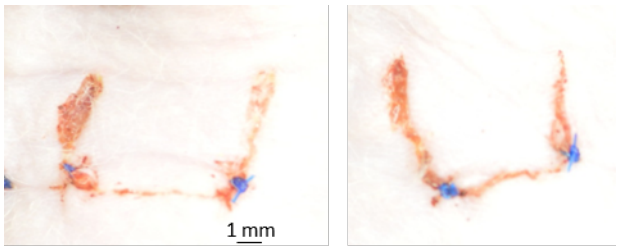


Figure 4.6: White light images of the incised only (left) and incised and undermined (right) flaps of Mouse 3 on the first day after surgery.

tissue is still present at t = 30 s indicated by the black arrow. The temporally filtered image at t = 30 s, in Figure 4.7, shows the majority of the heating occurs at the bottom edge of the flap with the highest temperature change seen at the bottom left corner of the flap. This behavior is not clearly visible in the unfiltered ETI images. The region of large temperature change seen in the temporally filtered image at t = 30 s indicates those regions have a large response to LED illumination likely due the presence of blood/microvasculature forming during the healing process. The region of damage indicated with the black arrow in the spatially filtered image at t = 30 s (see Figure 4.7, indicates a region with little blood/microvasculature. There is a corresponding lack of temperature change in this region in the temporally filtered image as expected. Comparing the t = 30 s temporally filtered images of Figures 4.7 and 4.8 shows that more of the flap is responding to the illumination for the undermined flap. This could potentially be a response from the deeper non-superficial damage. Again one of the points of maximum temperature change, colored red, in the t = 30 s temporally filtered image of Figure 4.8 corresponds to the damaged region that disappears in the corresponding spatially filtered image.

#### 4.3.1.2 Temperature as a Function of Time and Analysis of ETI images

Figure 4.9 shows the temperature as a function of time before, during, and after illumination with the LEDs. This is shown for Mouse 1 for both incised and undermined grafts (these are similar for the rest of the mice). The plots were created by averaging

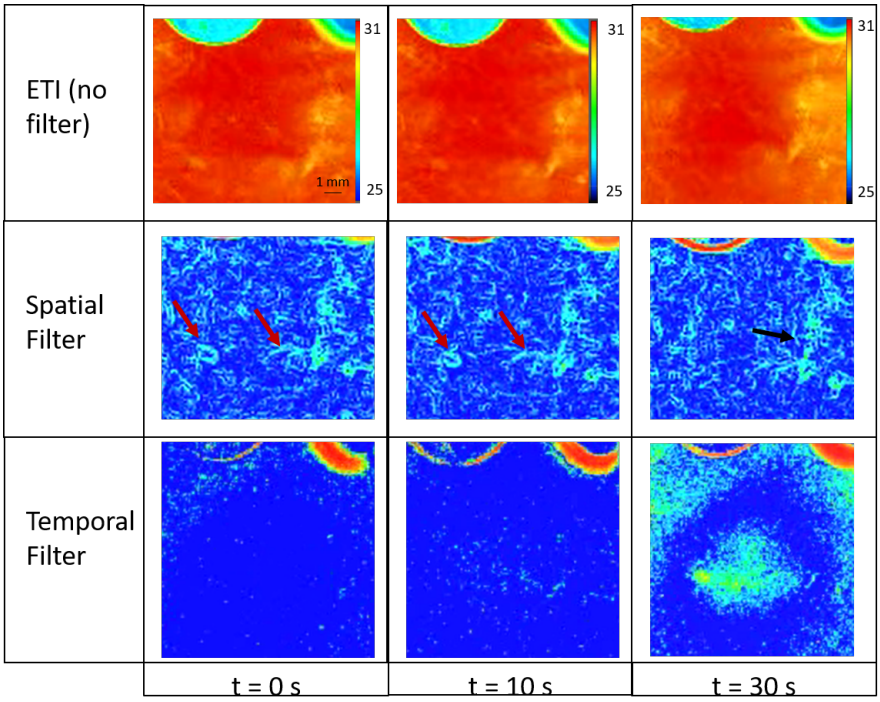


Figure 4.7: ETI (no filter), spatially filtered, and temporally filtered ETI images taken at t = 0 s (no LED illumination), t = 10 s (start of LED illumination), and t = 30 s (end of LED illumination) for the incised only flap of Mouse 3 on the first day after surgery.

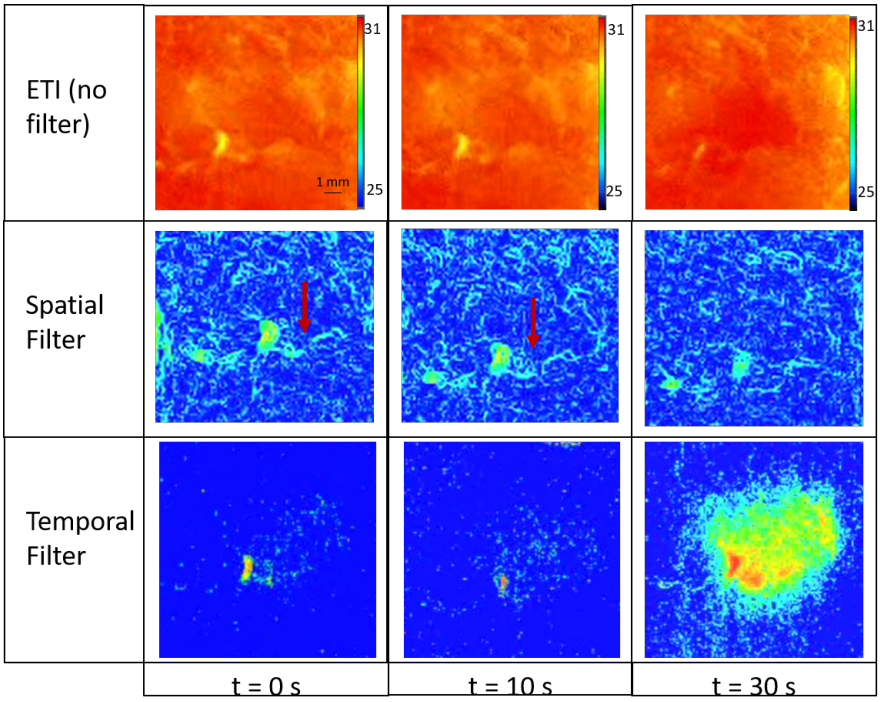


Figure 4.8: ETI (no filter), spatially filtered, and temporally filtered ETI images taken at t = 0 s (no LED illumination), t = 10 s (start of LED illumination), and t = 30 s (end of LED illumination) for the incised and undermined flap of Mouse 3 on the first day after surgery.

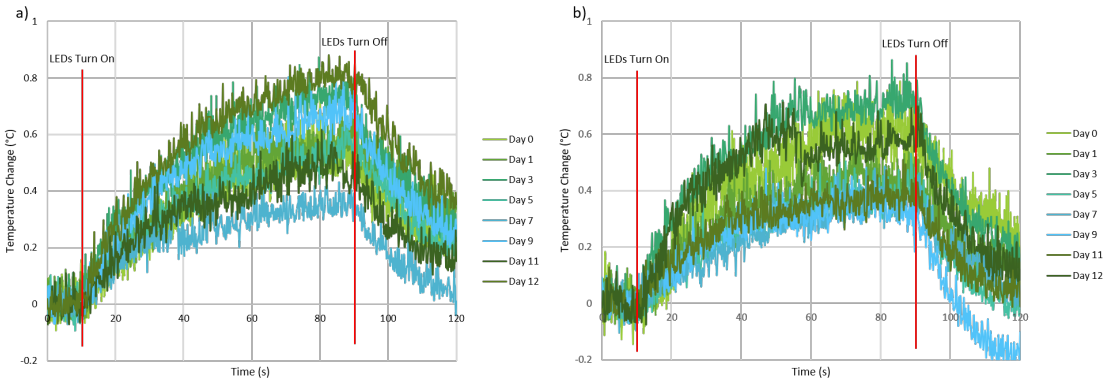


Figure 4.9: Temperature time graphs of all ETI measurements of both a) Incised, and b) Incised and undermined grafts of mouse 1.

the temperature of the flap site before illumination and subtracting that temperature from all subsequent frames of the video. Figure 4.9 shows the response of the flap site to LED illumination. When LED illumination begins, the temperature rises sharply and then plateaus toward the end of illumination. When the LED illumination stops, there is an exponential decay as the flap cools. This cresting wave shape of the temperature change seen in Figure 4.9 is expected and was seen previously in simulations of ETI conducted with MCMATLAB.[38] The maximum temperature change shown for both the incised-only and undermined flaps is the same so there is no dependence on overall temperature change between the different flap types.

The temporally filtered images showed that different regions of the skin flap responded to LED illumination from day to day (e.g. the location of the maximum temperature shifted; see Figures 4.4, 4.5, and 4.7). To quantify how much of the flap was responding to LED illumination on a given day, the number of pixels with a temperature difference greater than the average background noise of the temporal derivative filter after 20 s of illumination was determined. Figure 4.10 shows this pixel count and this is a measure of how much of the flap was responding to LED illumination. This is shown for both the incised only and undermined flaps on each day of the study. The error bars are the deviation from the mean value for the flaps.

For the incised only flaps, there is a sharp increase in the number of pixels responding to illumination between days 2 and 4. A similar response can be seen for the undermined flaps. This suggests that the amount of blood/microvasculature in the flap has increased on these days (likely the result of the healing process). Later in the study, between days 6 and 8, there is another increase in the number of pixels responding to illumination for the undermined flaps. This was seen in Figures 4.4, and 4.5 as persistent heating in the undermined flap. This second peak is not seen for the incised only flaps. The error bars shown in Figure 4.10 are large. This could be due to different healing rates for the individual mice. To further explore this, the mice were separated into two groups based on the date of surgery. Surgery was performed on two days. Mice 1-7 underwent surgery on the first day of surgery and Mice 8-15 underwent surgery on second day. Figure 4.11 shows the pixel counts for these two groups as a function of day of the study. The first sharp increase in the area of flap response to illumination occurs on different days for the two surgical groups. Mice 8-15 show this sharp increase in flap response a day earlier than mice 1-7 suggesting that mice 8-15 are healing at faster rate. This is likely the result of the veterinarian refining his surgical technique and inducing less trauma on the second day of surgeries. Figure 4.11 shows that regardless of when the first sharp increase in flap response occurs the second sharp increase for the undermined flap occurs approximately 5 days later. This suggests that healing occurs in stages, with the first stage occurring between days 2-4, and the second stage occurring between days 6-8. ETI plus the temporal filter seems to be sensitive to a stage of healing not seen by the other imaging techniques. Figures 4.10 and 4.11 omit Mouse number 2 because of extensive damage done to flap areas due to the animal scratching the surgical area.

Figure 4.12 a shows the normalized flap area response curves (from Figure 4.11) that have been shifted so that the first maximum occurs on the same day for both surgical groups. Regardless of when the first maximum of flap area response occurs

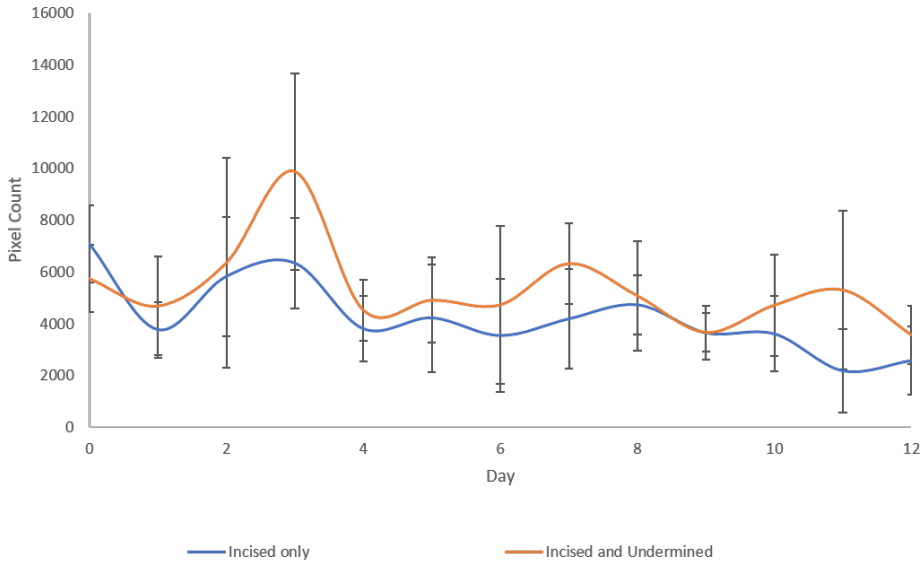


Figure 4.10: The average number of pixels with temperature change greater than the background noise of the temporal filter for both incised only, and undermined flaps for all mice for each day of the study.

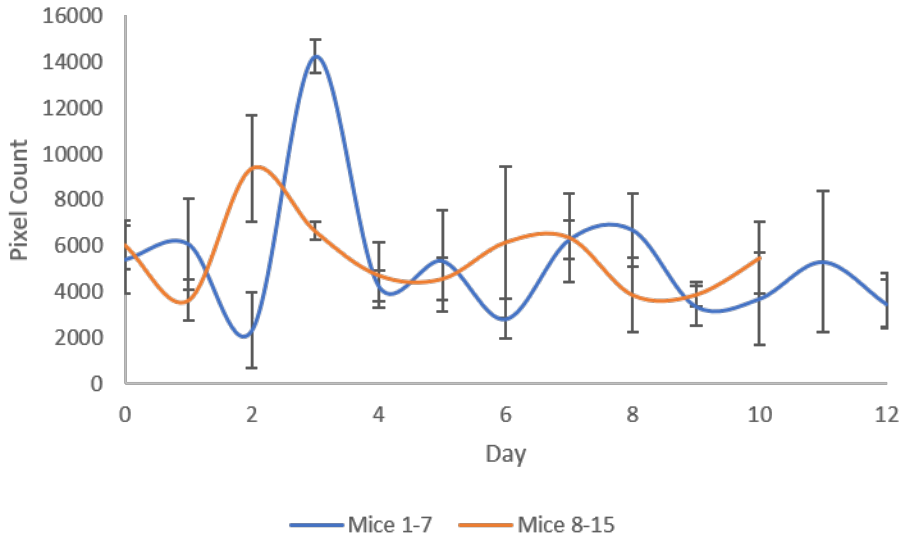


Figure 4.11: The average number of pixels with temperature change greater than the background noise of the temporal filter for the undermined flaps for the two surgical groups: mice 1-7 and mice 8-15.

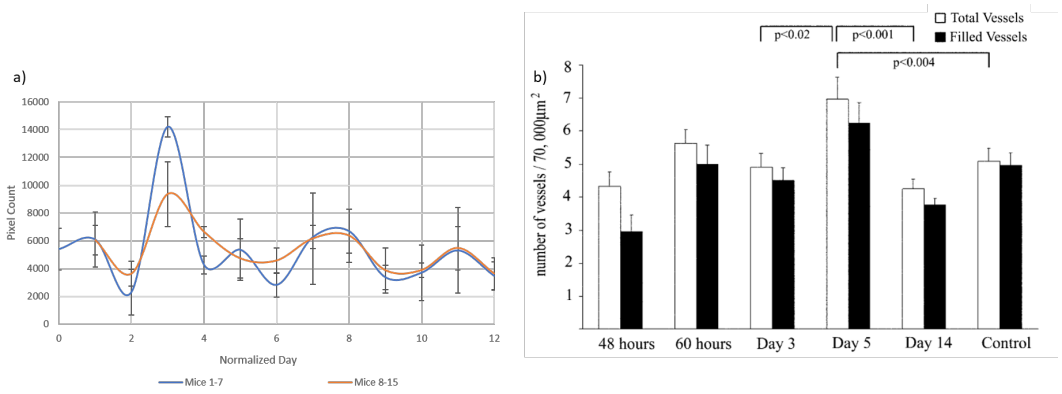


Figure 4.12: A comparison between the flap area response normalized to the first maximum for both surgical groups (a) and a previous study shown by O'Ceallaigh et al. measuring the total number of vessels and filled vessels each day post-operatively in mice.[41]

the second increase in flap area response occurs approximately 4-5 days later. Figure 4.12 b compares the ETI results to a previous study by O'Ceallaigh et al. in which the total number of unfilled and filled vessels was measured post-operatively in skin grafts in mice.[41] The ratio of the number of total versus filled vessels increases between the first 48 and 60 hours and then again on day 5. This agrees with the flap area response seen for the incised and undermined flaps shown in Figures 4.10, 4.11, and 4.12 a.

Mouse 2 caused damage to the surgical site due to scratching and was omitted from Figures 4.10 and 4.11. Figures 4.13 and 4.14 show white light, and ETI images of the incised only, and incised and undermined flaps of Mouse 2. On day 7 the white light images show damage that occurred across most of the undermined flap with some damage extending to the incised only flap. This damage prevented these flaps from healing at the same rate as the flaps on the other mice. This is seen in the temporally filtered images for both flaps. Figure 4.15 shows the pixel count, or flap response, for both flaps on Mouse 2 for each day of the study. Comparing Figures 4.10, 4.11, and 4.15 shows that the first sharp increase in flap response for Mouse 2 starts on day 2 and ends on day 6. For the other mice the sharp increase in flap response starts on day 2 and ends by day 4. This prolonged increase in response to the illumination is

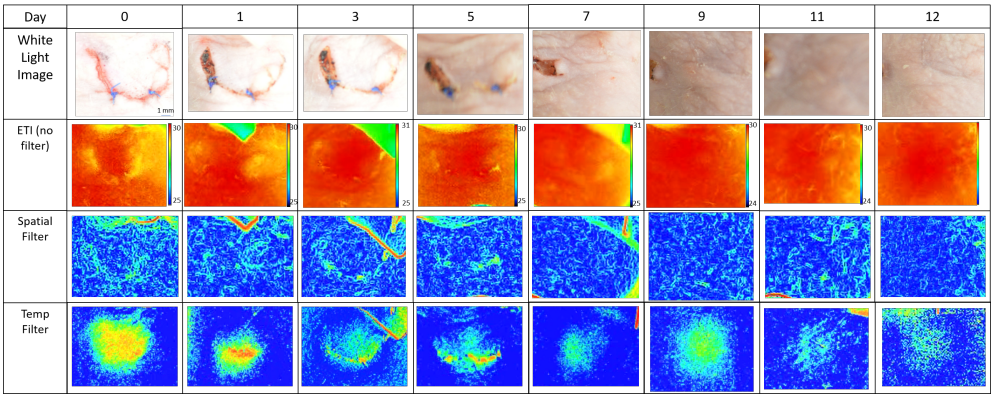


Figure 4.13: White light, ETI (no filter), spatially filtered ETI, and temporally filtered ETI images taken after 20 s of illumination for the incised only flaps of Mouse 2.

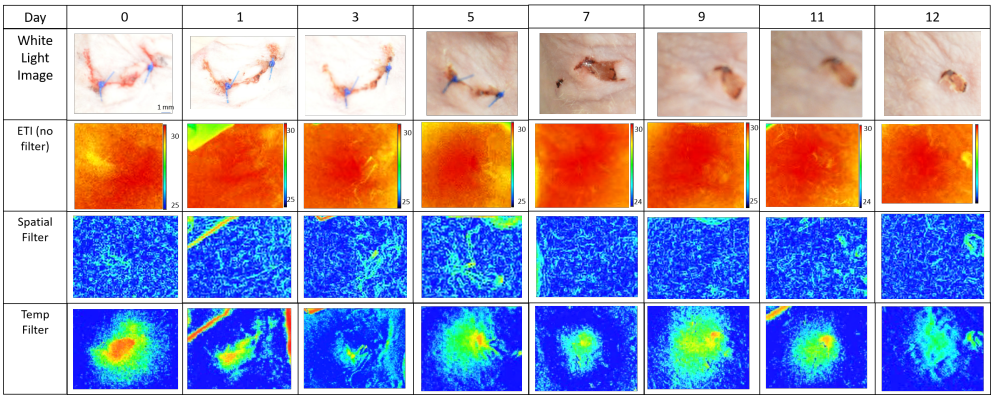


Figure 4.14: White light, ETI (no filter), spatially filtered ETI, and temporally filtered ETI images taken after 20 s of illumination for the incised and undermined flaps of Mouse 2.

most likely from prolonged healing of the flaps due to the animal scratching at the flap areas. Both flaps (incised only and undermined) show a second increase in flap response to illumination for Mouse 2. The second increase in flap response also has the same magnitude as the first response. This was not the case for the other animals. This second response also starts on day 6 and ends on day 10 which is prolonged in comparison to the other mice. The results for Mouse 2 clearly demonstrate that the repose to LED illumination seen in the temporally filtered images is related to healing of the skin flaps.

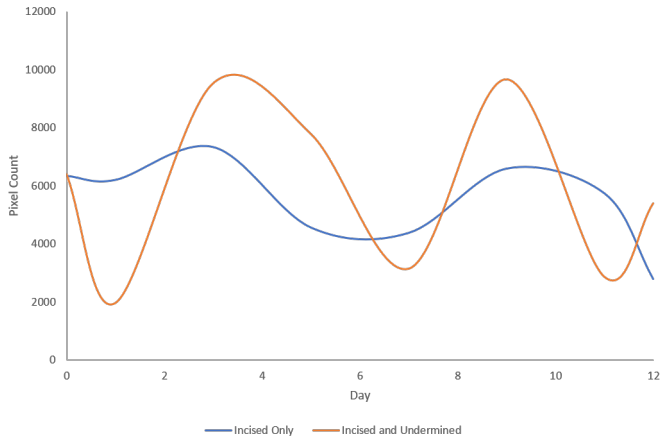


Figure 4.15: Number of pixels that have a temperature change greater than the background noise of the temporal filter for both incised only, and undermined flaps of Mouse 2 for each day of the study.

### 4.3.2 Fluorescence Imaging as a Function of Time

Figure 4.16 shows the IVIS fluorescence imaging of the flap regions (both incised-only and undermined) for Mouse 8. The ICG dye for Mouse 8 was administered sub-cutaneously. The ICG administered to the flap sub-cutaneously binds to the blood trapped in the scab and injured areas. After these areas have fully healed, the ICG dye is flushed from the area, diminishing the fluorescence. The intravenous ICG images yielded little information because of background fluorescence from larger organs. Both blood and ICG fluorescence are shown in Figure 4.16. In both types of fluorescent images, the edges of the flap are outlined early in the study. These images show that superficial healing appears to be complete by day 7. This is similar to the behavior seen for the mice in the thermal and white light images.

Additional analysis was performed of the ICG-fluorescence images using Living Image™software. ROI's were placed around the flap sites to measure the total radiant efficiency of the flap, and a second ROI was placed outside of the flap area to measure a background total radiant efficiency. The background total radiant efficiency was then subtracted from the flap site total radiant efficiency giving a measurement of radiant efficiency greater than the background. Radiant efficiency is defined as

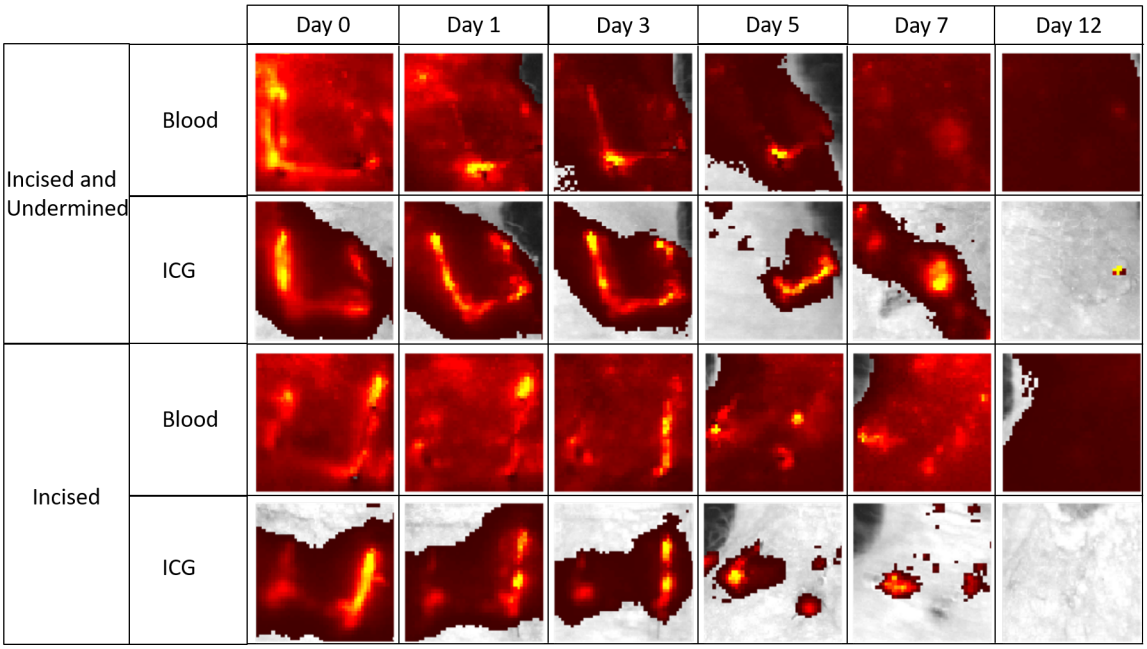


Figure 4.16: IVIS Spectrum images of Mouse 8 taken over the course of the 12-day study for the incised only flap and the undermined flaps. Images of both the fluorescence of blood ICG are shown.

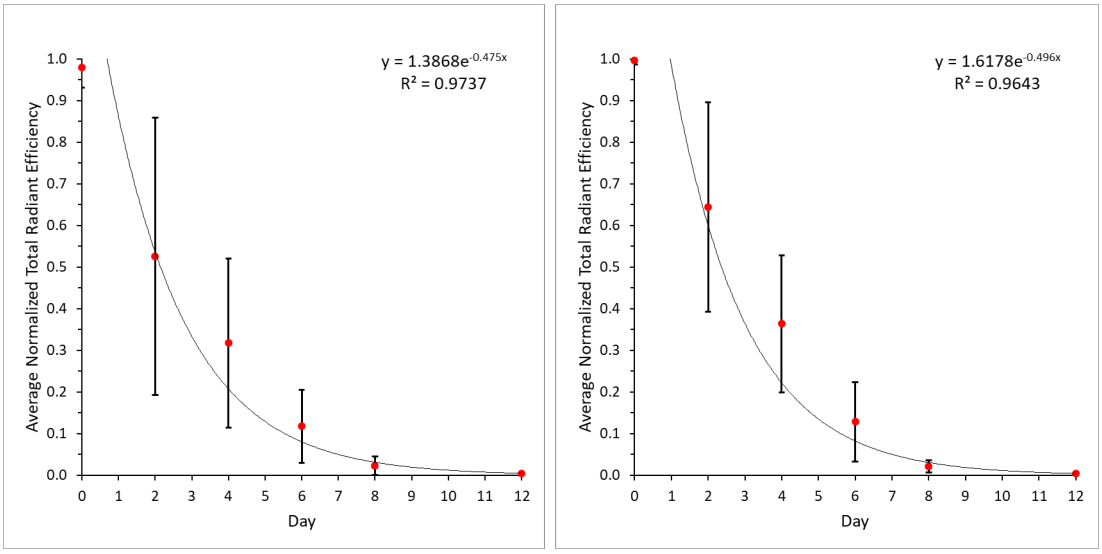


Figure 4.17: The average total radiant efficiency versus day of study for both incised only and undermined flaps of all mice.

the emission radiance (photons/second/cm$^2$/steradian) divided by the power density of the excitation light (microwatts/cm$^2$). Figure 4.17 shows a plot of the average radiant efficiency versus study day for IVIS images of ICG fluorescence in all mice.

Fluorescence decreases exponentially, with the curve flattening by day 7 for both the incised-only and undermined flaps. The exponential decrease shown in Figure 4.17 shows the flaps are healing and that the amount of blood trapped in the flap region is decreasing. Again, this agrees with the findings from the thermal and white light imaging that superficial healing was complete for both flaps by day 7.

Figure 4.18 shows the average radiant efficiency of both incised only and undermined flaps for all mice versus day of study. The same process that was used to measure the radiant efficiency for blood as was described previously for the ICG fluorescence images. A similar exponential decay is seen for blood fluorescence. This is most likely due to the radiant efficiency measured at the flap site being dominated by the superficial damaged regions caused by the incisions. The exponential curve for both incised and undermined flaps flattens by day 7 showing that superficial healing was complete for both flaps, and agreeing again with the findings from thermal and white imaging. Comparing the radiant efficiency shown in figure 4.18 to the pixel counts versus study day shown in Figure 4.10 shows a vast difference in behavior between the days of study. If the blood fluorescence radiant efficiency is dominated by the superficial areas, then the difference in behavior may show the potential for ETI to be more sensitive to non-superficial damage.

## 4.4 Conclusion

Enhanced thermal imaging is a novel combination of standard thermal imaging and selective heating of blood rich tissue. This technique has been shown to map vascular networks in real-time, monitor tumor growth, and now has the potential for intra-operative and post-operative monitoring of tissue perfusion.[2,38] This preliminary study showed a comparison between ETI and IVIS imaging in monitoring healing of surgical flaps created on 15 mice over a 12 day study. The ETI (no filter), spatially filtered ETI, temporally filtered ETI, white light images, and both blood and ICG fluorescence IVIS imaging all clearly show the superficial healing around

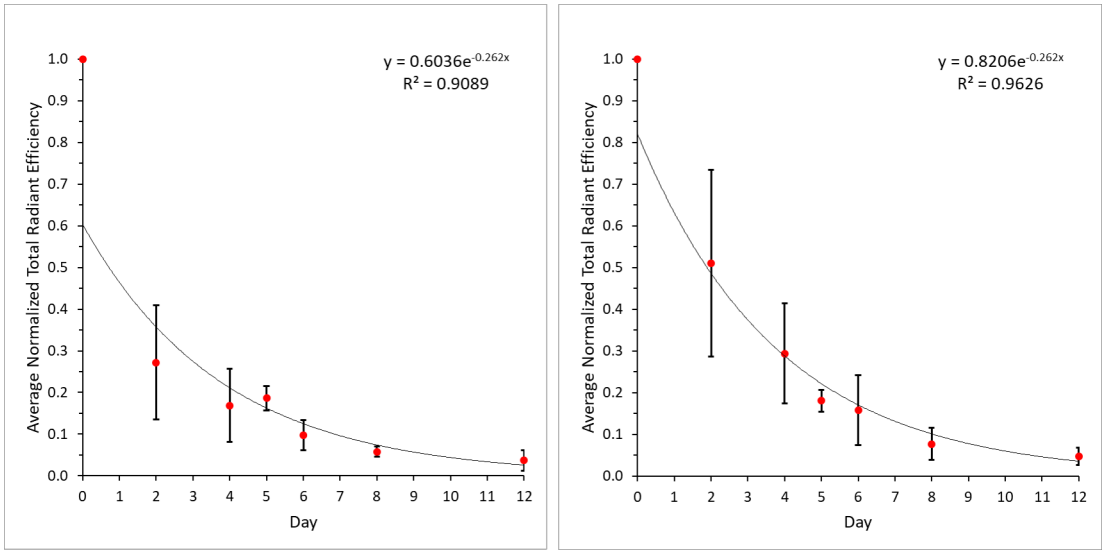


Figure 4.18: The average total radiant efficiency versus day of study for both incised and undermined and incised only skin flaps for all mice.

the edges of both the incised-only and undermined flaps. The temporally filtered ETI showed persistent heating in the undermined flap beyond this time of superficial healing.Further examination of number of pixels with a temperature change greater than the background measured in each temporally filtered ETI image shows that there is a secondary peak that may be associated with the healing/reperfusion of the center of the undermined flap via blood vessels from below. This healing/reperfusion is not seen in the other types of imaging. Measurements of radiant efficiency for ICG and blood fluorescence showed exponential decay trends agreeing with visual inspection and ETI of superficially damaged areas. The trends seen above match those shown previously with reattached skin grafts, the ratio of filled blood vessels to total blood vessels increases on between the first 48-60 hours and again betweeen days 5 and 6 post surgery.[40,41] ETI shows potential for monitoring non-superficial healing that is not visually apparent. This could reveal the development of deeper necrotic tissue. This preliminary study has shown the need for a larger more involved mouse study that can measure capillary density via flap excision on each day of the study to correlate the trends seen with ETI images to new vessel growth.

The introduction of intraoperative imaging techniques has shown beneficial impacts on the prevention of tissue necrosis.[22] The use of mid-IR imaging systems has severe limitations, and is consistently outperformed by ICGA.[30,31,33,36] The combination of selective heating with standard thermal imaging shows potential in overcoming these limitations while providing a cost effective and compact solution that can be used in real time intraoperatively or postoperatively.

# CHAPTER 5: CONCLUSIONS

The introduction of intraoperative image guidance has shown improvements in patient outcomes and reductions in costs for patients.[22] However, current imaging techniques have limitations such as the necessity for intravenous injection of contrast agents. Enhanced thermal imaging (ETI) is novel combination of standard thermal imaging and selective heating of embedded blood vessels. This combination shows potential in overcoming short comings of biomedical applications of standard thermal imaging highlighted previously by Han et al.[31] These limitations include poor contrast between different tissue types because temperature differences within the body is small, and poor spatial resolution from limited pixel densities in microbolometer arrays. The studies presented in this dissertation illustrate the potential for ETI to be used for both intraoperative imaging and post-surgical monitoring, while avoiding the necessity of intravenous contrast agents.

In the first study, the real time imaging capabilities of ETI were demonstrated by mapping vascular networks within porcine heart tissue *ex vivo*. Previously, ETI required extensive post-acquisition processing and application of the derivative filters. In the study presented here, the spatial and temporal filters were applied in real time, as the videos were acquired. The combination of ETI with the temporal derivative filter allowed for rapid delineation of vessel morphology and accurate measurements of vessel lengths. The removal of unnecessary temperature information along the surface of the porcine heart allowed detection and mapping of vessels more quickly and accurately than unfiltered ETI. Combined with the spatial derivative filter, ETI clearly delineates vessel walls and can provide measurements of vessel width.

The second study focused on simulating ETI to optimise the imaging process and

gain insights on how to use ETI to determine vessel depths and widths. ETI can be used in two different modalities - direct and indirect LED illumination. Direct illumination illuminates the same region that is being imaged. Computational simulations of direct illumination showed that for vessels below a depth of approximately 2 mm, LED illumination did not provide adequate heating to detect the thermal signature of the vessel at the tissue surface (regardless of vessel size). In addition, the temperature at the surface of the tissue was found to be independent of vessel size both computationally and in *ex vivo* tissue experiments. Further, by characterizing the contrast between the temperature directly above an embedded vessel and the temperature of the surrounding tissue, a signal arrival time could be determined in the simulations. This arrival time depended only on vessel depth and could be a way to measure the depths of embedded vessels. This trend was not seen in the *ex vivo* tissue experiments due to thermal and spatial resolution limitations of the ETI setup. Indirect illumination was also simulated. In this mode, a vessel is illuminated upstream the imaging area.[38] Computational simulations showed the potential of distinguishing the depth of an embedded vessel based on the time of maximum temperature change at the surface. *Ex vivo* tissue experiments showed this same potential, but with the inconsistency of blood perfusion rate, this trend was not as clear. Tissue experiments also showed an independence on the separation between point of interest and point of illumination.

In the third study, ETI was used to monitor the healing and re-perfusion of surgically induced skin flaps on 15 mice. ETI was then compared to the gold standard of IVIS imaging. Both ETI and IVIS clearly showed the superficial healing around the edges of both the incised and undermined flaps. Spatially filtered ETI images showed delineation between perfused and non-perfused regions, while temporally filtered ETI showed persistent heating in the undermined flaps beyond the time of superficial healing. Further analysis of the temporally filtered ETI images counted the number

pixels that had a temperature change greater than the background noise after 20 s of illumination. This revealed that between days 2-4 both flaps had a large increase in the number of pixels that responded to the illumination, and the undermined flaps had another large response between days 6-8. This trend was not seen in the IVIS radiant efficiency graphs which showed an exponential decay in fluorescence for both blood and ICG. The superficial damage seems to dominate the signal measured with IVIS, while ETI has the potential for monitoring non-superficial healing that is not visually apparent or seen via IVIS imaging. This could reveal the development of deeper necrotic tissue.

Future work will include improvements to the MCmatlab simulation, and *ex vivo* tissue experiments with a controlled blood perfusion rate. The computational model restricted the energy flow at the boundaries of the tissue model, lacked convective cooling at the tissue surface, and did not include blood flow. The addition of these parameters will create a more robust model to predict the effects of ETI. In future studies, the ETI imaging system will include a relay lens to achieve a higher spatial resolution to help resolve temperature gradients produced along the surface of the tissue. Finally, an animal or human trial to further explore the trends shown computationally will be completed. The preliminary animal study discussed here showed the potential for ETI to monitor surgical sites post-operatively for tissue viability. However, a larger more involved study is needed to link the trends measured with ETI to capillary growth over the course of the study. This can be performed by using a larger animal population and excising grafts at the end of each day to measure capillary growth via fluorescent and optical imaging.

# REFERENCES


[1] J. R. Case, M. A. Young, R. G. Keanini, and S. R. Trammell, "Using led sources to selectively heat blood for enhanced mid-ir imaging of vascular structures," in *Biomedical Optics*, pp. BS5A–1, Optical Society of America, 2014.

[2] J. R. Case, M. A. Young, D. Dréau, and S. R. Trammell, "Noninvasive enhanced mid-ir imaging of breast cancer development in vivo," *Journal of biomedical optics*, vol. 20, no. 11, p. 116003, 2015.

[3] J. Case and S. Trammell, "Methods and systems using led sources to create contrast agents for mid-infrared imaging of blood vessels," Dec. 11 2018. US Patent 10,149,620.

[4] J. Crezee and J. Lagendijk, "Temperature uniformity during hyperthermia: the impact of large vessels," *Physics in Medicine & Biology*, vol. 37, no. 6, p. 1321, 1992.

[5] K. z. Hadley PhD, "Oregan State PHYS207 topics."

[6] "Thermoworks, What is Emissivity?."

[7] Madhu, "Difference between Bohr model and quantum model."

[8] G. Keiser, *Biophotonics*. Springer, 2016.

[9] M. Fox, "Optical properties of solids," 2002.

[10] L. Wang, S. L. Jacques, and L. Zheng, "Mcml - monte carlo modeling of light transport in multi-layered tissues," *Computer methods and programs in biomedicine*, vol. 47, no. 2, pp. 131–146, 1995.

[11] D. Marti, R. N. Aasbjerg, P. E. Andersen, and A. K. Hansen, "Mcmatlab: an open-source, user-friendly, matlab-integrated three-dimensional monte carlo light transport solver with heat diffusion and tissue damage," *Journal of biomedical optics*, vol. 23, no. 12, p. 121622, 2018.

[12] H. H. Pennes, "Analysis of tissue and arterial blood temperatures in the resting human forearm," *Journal of applied physiology*, vol. 85, no. 1, pp. 5–34, 1998.

[13] A. Zolfaghari and M. Maerefat, *Bioheat transfer*. IntechOpen, 2011.

[14] W. L. Nyborg, "Solutions of the bio-heat transfer equation," *Physics in Medicine & Biology*, vol. 33, no. 7, p. 785, 1988.

[15] M. C. Kolios, A. E. Worthington, D. W. Holdsworth, M. D. Sherar, and J. W. Hunt, "An investigation of the flow dependence of temperature gradients near large vessels during steady state and transient tissue heating," *Physics in Medicine & Biology*, vol. 44, no. 6, p. 1479, 1999.

[16] R. Roemer, T. Cetas, J. Oleson, S. Halac, and A. Matloubieh, "Comparative evaluation of hyperthermia heating modalities: I. numerical analysis of thermal dosimetry bracketing cases," *Radiation research*, vol. 100, no. 3, pp. 450–472, 1984.

[17] K.-P. Möllmann and M. Vollmer, *Infrared thermal imaging: fundamentals, research and applications*. John Wiley & Sons, 2017.

[18] C. L. McGinnis and S. R. Trammell, "Non-invasive enhanced mid-ir imaging for real-time surgical guidance," in *Advanced Biomedical and Clinical Diagnostic and Surgical Guidance Systems XIX*, vol. 11631, p. 116310D, International Society for Optics and Photonics, 2021.

[19] A. Roggan, M. Friebel, K. Dörschel, A. Hahn, and G. J. Mueller, "Optical properties of circulating human blood in the wavelength range 400-2500 nm," *Journal of biomedical optics*, vol. 4, no. 1, pp. 36–46, 1999.

[20] B. T. Phillips, S. T. Lanier, N. Conkling, E. D. Wang, A. B. Dagum, J. C. Ganz, S. U. Khan, and D. T. Bui, "Intraoperative perfusion techniques can accurately predict mastectomy skin flap necrosis in breast reconstruction: results of a prospective trial," *Plastic and reconstructive surgery*, vol. 129, no. 5, pp. 778e–788e, 2012.

[21] A. E. Yang, C. A. Hartranft, A. Reiss, and C. R. Holden, "Improving outcomes for lower extremity amputations using intraoperative fluorescent angiography to predict flap viability," *Vascular and endovascular surgery*, vol. 52, no. 1, pp. 16–21, 2018.

[22] C. S. Duggal, T. Madni, and A. Losken, "An outcome analysis of intraoperative angiography for postmastectomy breast reconstruction," *Aesthetic Surgery Journal*, vol. 34, no. 1, pp. 61–65, 2014.

[23] H. R. Moyer and A. Losken, "Predicting mastectomy skin flap necrosis with indocyanine green angiography: the gray area defined," *Plastic and reconstructive surgery*, vol. 129, no. 5, pp. 1043–1048, 2012.

[24] G. C. Gurtner, G. E. Jones, P. C. Neligan, M. I. Newman, B. T. Phillips, J. M. Sacks, and M. R. Zenn, "Intraoperative laser angiography using the spy system: review of the literature and recommendations for use," *Annals of surgical innovation and research*, vol. 7, no. 1, pp. 1–14, 2013.

[25] P. Van Den Hoven, S. D. Van Den Berg, J. P. Van Der Valk, H. Van Der Krogt, L. P. Van Doorn, K. E. Van De Bogt, J. Van Schaik, A. Schepers, A. L. Vahrmeijer, J. F. Hamming, *et al.*, "Assessment of tissue viability following amputation surgery using near-infrared fluorescence imaging with indocyanine green," *Annals of Vascular Surgery*, 2021.

[26] G. S. De Silva, K. Saffaf, L. A. Sanchez, and M. A. Zayed, "Amputation stump perfusion is predictive of post-operative necrotic eschar formation," *The American Journal of Surgery*, vol. 216, no. 3, pp. 540–546, 2018.

[27] I. Ludolph, R. E. Horch, A. Arkudas, and M. Schmitz, "Enhancing safety in reconstructive microsurgery using intraoperative indocyanine green angiography," *Frontiers in surgery*, vol. 6, p. 39, 2019.

[28] E. H. Liu, S. L. Zhu, J. Hu, N. Wong, F. Farrokhyar, and A. Thoma, "Intraoperative spy reduces post-mastectomy skin flap complications: a systematic review and meta-analysis," *Plastic and Reconstructive Surgery Global Open*, vol. 7, no. 4, 2019.

[29] K. Li, Z. Zhang, F. Nicoli, C. D'Ambrosia, W. Xi, D. Lazzeri, S. Feng, W. Su, H. Li, M. Tremp, *et al.*, "Application of indocyanine green in flap surgery: a systematic review," *Journal of reconstructive microsurgery*, vol. 34, no. 02, pp. 077–086, 2018.

[30] A. Saxena, E. Ng, V. Raman, M. S. B. M. Hamli, M. Moderhak, S. Kolacz, and J. Jankau, "Infrared (ir) thermography-based quantitative parameters to predict the risk of post-operative cancerous breast resection flap necrosis," *Infrared Physics & Technology*, vol. 103, p. 103063, 2019.

[31] T. Han, N. Khavanin, J. Wu, M. Zang, S. Zhu, B. Chen, S. Li, Y. Liu, and J. M. Sacks, "Indocyanine green angiography predicts tissue necrosis more accurately than thermal imaging and near-infrared spectroscopy in a rat perforator flap model," *Plastic and reconstructive surgery*, vol. 146, no. 5, pp. 1044–1054, 2020.

[32] M. S. Fourman, R. P. Gersch, B. T. Phillips, A. Nasser, A. Rivara, R. Verma, A. B. Dagum, T. K. Rosengart, and D. T. Bui, "Comparison of laser doppler and laser-assisted indocyanine green angiography prediction of flap survival in a novel modification of the mcfarlane flap," *Annals of Plastic Surgery*, vol. 75, no. 1, pp. 102–107, 2015.

[33] M. E. Jaspers, M. Carrière, A. Meij-de Vries, J. Klaessens, and P. Van Zuijlen, "The flir one thermal imager for the assessment of burn wounds: Reliability and validity study," *Burns*, vol. 43, no. 7, pp. 1516–1523, 2017.

[34] R. F. Lohman, C. N. Ozturk, R. Djohan, H. R. Tang, H. Chen, and K. L. Bechtel, "Predicting skin flap viability using a new intraoperative tissue oximetry sensor: a feasibility study in pigs," *Journal of reconstructive microsurgery*, vol. 30, no. 06, pp. 405–412, 2014.

[35] J. T. Alander, I. Kaartinen, A. Laakso, T. Pätilä, T. Spillmann, V. V. Tuchin, M. Venermo, and P. Välisuo, "A review of indocyanine green fluorescent imaging in surgery," *International journal of biomedical imaging*, vol. 2012, 2012.

[36] B. Lahiri, S. Bagavathiappan, T. Jayakumar, and J. Philip, "Medical applications of infrared thermography: a review," *Infrared Physics & Technology*, vol. 55, no. 4, pp. 221–235, 2012.

[37] J. M. Prewitt, "Object enhancement and extraction," *Picture processing and Psychopictorics*, vol. 10, no. 1, pp. 15–19, 1970.

[38] C. L. McGinnis, M. R. Kern, G. D. Olson, and S. R. Trammell, "Enhanced thermal imaging: a real-time imaging technique to delineate blood vessels embedded in soft tissue," in *Photonics in Dermatology and Plastic Surgery 2022*, vol. 11934, pp. 26–33, SPIE, 2022.

[39] P. Van Den Hoven, S. D. Van Den Berg, J. P. Van Der Valk, H. Van Der Krogt, L. P. Van Doorn, K. E. Van De Bogt, J. Van Schaik, A. Schepers, A. L. Vahrmeijer, J. F. Hamming, *et al.*, "Assessment of tissue viability following amputation surgery using near-infrared fluorescence imaging with indocyanine green," *Annals of Vascular Surgery*, vol. 78, pp. 281–287, 2022.

[40] N. Lindenblatt, M. Calcagni, C. Contaldo, M. D. Menger, P. Giovanoli, and B. Vollmar, "A new model for studying the revascularization of skin grafts in vivo: the role of angiogenesis," *Plastic and reconstructive surgery*, vol. 122, no. 6, pp. 1669–1680, 2008.

[41] S. O'Ceallaigh, S. E. Herrick, J. E. Bluff, D. A. McGrouther, and M. W. Ferguson, "Quantification of total and perfused blood vessels in murine skin autografts using a fluorescent double-labeling technique," *Plastic and reconstructive surgery*, vol. 117, no. 1, pp. 140–151, 2006.

[42] T. Troy, A. Akin, E. Lim, N. Zhang, J. Kim, J. Whalen, C. K. B. Rice, H. Xu, and C. Shelton, "Advances in 3d optical imaging quantification and sensitivity," *Application Article,. Caliper Life Sciences*, 2011.